Czech Technical University in Prague

Faculty of Electrical Engineering

Doctoral Thesis

October 2018 *Martin Němec*

Czech Technical University in Prague

Faculty of Electrical Engineering
Department of Electrotechnology

Microstructural Characterization of Mg-Zn Alloys Using Transmission Electron Microscopy

Doctoral Thesis

Ing. Martin Němec

Prague, October 2018

Ph.D. Programme: P2612-Electrical Engineering and Information Technology
Branch of study: 2602V009-Electrotechnology and Materials

Supervisor: ***Ing. Josef Sedláček, CSc.***
Supervisor-Specialist: ***RNDr. Aleš Jäger, Ph.D.***

Abstract

The thesis is focused on microstructural characterization of perspective Mg-Zn alloys using transmission electron microscopy techniques. Brief history and industrial applications of Mg and its alloys are discussed. Recent perspective applications are highlighted, together with advantages and disadvantages of Mg. Options for improvement of its properties are also described, with focus on alloying with Zn, which is one of the common alloying element in Mg. Current state of knowledge about Mg-Zn system and its gaps are also thoroughly discussed.

The essential tool for the microstructural characterization in this work is transmission electron microscope. The instrument, its basic properties and abilities are briefly described. Fundamentals of crystallography and physical metallurgy regarding crystalline metallic materials are remarked. Crystallographic and metallurgical phenomena used in the Results and Discussion section are elucidated. Interaction of electrons with solid crystal, which provides insight to experimental data acquisition and processing, is explained. Structural properties of Mg that are important for the thesis are pointed out: crystal structure, deformation behaviour and solidification of Mg-Zn alloys.

Mg–6 wt.%Zn and Mg–12 wt.%Zn alloys are prepared by casting under Ar+ atmosphere. As-cast alloys are subjected to severe plastic deformation using equal channel angular pressing with applied back pressure. Two types of microstructure are analysed: as-cast and after severe plastic deformation for both Mg-Zn alloys. The microstructures are examined using imaging, diffraction and spectroscopy transmission electron microscopy techniques. General microstructural features of the α-Mg Matrix and four distinct types of intermetallic particles are investigated in the α-Mg matrix. The existence of the $Mg_{21}Zn_{25}$ phase is experimentally proven in particular. The results of microstructural characterization of the alloys after severe plastic deformation are compared and discussed regarding the analysis of the initial state of the alloy. The α-Mg matrix after severe plastic deformation is composed of two types of areas. The first type of area has highly deformed microstructure, and the second area has partially recrystallized microstructure. Furthermore, intermetallic particles in the microstructure after severe plastic deformation are thoroughly analyzed and compared with the initial state.

Electron energy-loss spectroscopy and high-angle annular dark field imaging are employed to investigate uneven distribution of Zn in the α-Mg matrix after severe plastic deformation.

In addition, compression and corrosion tests of both alloys in both states (as-cast and after severe plastic deformation) are performed to investigate influence of microstructure changes after severe plastic deformation on its mechanical and corrosion properties. Mechanical properties are analyzed by uniaxial compression tests at constant crosshead speed. Corrosion rate of the alloys is evaluated using hydrogen evolution method. Results of mechanical and corrosion test are correlated with microstructural observations.

Key words:

Crystallography; magnesium alloys; microstructure; metalurgy; severe plastic deformation; transmission electron microscopy.

Abstrakt

Práce je zaměřena na mikrostrukturní charakterizaci slitin Mg-Zn pomocí technik transmisní elektronové mikroskopie. Stručná historie a průmyslové využití Mg a jeho slitin jsou popsány s důrazem na aktuální perspektivní aplikace, společně s příznivými i nepříznivými vlastnostmi Mg. Možnosti zlepšení vlastností Mg jsou objasněny se zaměřením na legování pomocí Zn. Dále je v práci podrobně rozebrán současný stav znalostí o systému Mg-Zn včetně některých neobjasněných faktů a jevů.

Klíčovým nástrojem pro mikrostrukturní charakterizaci je v této práci transmisní elektronový mikroskop. Mikroskop, jeho vlastnosti a možnosti využití při analýze mikrostruktur jsou v rámci práce stručně popsány. Základní pojmy a jevy krystalografie a fyzikální metalurgie využívané v kapitole Results and Discussion jsou objasněny se zaměřením na Mg. Vysvětlení principů interakce elektronů s pevnou látkou v transmisním elektronovém mikroskopu poskytuje pochopení principů využitých experimentálních metod a vyhodnocení získaných dat. V teoretické části jsou zdůrazněny též strukturní vlastnosti Mg, jeho krystalografie, deformační chování a tuhnutí Mg-Zn slitin.

Slitiny Mg–6 wt.%Zn a Mg–12 wt.%Zn jsou v této práci analyzovány s využitím zobrazovacích, difrakčních i spektroskopických technik transmisní elektronové mikroskopie. Popsány jsou základní mikrostrukturní vlastnosti α-Mg matrice, v níž jsou pozorovány čtyři druhy intermetalických částic. Zejména je experimentálně prokázána existence fáze $Mg_{21}Zn_{25}$. Obě slitiny jsou poté modifikovány metodou intenzivní plastické deformace, jejíž vliv na mikrostrukturní, mechanické a korozní vlastnosti je podrobně analyzován. Výsledky analýzy těchto vlastností před a po zpracování slitin intenzivní plastickou deformací jsou podrobně diskutovány. Matrice α-Mg po intenzivní plastické deformaci sestává ze dvou typů oblastí. Jedná se o vysoce deformovanou mikrostrukturu a částečně zrekrystalizovanou mikrostrukturu. Změnami prošly i intermetalické částice, jejichž vlastnosti a morfologie jsou detailně popsány a porovnány se základním stavem před intenzivní plastickou deformací.

S využitím technik spektroskopie energiových ztrát elektronů a zobrazování ve tmavém poli elektrony rozptýlenými do vysokých úhlů byla objevena nehomogenní distribuce Zn v α-Mg matrici. Mechanické vlastnosti jsou zkoumány jednoosým zatěžováním v tlaku při pokojové teplotě a konstantní rychlosti příčníku. Korozní rychlost slitin je vyhodnocena s využitím metody uvolňování vodíku. Výsledky mechanických a korozních experimentů jsou vztaženy k mikrostrukturní analýze.

Acknowledgement

I would like to kindly thank to all colleagues in my research specialization who helped me to gain necessary practical and theoretical skills, particularly Viera Gärtnerová and Aleš Jäger.

I would like also to thank to my co-authors for their valuable contribution.

Support offered by GACR GBP108/12/G043 is appreciated.

List of Contents

List of Symbols and Acronyms

[uvw]	Miller indices of crystallographic directions
[UVTW]	Miller-Bravais indices of crystallographic directions
[hkl]	Miller indices of crystallographic planes
[HKIL]	Miller-Bravais indices of crystallographic planes
°C	degree of Celsius
$\mathrm{\alpha}$	solid solution, solid phase
α	convergence semi-angle
β	collection semi-angle
$\mathrm{\varepsilon}$	mechanical strain
$\mathrm{\phi}$	die inter-channel angle
θ	Bragg angle
λ	wavelength
μm	micrometers
$\mathrm{\sigma}$	mechanical stress
a, b, c	lattice parameters, lattice axes
A	elongation
at.%	atomic percent
c_i , c_A , c_B	concentration
d	interplanar spacing
eV	electron volt
$\mathrm{E_B}$	binding energy
$\mathrm{E_C}$	eutectic temperature
H	hours
kV	kilovolt
keV	kilo electron volt

l	liquidus curve
L	liquid phase
m	mass of phase
m, n, o	basis vectors´ fractions
MPa	megapascal
nm	nanometre
q	quantity of phase
r	solubility-limit curve
s	solidus curve
t	thickness
T	temperature
wt.%	weight percent
x, y, z	basis vectors
BF	bright-field
BP	back-pressure
BSE	back-scattered electrons
CBED	convergent-beam electron diffraction
CCD	charge-coupled device
CL	cathodoluminescence
CMOS	complementary metal oxide semiconductor
ECAP	equal channel angular pressing
ECAP-BP	equal channel angular pressing with applied back-pressure
ED	extrusion direction
EDS	energy-dispersive X-ray spectroscopy
EELS	electron energy loss spectroscopy
FFT	fast Fourier transform
FIB	focussed ion beam

HAADF	high-angle annular dark field
HAADF-STEM	high-angle annular dark field scanning transmission electron microscopy
hcp	hexagonal close-packed
HRTEM	high-resolution transmission electron microscopy
ID	insertion direction
LM	light microscopy(e)
PA-EDT	precession-assisted electron diffraction tomography
RT	room temperature
SAED	selected area electron diffraction
SE	secondary electrons
SEM	scanning electron microscopy(e)
SPD	severe plastic deformation
STEM	scanning transmission electron microscopy
OR	orientation relationship
TD	transverse direction
TEM	transmission electron microscopy(e)
TEM BF	transmission electron microscopy bright-field

1 Introduction to Mg-Zn System

Magnesium was discovered in the form of magnesium oxide in 1808 and metallic magnesium was first isolated in 1828 [1]. It comprises 2.7% of the earth´s crust. Commercial production began in the middle of the nineteenth century. The production per year in the 1990s was estimated to 350 000 tonnes [1]. The first industrial use of magnesium in the form of a fine powder was in pyrotechnics (miscellaneous fireworks, high-energy fuels, photographic flashlights). Magnesium is used in metallurgy as an alloying element to improve strength and corrosion resistance of aluminium or as a constituent in other systems (zinc or nickel-copper products). In chemistry, magnesium is used for a production of organic and organometallic compounds or electro-chemical products, such as batteries and galvanic anodes. Because magnesium is extremely light metal, it is very attractive in structural applications for moving or lifting parts [2].

1.1 Mg-Zn Binary Phase Diagram

Magnesium-Zinc alloys belong to the most important magnesium-based materials with remarkable precipitation hardening effect [3, 4]. The Mg-Zn system is a subject of widespread research that covers lightweight components in the automotive and aerospace industries; sporting goods and portable electronic devices, where the weight-to-strength ratio of Mg is one of the most important parameters [2]. Mg-Zn is also considered for hydrogen [5] or thermal energy storage [6] and was successfully used to prepare MgO nanoparticles via the green-chemistry route [7]. However, a fundamental understanding regarding the formation of intermetallic compounds beyond the solubility limit of Zn in Mg such as speculative $Mg_{21}Zn_{25}$ remains a subject of a doubt. The main reason is a lack of an experimental work.

As summarized by Agarwal [8], the Mg-Zn binary system has been thoroughly investigated since 1904. A significant amount of work was also recently performed [9–16]; however, there are only a few experimental works that addressed Mg-Zn binary alloys with a Zn concentration that exceeded the solubility limit in Mg at the eutectic temperature [6, 14–18]. This deficiency could be a major reason for an uncertainty about a crystal structure of the Mg-Zn intermetallic phase at approximately 74 wt.% of the Zn concentration in a generally accepted binary phase diagram [19] or its revised forms [8, 20]. This phase was first proposed by Hume-Rothery et al. [21] as MgZn and later substituted by $Mg_{12}Zn_{13}$ based on the experimental work of Clark and Rhines [17]. They predicted that the phase forms at 72.9 wt.% of Zn but experimentally found formation at 74.5 wt.% of Zn, which corresponds to the $Mg_{12}Zn_{13}$ stoichiometry. Two different crystal structures were suggested for this phase. The first one (hexagonal with lattice parameters a = 1.066 nm, c = 1.716 nm) by Tarschnisch [22] and the second one (rhombohedral with lattice parameters a = 2.569 nm, c = 1.810 nm) by Khan [23]; however, those structures have never been experimentally confirmed. In the experimental work of Černý and Renaudin [24], the crystal structure of the Mg-Zn specimen was examined with single-crystal X-ray diffraction. The crystal structure of the major intermetallic compound in the material was determined as a trigonal $Mg_{21}Zn_{25}$ with lattice parameters a = 2.578 nm and c = 0.876 nm. This structure should substitute the $Mg_{12}Zn_{13}$ compound in the phase diagram. Despite this finding, in recent experimental works [14, 16] and reassessments of the Mg-Zn binary system [10–12], the $Mg_{12}Zn_{13}$ (or MgZn) with experimentally unconfirmed crystal structure remained considered.

However, an alternative form of the Mg-Zn binary phase diagram, where $Mg_{12}Zn_{13}$ (or MgZn) was replaced by $Mg_{21}Zn_{25}$ at approximately 74 wt.% of the Zn concentration, is available in a textbook [25] or accessible in an online database [26]. Moreover, this new type of diagram was also considered in [5]. In 2013, Okamoto [27] published an Mg-Zn binary phase diagram based on the summary of up-to-date information about this system. According to the newly adapted diagram, the ***Mg-Zn binary intermetallic phases are*** as follows: $\boldsymbol{Mg_{51}Zn_{20}}$, $\boldsymbol{Mg_{21}Zn_{25}}$, $\boldsymbol{Mg_{4}Zn_{7}}$, $\boldsymbol{MgZn_{2}}$ and $\boldsymbol{Mg_{2}Zn_{11}}$ [24, 28–31]. $Mg_{21}Zn_{25}$ was also placed at a higher Zn concentration of 76.2 wt.% because of its stoichiometry. Nevertheless, there are still references in notably recent works (for example [32]) to the outdated one, but it remains a generally accepted version of the diagram [19].

In the experimental work of Gao and Nie [14], which addressed the Mg-8wt.%Zn alloy, the MgZn phase was discussed as a β phase, which should form equilibrium with α-Mg matrix. A eutectoid reaction is reported during the treatments at 325°C or below (Mg_7Zn_3 is a former notation of $Mg_{51}Zn_{20}$):

$$Mg_7Zn_3 \rightarrow \alpha\text{-}Mg + Mg_4Zn_7. \tag{1.1}$$

Consequently, because of the metastability of Mg_4Zn_7:

$$Mg_4Zn_7 \rightarrow MgZn. \tag{1.2}$$

In the recent paper of Rodríguez et al. [6], the identical reactions are provided as follows, with the most recent notations of the phases from a diagram revised by Okamoto [27]:

$$Mg_{51}Zn_{20} \rightarrow \alpha\text{-}Mg + Mg_4Zn_7 \tag{1.3}$$

$$Mg_4Zn_7 \rightarrow Mg_{21}Zn_{25}. \tag{1.4}$$

1.2 Mechanical Properties of Pure Mg and its Alloys in General

Insufficient mechanical properties of pure Mg for load-bearing applications, for example, low yield strength, can be enhanced via a precipitation hardening effect or a grain refinement using severe plastic deformation (SPD) techniques. In the field of hydrogen storage, Mg alloys prepared by SPD can possess key properties similar to those prepared by expensive ball-milling methods [33].

Zinc is one of the most common ***alloying*** elements in Mg alloys with a great age-hardening response via the formation of intermetallic particles, mainly $MgZn_2$ and Mg_4Zn_7 precipitates [3, 4]. ***Intermetallic particles*** present in Mg-Zn alloys have been investigated using transmission electron microscopy since the 1960s [3] and remained peculiar until a revised binary phase diagram was published in 2013 [27]. However, with the development of modern SPD methods, research at the nanoscale has been more focused on the α-Mg at the expense of Mg-Zn intermetallic particles [34]. However, SPD can significantly affect intermetallic particles that might be responsible for the key material properties. Furthermore, Mg-Zn alloys has also been considered as a material for hydrogen [5] and thermal energy [6] storage. Mg-Zn is therefore the fundamental binary system used to enhance not only the mechanical properties of pure Mg.

As stated above, ***grain refinement via SPD*** leads to an improvement of weak mechanical properties of Mg and its alloys. Very popular and progressive grain refining method resulting in a grain size down to hundreds of nanometres is equal channel angular pressing (ECAP) [35]. During ECAP, various slip and twinning modes are activated as deformation mechanisms in pure Mg and its alloys, affecting the mechanical properties of the material [34, 36–38].

1.3 Biocompatibility and Biodegradability of Mg

In recent years, investigation of Mg and its alloys has increasingly expanded into the field of biocompatible and biodegradable materials. Among metallic elements, Mg possesses a Young's modulus closest to a human bone. Therefore, it is a suitable candidate for bone implants with minimized adverse effects, such as stress shielding of the bone [39]. It also exhibits a positive effect on the healing of bone tissue and favourable biocompatibility because it has the highest natural volume content in the human body among metals. Mg was first considered for biomedical implants more than a hundred years ago, and its properties as a biomaterial have been reviewed by many authors [40–43]. However, control of the corrosion rate of Mg biomaterials remains the most challenging issue and still has not been solved, thus limiting the use of Mg in this field [40], [42].

Mechanical and corrosion properties of a material are the most important with respect to the applications of biodegradable implants. A fundamental way to tailor the corrosion properties of Mg biomaterials is alloying [41]. One of the proper biocompatible elements for alloying with Mg is Zn, if an adequate concentration is used [41, 44]. The benefits of Zn addition to improve corrosion properties of Mg alloys have been thoroughly investigated by several authors [41–47]. Addition of Zn up to its solubility limit in Mg (approximately 6.2 wt.%), improve the corrosion properties of Mg [47]. In addition, Zn has beneficial effects on the corrosion film and can also elevate the charge transfer resistance of magnesium and thus reduce the corrosion rate [46]. However, taking into account Zn concentrations over solubility limit, corrosion properties are deteriorated due to a formation of secondary phases, which are responsible for production of excessive hydrogen gas [45–47].

1.4 Influence of SPD on Microstructural Evolution of Mg-Zn alloys

The microstructural features of the α-Mg matrix, distribution of secondary phases and intermetallic particles have an important impact on mechanical and corrosion properties of a particular alloy. Effect of Mg alloying with Zn and Al and various annealing treatment on mechanical properties of Mg alloys was addressed in the works by Cui et al. [48], [49]. The microstructural evolution of the α-Mg matrix due to SPD was addressed, for example, in [38, 50, 51]. However, a description of effects of grain refinement using SPD combined with the presence of secondary phases on the mechanical and corrosion properties has not been found in the literature yet.

1.5 Description of Material, Data and Techniques Used

Essential tool used for microstructural characterization was transmission electron microscopy (TEM) with various imaging, diffraction and spectroscopy techniques. This work uses the stoichiometry and crystallography of the intermetallic phases in an Mg-Zn binary phase diagram considering the latest information about those phases. An advantage of TEM is a possibility of direct identification of the particles that are undetectable using other techniques, notably X-ray diffraction and scanning electron microscopy because of their low volume fraction or small dimensions. Magnesium alloys with 12 wt.% of Zn concentration (referred as Mg12Zn hereafter) and 6 wt.% of Zn concentration (referred as Mg6Zn hereafter), which creates an abundant occurrence of particles with a phase that results from reactions (1.2) or (1.4), were examined. Complex microstructure characterization and crystal structure determination of all intermetallic compounds found in both alloys were accomplished using three different electron diffraction techniques. The possible orientation relationships of individual compounds toward the α-Mg matrix in the Mg12Zn alloy are thoroughly inspected and discussed in accordance with literature. The microstructure evolution of intermetallic particles in the Mg12Zn alloy subjected to ECAP with applied back pressure (ECAP-BP) is thoroughly characterized using TEM techniques. The results are compared with the microstructure of as-cast initial state of the Mg12Zn alloy prior to the ECAP-BP processing. Particular attention is also focused to the α-Mg matrix analysis of both Mg6Zn and Mg12Zn alloys. Uneven distribution of Zn in the α-Mg matrix of Mg12Zn alloy is analyzed using spectroscopic and advanced imaging techniques.

1.6 Aim of this Work

Main goals of this work are thorough microstructure characterization of Mg12Zn and Mg6Zn alloys; intermetallic compounds identification; determination of orientation relationship of intermetallic compounds toward the α-Mg matrix; investigation of influence of severe plastic deformation on microstructure evolution and changes in mechanical and corrosion properties; microstructure evolution evaluation after severe plastic deformation. The final aim of this work is to clarify the connection between the microstructural features and the mechanical and corrosion properties of Mg6Zn and Mg12Zn alloys processed by ECAP-BP.

2 Transmission Electron Microscope

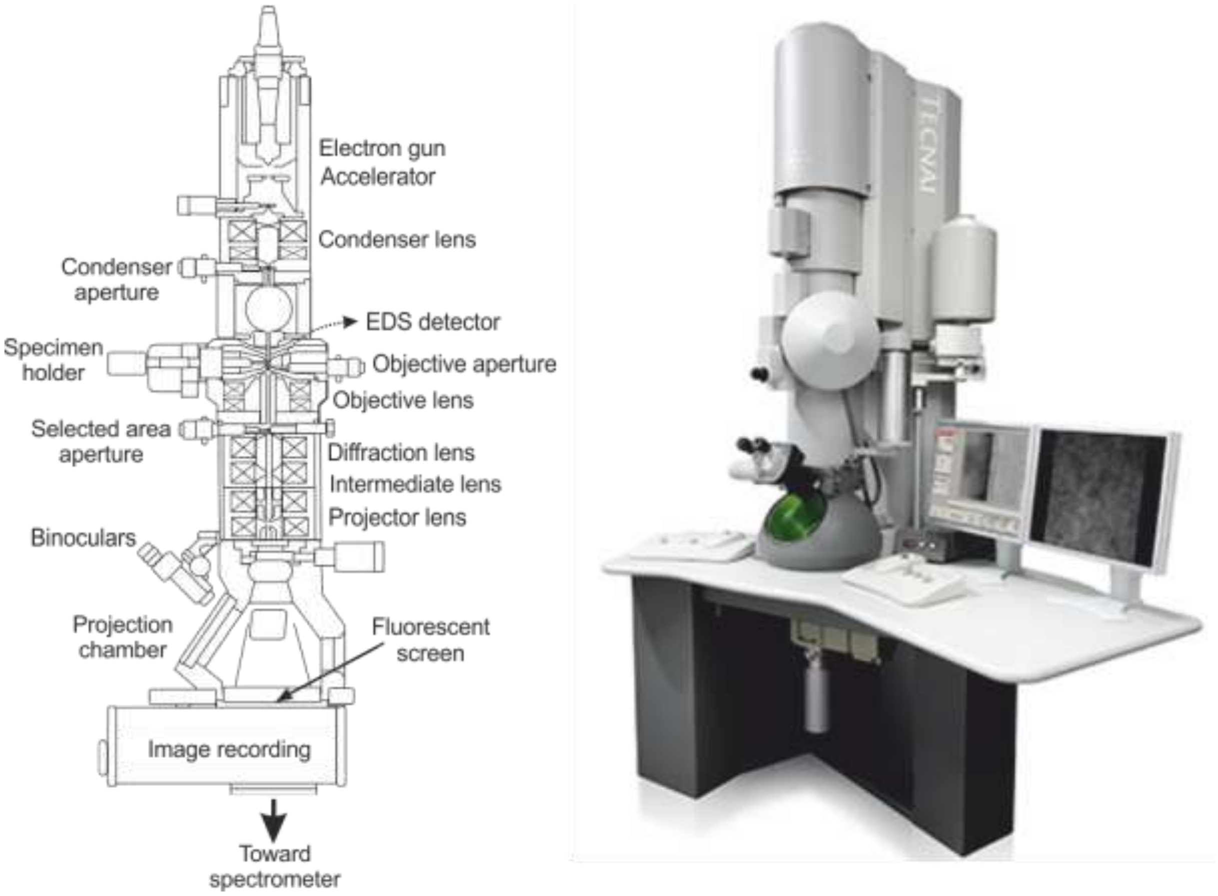

Fig. 1. Transmission electron microscope. The image shows a schematic cross-section of TEM that reveals essential components (on the left), and a photograph of the 200kV FEI 52 microscope used for TEM experiments in this work (on the right) [52].

Transmission electron microscope (TEM) is a complex and versatile scientific instrument. The most important advantage of TEM is that it works with a signal that propagates through a solid specimen. This signal carries information about the specimen volume, not only about the specimen surface. The most recent TEMs with an aberration-corrected electron optics attain a spatial resolution better than 0.1 nm [53] that is well below common interatomic distances in crystals. Current development in electron sources, electron filtering and spectrometer´s design allows to achieve energy resolution for electron spectroscopic techniques close to 0.01 eV [54]. Atomic vibration modes are becoming feasible to observe in TEM besides common analytical information about specimen chemistry. TEM is therefore a fundamental instrument in every field that deals with electronics, material design or nanotechnology. Notable disadvantages of TEM are demanding data evaluation and specimen preparation. It is therefore necessary to complement TEM, for example, by a scanning electron microscopy (SEM) or a light microscopy (LM).

Fig.1 shows several essential blocks of TEM. The upper part is an electron gun with an accelerator unit. In modern TEMs, electrons are extracted by strong electrical field applied to a source material. This type of gun is called field emission gun [55]. The electrons are then accelerated by accelerating voltage, typically 80 – 300 kV. State-of-the-art TEMs are often equipped with a monochromator that improves energy spread of the beam using energy filtering [55].

When the electron beam enters electron optics column, it is first adjusted by condenser lens system (Fig.1). Condenser lenses are used to guide the electron beam onto the specimen in specific conditions that are dependent on the experimental technique to be performed or the information to be extracted. The beam is formed by condenser system differently to obtain different information about the specimen. The beam can be parallel to the optical axis or focused to a small spot that is imprinted on the specimen. The angle of convergence and the size of the spot imprinted on the specimen can be controlled based on desirable information. The most advanced TEMs are nowadays equipped with a corrector of up to the third order spherical aberrations of the condenser lens. Uncorrected aberrations of electromagnetic lenses are otherwise significantly limiting microscope resolution [55].

A specimen is inserted into TEM using a specimen holder. The TEM holder is very important mechanical part of TEM, because it represents the only way for an operator to manipulate with the specimen. Principally, the specimen can be positioned, rotated, tilted, heated or electrically biased via the specimen holder, in dependence on the holder versatility. The specimen is located in evacuated specimen chamber where it is illuminated by the beam. TEMs can be optionally equipped also with an energy-dispersive spectrometer that is located inside the specimen chamber and enable to analyze specimen chemistry based on characteristic X-ray signal.

Objective lens creates the image of the specimen. This lens needs to be well aligned with the rest of the optical system in order to get the best result. The most powerful instruments are equipped with a corrector of up to the third order spherical aberration of the objective lens. Diffraction, intermediate and projector lenses control what is to be projected onto a fluorescent screen or a detector. We can project direct (bright- or dark- field) image of the specimen, diffraction pattern from a selected part of the specimen or high-resolution interference image from a chosen area. In history, photographic film plates were used for data recording and storage. Nowadays, CCD or CMOS cameras are now used for data recording and subsequent transfer to a digital form.

Fluorescent screen or digital cameras are located in a projection chamber (Fig. 1). The image of the specimen on the fluorescent screen can also be seen and magnified using binoculars. The benefit of the screen is much larger field of view. Modern instruments are optionally equipped with an electron energy-loss spectrometer or electron filter that is usually located behind the projection chamber. The screen can be lifted up to allow the beam to propagate toward the spectrometer. The spectrometer or the filter has its own cameras for the electron spectra or filtered image recording.

The TEM is permanently pumped to ultra-high vacuum to maintain its interior clean and prevent collisions of electron beam with air or dust particles.

3 Crystallography

This section show selection of fundamental crystallographic terms and phenomena used for interpretation of results in the Results and Discussion section of the thesis.

3.1 Symmetry of Crystal

Atoms in solids are often arranged periodically in all directions to uniformly fill the body of mass. The term crystal structure expresses how the atoms are situated in space with respect to each other. The atoms can form different crystal structures with dependence on their chemistry and thermodynamic conditions. Particular crystal structures can be distinguished based on dimensions and symmetry of a unit cell. Unit cell dimensions are characterized by lattice parameters. Symmetry expresses mutual positions of atoms in the unit cell. The unit cell is the smallest part of the crystal structure that can create the whole crystal just by translation in the three principal Cartesian directions. The symmetry of a crystal is therefore the symmetry of its unit cell [56–58]. Basic symmetries adopted by many metallic elements and their solid solutions are the cubic symmetry and the hexagonal symmetry.

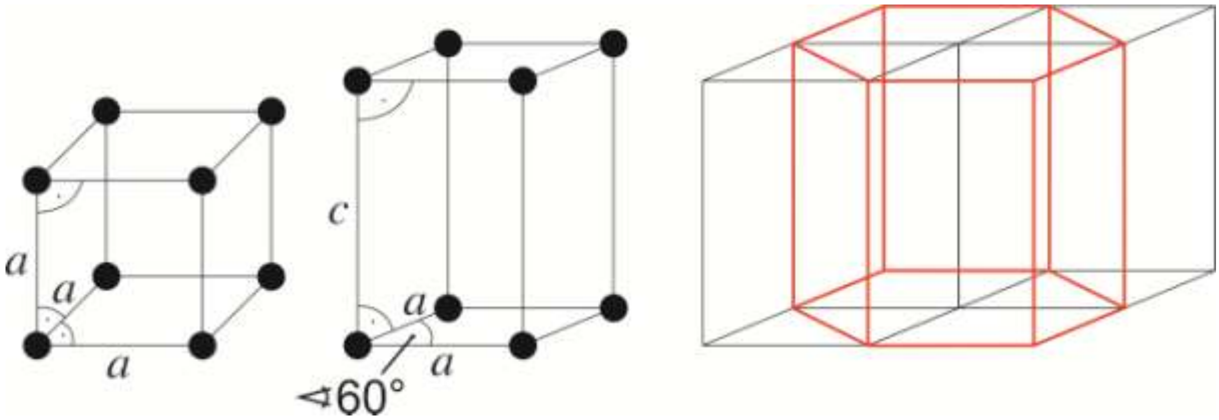

Fig. 2. Basic symmetries. a) The image shows the cubic crystal symmetry unit cell with lattice parameter *a*; b) the image shows the hexagonal crystal symmetry unit cell with lattice parameters *a* and *c*; c) the image shows four hexagonal unit cells with highlighted hexagon for more intuitive visualization of the hexagonal symmetry.

3.1.1 Cubic Symmetry

Atoms in a crystal are arranged to form a cube (Fig. 2 a). Three principal angles in a cube are 90 degrees and the length of the unit cell in the three principal Cartesian directions is equal. Therefore, only one number is needed to characterize a size of a cubic unit cell. This number is called the lattice parameter. It is represented by the length of a cube side (designated as *a*) in the case of a cubic unit cell.

3.1.2 Hexagonal Symmetry

Atoms are arranged in a crystal to form a rhombic prism (Fig. 2b). The hexagonal symmetry is however more intuitive when four unit cells are added together and a hexagonal prism is highlighted (Fig. 2c). The unit cell with the hexagonal symmetry has two axes of equal lengths that form an angle of 60° and the third one that forms the right angle with the first two and has a different length. The *c* axis acts as a 6-fold rotational axis, thus giving name to the hexagonal symmetry. Two lattice parameters are therefore needed to characterize a size of a hexagonal unit cell (designated as *a* and *c*) [56, 57]. The length ratio of the two lattice parameters depends on a chemical element and is very important especially with respect to a mechanical behaviour of the metal. It is designated as the *c/a* ratio. The *c/a* ratio plays important role during plastic deformation, which is discussed in the section 4.

3.2 Crystallographic Planes and Directions

Physical and chemical properties of a material are often dependent on the considered crystallographic direction or the crystallographic plane [57]. Examples of two crystallographic planes and directions in the cubic unit cell are shown in Fig. 3a. The planes and the directions need to be identified to distinguish them among each other and to relate them to a physical property of a material. A basis of vectors is chosen as a reference for identification of crystallographic planes and directions [56, 57]

3.2.1 Planes and Directions in Cubic Crystals

Preferable basis for cubic crystals is the cubic system of basis vectors (Fig. 3b). It consists of three mutually perpendicular vectors (x, y and z) with the common origin and the same length that is equal to the lattice parameter a. An arbitrary direction in a crystal can be represented by a corresponding vector r that comes from the origin and whose length is limited by the unit cell edge. This vector can be written as:

$$r = mx + ny + oz \tag{3.1}$$

where m, n and o are fractions of the basis vectors x, y and z, respectively. These fractions are then converted to the least common denominator and expressed in square brackets as [uvw] that are called Miller indices of a crystallographic direction. Two examples of indexed directions are in Fig. 3c. A bar above a number means that negative corresponding basis vector is taken into account [56, 57].

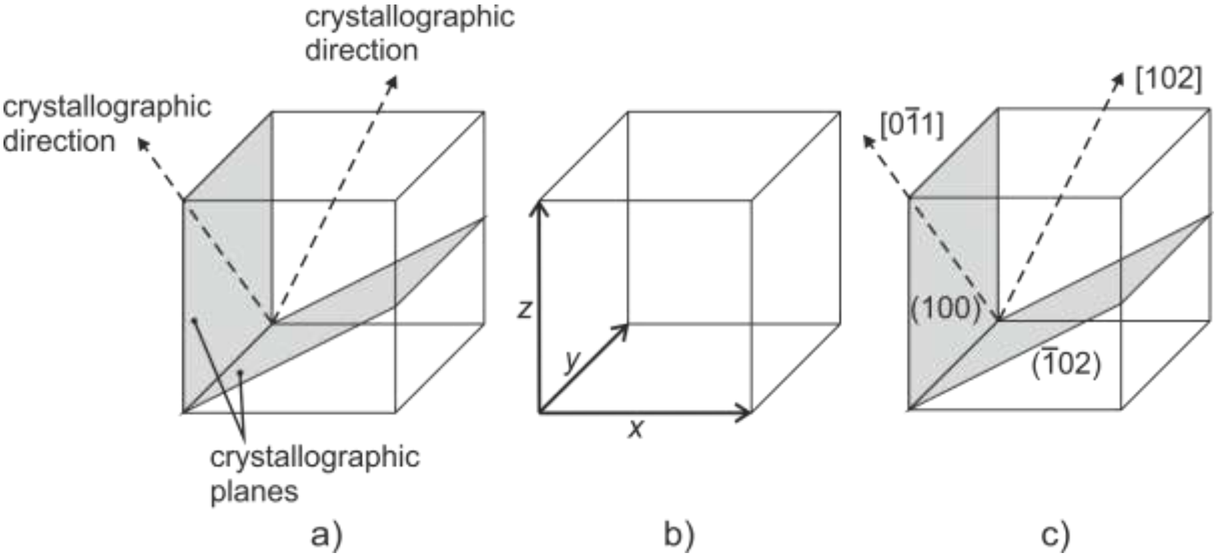

Fig. 3. Cubic symmetry. a) The image explains schematically general meaning of crystallographic planes and crystallographic directions; b) the image defines cubic system of basis vectors; c) the image shows identification of particular crystallographic planes and directions in the cubic unit cell using Miller indices [59].

Before identification of a crystallographic plane we have to first figure out which basis vectors are intercepted by the plane and then find out fractions of coordinates from the origin to the intercept. When a plane is collinear with a basis vector, intercept is considered to be at the infinity. Reciprocals of the finite intercepts are converted to the least common denominator and expressed in round brackets as (hkl) that are called Miller indices of a crystallographic plane. If a plane is collinear to a basis vector, corresponding Miller index is zero. Two examples of indexed planes are in Fig. 3c. A bar above a number means that the plane intercepts corresponding negative basis vector [59].

3.2.2 Planes and Directions in Hexagonal Crystals

Crystals with the hexagonal symmetry can be also indexed using a cubic system of basis vectors (Fig. 4a). The Miller indices of crystallographic directions and planes are then analogous. However, the use of the hexagonal system of basis vectors is more suitable for practical crystallography. The hexagonal system has four vectors, as seen from Fig. 4b. Indices expressed in the hexagonal system of basis vectors in the form of (HKIL) in the case of planes and [UVTW] in the case of directions are called Miller-Bravais indices. The procedure of indexing planes and directions is the same for hexagonal and cubic systems of basis vectors [56–58].

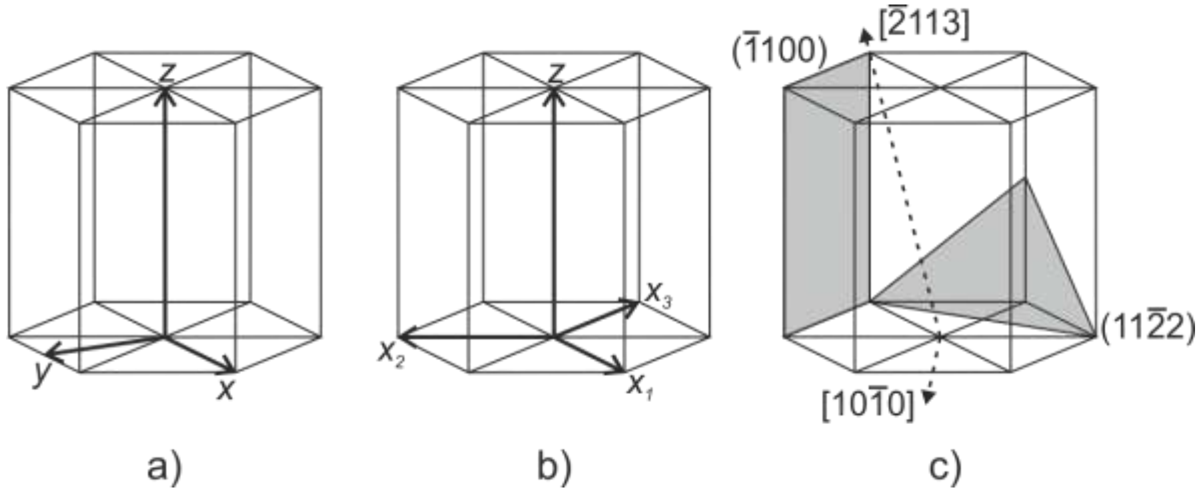

Fig. 4. Hexagonal symmetry. a) The image shows the cubic system of basis vectors applied to the hexagonal symmetry; b) the image shows the hexagonal system of basis vectors applied to the hexagonal symmetry; c) the image shows schematically identification of particular crystallographic planes and directions in a hexagon using Miller-Bravais indices.

The x_3 vector is a linear combination of the x_1 and the x_2. The 4-index notation is therefore mathematically redundant; however, it is preferred for its practical advantages. Transformation of crystallographic directions from the 3-index notation [uvw] to the 4-index notation [UVTW] is:

$$U = \frac{1}{3}(2u - v); V = \frac{1}{3}(2v - u); T = -\frac{1}{3}(u + v); W = w\,. \tag{3.2}$$

From the 4-index notation to the 3-index notation:

$$u = U - T = 2U + V; v = V - T = 2V + U; w = W. \tag{3.3}$$

The transformation from the 4-index notation to the 3-index notation of crystallographic planes using the hexagonal system of basis vectors is performed just by ignoring the third index I. Reversibly the I index in the 4-index notation of planes is determined from the 3-index notation:

$$I = -(h + k). \tag{3.4}$$

3.3 Crystallography of Mg and Mg Alloys

The crystal structure of Mg is hexagonal close packed (hcp). General hcp crystal structure is shown in Fig. 5. In a unit cell of the hexagonal close packed crystal, there is an additional plane inserted in the half of the *c* axis that is perpendicular to the *c* axis and collinear with the *a* axis. The indices of this plane are therefore (0002). Due to the symmetry of the crystal, all of the (0002) planes are equivalent among each other. A family of equivalent crystallographic planes is designated by curly brackets, in this case as the $\{0002\}$ equivalent planes. The $\{0002\}$ planes contain the $[2\overline{1}\overline{1}0]$ crystallographic direction. There are in total 6 equivalent directions due to the 6-fold symmetry that are marked with angle brackets as the family of equivalent $\langle 2\overline{1}\overline{1}0\rangle$ directions. The $\langle 2\overline{1}\overline{1}0\rangle$ directions are close packed directions. Close packed direction means that the density of atomic occupation through the crystal is the highest in this direction. The $\{0002\}$ planes and the $\langle 2\overline{1}\overline{1}0\rangle$ directions are very important with respect to the Mg deformation behaviour [60].

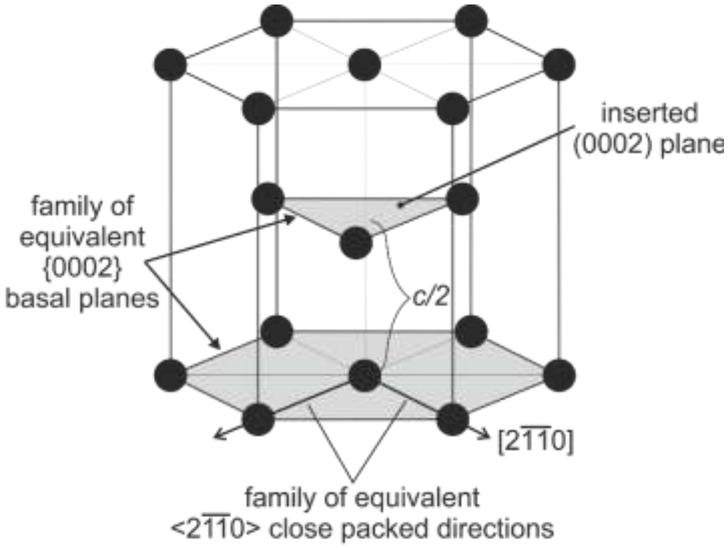

Fig. 5. Hexagonal close packed crystal structure. The image shows an inserted plane of the hexagonal close packed structure and explains the meaning and designation of crystallographic planes´ and directions´ families [60].

3.4 Zone Axis

The Zone axis is a crystallographic term frequently used in the field of crystallography and TEM. The zone axis is a crystallographic direction that is common to a number of crystallographic planes. Each plane located in the zone axis contains the zone axis direction. Hence, it has to satisfy:

$$hu + kv + lw = 0, \tag{3.5}$$

where h, k and l are (hkl) indices of the plane and u, v and w are [uvw] indices of the zone axis direction. The zone axis is schematically shown in Fig. 6.

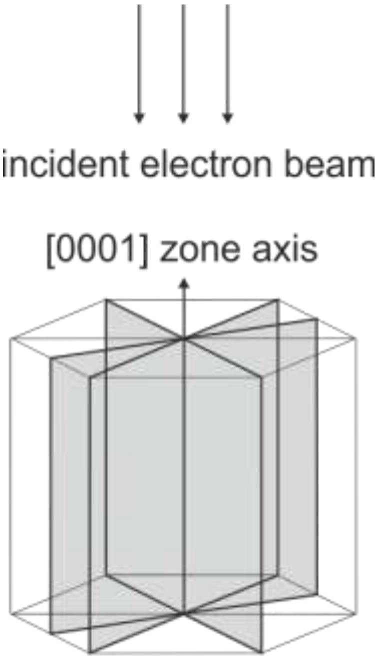

Fig. 6. Zone axis and zone axis orientation. The image schematically shows the [0001] zone axis, which is common to the grey-highlighed planes. When a zone axis is collinear with the electron beam, the crystal is tilted into the zone axis orientation.

3.4.1 Zone Axis Orientation

An important term for practical transmission electron microscopy is a zone axis orientation. It means that a specimen is tilted in TEM with respect to an electron beam so that the beam is collinear with a zone axis of the specimen. An example of a zone axis orientation is also shown in Fig. 6. The zone axis direction [0001] in hcp lattice is common to the highlighted planes and collinear to the incident electron beam. Practical meaning of the zone axis orientation is especially in amplitude and phase contrast imaging, which are the two fundamental imaging techniques in TEM. In these imaging modes, it is very important to tilt the specimen to a low-index zone axis orientation to get the best resolution and the most information from the crystal. The closer the crystal is tilted to the low-index zone axis orientation, the better quality images. Aforementioned advantages of the zone axis orientations arise from a deeper theory of the interaction of electrons with a solid matter (see for example [55, 56, 61]).

4 Physical Metallurgy

This section explains fundamental metallurgical terms and phenomena used for discussion and interpretation of the thesis' results.

4.1 Solidification and Crystallization

Initial amount of pure metallic materials, alloying elements or master alloy in appropriate quantities is heated above the melting temperature to transform to the liquid state. When all constituents are melted, they can be casted into the alloy. After casting, the alloy cools down and solidifies when the temperature drops below the melting point. If the cooling gradient is low to medium, metallic alloys usually form a crystalline structure during solidification. Atoms are periodically arranged in all directions to fill whole space during crystallization. As cast alloys are often subjected to an annealing after solidification process to homogenize their microstructure and composition. This so called homogenization is a heat treatment at a temperature just below the melting point [62].

4.2 Nucleation and Growth

The early process of crystallization from the liquid state is called nucleation. Nuclei are clusters of atoms excluded from the liquid state that arrange themselves to a crystal structure. Highest probability to form a nucleus is at interfaces (for example contact with crucible walls), impurities (atoms of different chemical element) or inclusions. Energy of an alloy is increased by a formation of a nucleus, due to the interface between the nucleus and the liquid. Contrary, energy of the alloy is decreased due to a formation of more stable crystal structure. When the size of the nucleus exceeds the critical diameter, the energy decrease is higher than energy increase and the solid becomes more stable. Nuclei of sufficient size can further grow to fill the space with a crystal structure [60].

It is common that many nuclei of sufficient size are formed in an alloy during cooling. Crystal orientations that grow from different nuclei are independent on each other; therefore an orientation of the crystalline lattice at different sites of the alloy differs. Individual bodies of mass that share the same orientation of the crystalline lattice are called grains. Grain is a term designating a nucleus larger than the critical size that was able to grow up [62]. The grains begin to interact with each other during advanced stage of growth. Planar defects of regular crystal structure are then produced because of misfits of the initial crystalline orientation of particular grains. These defects are called grain boundaries. The process is schematically shown in Fig. 7. Crystalline nuclei A and B are excluded in the melt under the temperature of the melting point and start to grow. They form grains that fill the whole body of mass with a crystalline structure. Initial crystalline orientation of the nuclei is different hence the orientation of the grains is different. When the grains interact with each other during the growth, they form a grain boundary. The crystalline orientation of the material is different at either side of the grain boundary [60].

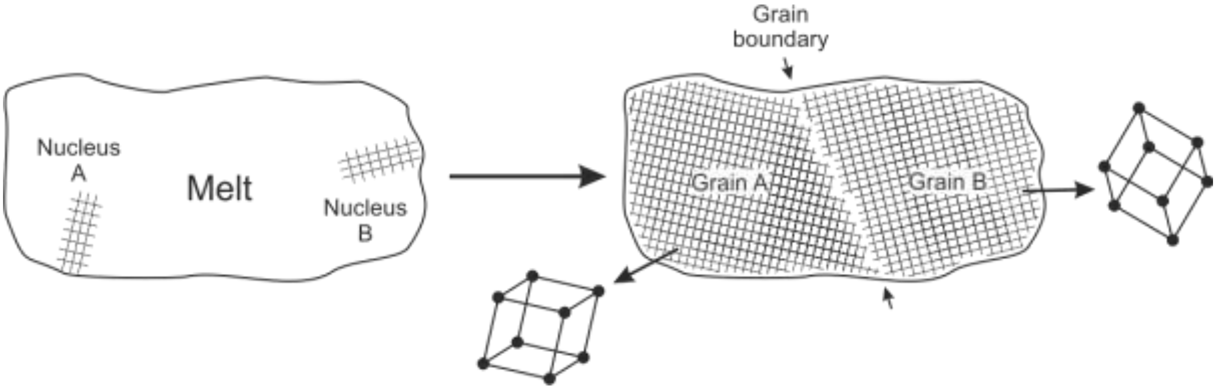

Fig. 7. Nucleation and growth. The image shows schematically the process of nucleation and growth during solidification of a melt to a crystal [60].

4.3 Phase and Solid Solution

Phase is a continuous body of mass with given physical properties. In particular, a chemical composition and a crystal structure have to be the same through the whole body of mass to enclose a single phase. More phases can coexist in a piece of material. A typical example of different phases is particles of impurities in otherwise pure metal. An example of different phases that has the same chemical composition and differ by a crystal structure can be found in the case of iron. The crystal structure of iron at temperatures below 910 °C is the body centered cubic. It is designated as an α-iron phase. The crystal structure of iron at temperatures between 910 °C and 1394 °C is the face centered cubic. It is designated as the γ-iron phase. Contrary, pure copper (or α-copper) that adopts also the face centered crystal structure as the γ-iron is a different phase from the γ-iron [60].

Atoms of two (or more) different metallic elements can be mixed together to form an alloy. When such a mixture is cooled to the solid state, there is a chance that the atoms of the element of lower concentration dissolve in a crystal lattice of the more concentrated element. The amount of atoms of one element that is able to dissolve in the crystal structure of the second element is designated as the *solubility limit*. The solubility limit is dependent especially on a similarity of atomic diameters of particular elements, their crystal structures and temperature of the alloy.

Assume the solubility limit at given temperature of an element A in an element B as 1 at.%. If the concentration of the A atoms in a crystal structure of the B atoms is up to 1 at.%, all the A atoms are distributed within the crystal structure of the B atoms [60, 62].

If the concentration of the A atoms is higher than the solubility limit, excess atoms that do not fit the B element crystal structure are forced to form a *second phase* with an energetically favourable stoichiometric ratio of the A and B atoms. It is generally designated as an A_XB_Y phase. This newly formed phase from the excess atoms can adopt a crystal structure that is different from the crystal structure of the B element and A element. [60, 62].

The solubility limit is temperature dependent. When the solubility limit of atoms A in a crystal structure of atoms B drops below the actual concentration due to a cooling, the excess A atoms are forced to leave the crystal structure of B atoms. They start to form fine particles of a second phase that are dispersed in the B-matrix. The process is designated as *precipitation* and the newly formed particles are called *precipitates* [60, 62].

4.4 Solid State Phase Transformation

Atoms in a material tend to arrange themselves to the most energetically favourable microstructure for given temperature and pressure. When a solidified alloy is cooled to a room temperature (RT) from higher solid state temperatures or the alloy pressure is changed, more favourable arrangement of atoms can occur. The atoms are forced to rearrange themselves to a more stable phase. The newly formed phase can differ not only by a crystal structure, but also by a chemical composition (in the case of alloy). Solid state phase transformations are in general reversible. When the thermodynamic conditions are turned back, the atoms rearrange themselves to the previous phase [60, 62, 63].

4.5 Orientation Relationship

Newly formed body of mass during solid state phase transformations (especially precipitates) can adopt particular alignment toward the matrix. If an important low-index crystallographic direction of its crystal structure is collinear to an important low-index crystallographic direction of the crystal structure of the matrix, orientation relationship occurs. If the majority of the precipitates are formed in the matrix with the same orientation of its crystal structure toward the matrix, they are grown in preferred orientation. Precipitates formed in this way share the same orientation relationship with the matrix. Preferred orientation and orientation relationship are also important during techniques of a material preparation that use growing or deposition of a material on a substrate. The substrate is then often oriented in a zone axis orientation and the new material often adopts an orientation relationship with the substrate.

4.6 Equilibrium Solidification

Equilibrium solidification means that it proceeds during a slow cooling rate by a reversible process [63]. Thermodynamics of equilibrium solidification and solid state phase transformations can be explained using a phase diagram. Phase diagram is a tool for visualization and calculation of concentrations of individual constituents and their quantity in a system. If the system consists of two pure elements that form a binary alloy, a binary phase diagram is used. An example of the most simple binary phase diagram and a procedure for determination of phase, composition and quantities of individual constituents is shown in Fig. 8. Variables of the diagram are the temperature T and the concentration of the individual constituents c_i. Since the phase equilibrium is also pressure dependent, constant atmospheric pressure is assumed through the whole area of the diagram [63].

The A point on the concentration axis determines the pure element A and the B point on the concentration axis determines the pure element B (Fig. 8). In this example, the concentration of individual elements between these two points is expressed in weight percent. There are two most important curves in the diagram called liquidus l and solidus s. At the temperatures above the liquidus curve, the alloy is in the liquid state L for given composition. Contrary, at the temperatures below the solidus curve, the alloy is in the solid state α for given composition. The letter α designates a *solid solution*. The area between the two curves determines the equilibrium of L and α for given temperature and concentration of individual constituents and describes a progress of solidification [60, 62, 63]. The equilibrium solidification is explained for the alloy I.

Concentrations c_A and c_B of corresponding constituents A and B in the alloy I are marked on the concentration axis. Above the temperature given by the point 1, the alloy I is in the liquid state. Solidification starts when the temperature drops to the point 1 and first crystals of the solid solution α are excluded from the melt L. An initial composition of α is determined by a projection of the point 5 onto the concentration axis. Rules for determination of composition and quantity of the L + α solid solution equilibrium are explained for the temperature of the point 2.

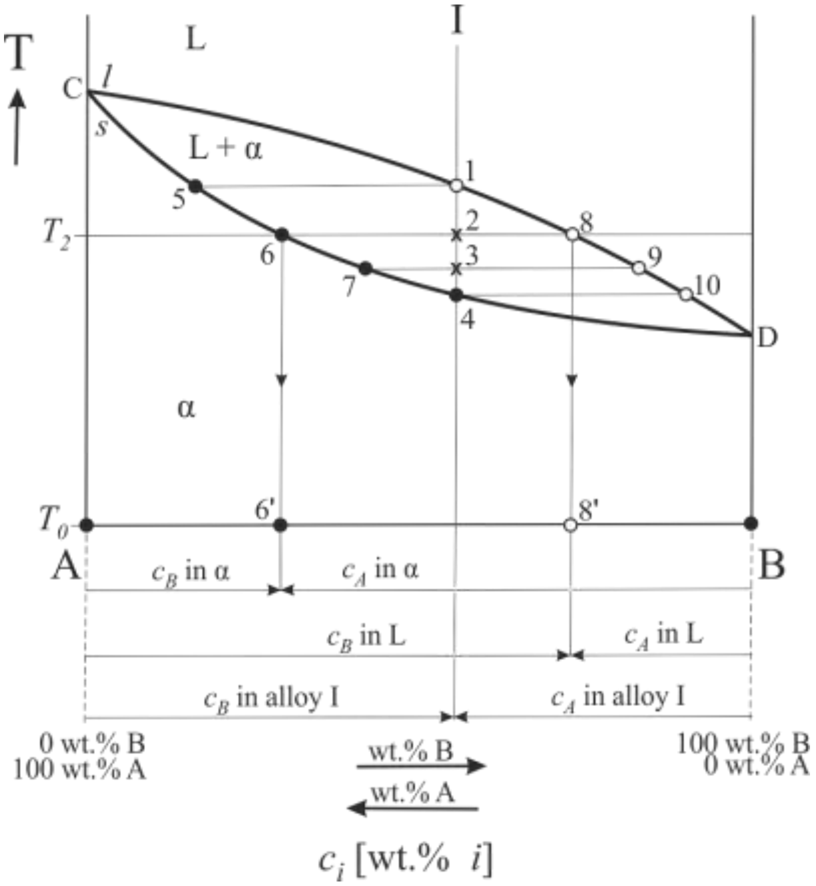

Fig. 8. Binary phase diagram. The image shows the simplest kind of a binary phase diagram showing of basic phenomena during solidification [63].

The point 2 is located inside the L + α area of the diagram. The melt L and the solid solution α coexist in the alloy I at the temperature T_2, as seen from the diagram. The composition of the solid solution α is determined by a projection of the point 6 onto the concentration axis to the point 6´. The concentrations c_A and the c_B in the solid solution α can be read directly from the concentration axis. The composition of the melt L is determined by a projection of the point 8 onto the concentration axis to the point 8′. The concentration c_A and the c_B in the melt L can be read directly from the concentration axis. The quantities of L and α at T_2 in wt.% are determined using the lever rule [60, 63] with the aid of distances defined by the points 2, 6 and 8 (numbers in brackets are related to the Fig. 8):

$$m_\alpha[wt.\%] = \frac{|\,2,8\,|}{|\,6,8\,|}\cdot 100;\ m_L[wt.\%] = \frac{|\,2,6\,|}{|\,6,8\,|}\cdot 100. \tag{4.1}$$

The solidification proceeds to the point 3. The composition of the solid solution α can be determined by a projection of the point 7 onto the concentration axis. The composition of the melt L can be determined by a projection of the point 9 onto the concentration axis. The quantities of L and α at the point 3 in wt.% are determined similarly using the lever rule using distances defined by the points 3, 7 and 9 as follows (numbers in brackets are related to the Fig. 8):

$$m_\alpha[wt.\%] = \frac{|\,3,9\,|}{|\,7,9\,|}\cdot 100;\ m_L[wt.\%] = \frac{|\,3,7\,|}{|\,7,9\,|}\cdot 100. \tag{4.2}$$

The equilibrium solidification terminates at the point 4. The rest of the melt of the final composition determined by the point 10 is solidified. Below the point 4 exists only the solid solution α. The composition of the solid solution α below the *s* curve is given by the point 4 that is the same as the composition of the melt L above the *l* curve. It is the composition of the alloy I.

4.7 Severe Plastic Deformation

When a force is applied on a crystal, the crystal can be deformed. Deformation means that the atoms of the crystalline material are shifted from their original positions. The higher the applied force, the more severe deformation of the material and the atomic displacement. There are two basic possibilities after the force is removed. The atoms are either returned to their original positions or not. When the atoms are returned to their original positions, the deformation is elastic. When the atoms remain displaced, the deformation is plastic. Plastic deformation is connected with a permanent change in the shape of the material and also with a modification of its internal structure. Plastic deformation mechanisms are mostly based on the motion, creation and annihilation of point, line and plane defects such us vacancies, dislocations and interfaces.

In the case of very high forces applied to the considered material accompanied by intensive plastic deformation without cracking, the deformation is called severe plastic deformation (SPD). SPD has serious impact on the change of microstructure of the material and consequently on the properties such us corrosion resistance or mechanical strength. The usual mechanism responsible for the strength improvement during SPD is a grain refinement. During SPD, large amount of defects, particularly dislocations and grain boundaries, are introduced to the material structure. In comparison with as-cast counterparts, an average grain size is reduced by the order of 10^3 to 10^4 and may attain the size of hundreds of nanometres [64].

4.8 Recrystallization

The material after severe plastic deformation contains very high amount of crystal defects. Crystal is strained and a regular grain structure fades away. The material is energetically in a metastable excited state and tends to decrease its energy to a more stable state. The process of getting to the more stable state proceeds by structural changes. An early stage of energy release is usually recovery. The main stage of energy release is recrystallization. In general, the two processes can overlap or one of them can be suppressed. It depends on a material and thermomechanical history of the deformation process. Recrystallization is thermally activated process. However, it can start even at the room temperature, when the amount of deformation of the crystal structure is sufficiently high. While static recrystallization occurs after deformation (usually during subsequent annealing), dynamic recrystallization occurs during deformation itself [62, 65].

Recrystallization starts at places with the highest energy such as second phase particles or grain boundaries whit high concentration of dislocations and point defects. When the recrystallization is complete, the new grains are strain- and defect- free. The recrystallization process can also terminate before the grains are strain- and defect- free. Partially recrystallized structure is preserved in this case. When the recrystallization does not occur at all, the microstructure remains highly deformed [62, 65].

Severely deformed structure lowers its energy during recrystallization. Physical properties of the material (for example the improved strength) can change back toward their initial states. A progress of recrystallization depends mainly on chemistry, amount of deformation, applied temperature and time. In general, the lower the processing temperature is used, the less probability of recrystallization occurence. However, lower homologous temperature usually deteriorates a material formability. The material tends to crack during SPD processing at low homologous temperatures.

4.9 Solidification and Solid State Phase Transformations in Mg-Zn Alloys

Equilibrium solidification and solid state phase transformations in Mg-Zn system are described using the example of the Mg12Zn. It is the key material for the experimental part of the thesis. The binary phase diagram of Mg-Zn system [27] is shown in Fig. 9 and the Mg12Zn alloy marked by the red dotted line. Note: the diagram is drawn in at.% so the alloy is after recalculation placed at about 5 at.% concentration.

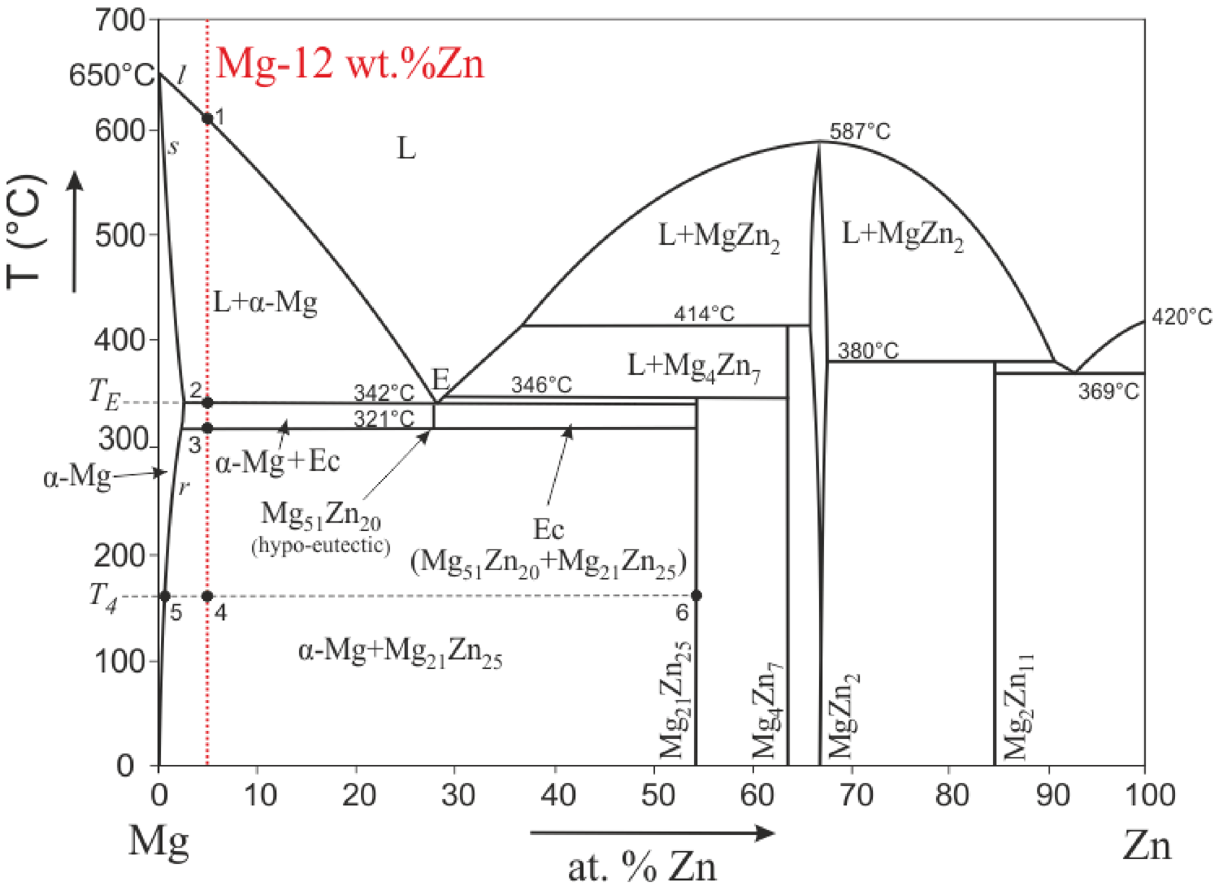

Fig. 9. Mg-Zn binary phase diagram. The image shows Mg-Zn binary phase diagram with highlighted important points concerning a solidification of an Mg-12 wt.%Zn alloy that was used as an experimental material for the thesis [27].

The alloying has to be performed above the temperature of 650 °C to allow complete melt of a raw material. When the melt of Mg and Zn is mixed, the alloying process is finished and the molten alloy starts to cool down.

When the temperature drops to the point 1 (intersection of the alloy composition and the liquidus curve), first crystals of the α-Mg (solid solution of Zn in α-Mg matrix) originate from the melt L. As the cooling proceeds, the composition of the L follows the liquidus curve *l* and the composition of the α-Mg follows the solidus curve *s*. The quantities of L and α-Mg matrix that are in equilibrium at given temperature can be at each instance determined using the lever rule (eq. 4.1) explained in the subsection 4.6.

At the eutectic temperature T_E, the composition of the L reaches the point E and the L undergoes the eutectic reaction [63]. Because the $Mg_{51}Zn_{20}$ compound is hypo-eutectic (its composition is slightly below the composition of the melt right before the reaction), the L is transformed to the eutectic compound E_C that consists of the $Mg_{51}Zn_{20}$ and the $Mg_{21}Zn_{25}$ intermetallic compounds. $Mg_{51}Zn_{20}$ and $Mg_{21}Zn_{25}$ are intermediate phases (see for example [60] or [63]) and their quantities in the E_C can be determined using the lever rule (eq. 4.1). It can be seen from the diagram that between the points 2 and 3, the equilibrium compounds in the Mg-12 wt.%Zn alloy are α-Mg matrix and E_C (that consists of $Mg_{51}Zn_{20}$ and $Mg_{21}Zn_{25}$). The quantities of α-Mg matrix and E_C can be also determined using the lever rule (eq. 4.1).

In the area under the temperature of the point 3, α-Mg matrix and $Mg_{21}Zn_{25}$ are in the equilibrium. Solid state phase transformation occurs during cooling at this temperature. The $Mg_{51}Zn_{20}$ transforms to α-Mg matrix and $Mg_{21}Zn_{25}$ compounds at 321 °C. As the cooling proceeds to the point 4, the composition of the α-Mg matrix follows the *r* curve. The *r* curve represents the solubility limit of Zn in α-Mg matrix in the solid state. It is seen that the solubility limit decreases with temperature. Zn atoms are forced to precipitate from the α-Mg matrix solid solution, as described in subsection 4.4. The most common precipitates in Mg-Zn alloys are $MgZn_2$ and Mg_4Zn_7 intermetallics [3, 4].

There are no more phase transformations except the precipitation under the temperature of 321 °C. An example of phase equilibrium determination is for the temperature T_4. The α-Mg matrix and the $Mg_{21}Zn_{25}$ are phases in equilibrium. The composition of the α-Mg matrix is given by the projection of the point 5 onto the concentration axis. The composition of the $Mg_{21}Zn_{25}$ phase does not change during cooling and is given by the projection of the point 6 onto the concentration axis. The quantities *q* of particular phases (in at.%) are determined using the lever rule (eq. 4.1, numbers in brackets are related to the Fig.9):

$$q_{\alpha-Mg}[at.\%] = \frac{|\,4,6\,|}{|\,5,6\,|} \cdot 100;\; q_{Mg_{21}Zn_{25}}[at.\%] = \frac{|\,5,4\,|}{|\,5,6\,|} \cdot 100. \qquad (7.1)$$

The alloy cools down to the ambient temperature that is usually the RT. The precipitation still occurs down to the RT. However, the lower the temperature, the slower the precipitation kinetics [60, 63].

4.10 Plastic Deformation of Mg

The most important deformation mechanisms in Mg crystals at lower homologous temperatures are dislocation slip and deformation twinning. Dislocation slip is connected with gliding of atomic planes over each other, which is caused by a shear stress applied to a crystal [62, 60]. When the shear stress is high enough toward particular atomic planes, it activates the gliding of the planes. Deformation twinning is connected with a local rearrangement of atoms to the more stable crystalline orientation toward an applied stress. These two deformation mechanisms are depicted in Fig. 10.

Dislocation slip is depicted in Fig. 10a. When a favourably oriented and sufficiently high stress is applied toward a system of particular atomic planes, the planes glide over each other in a certain direction. The direction of glide in hexagonal metals is usually the close packed direction and the gliding planes in magnesium are usually the basal planes. There are also other most probable possibilities in a case of different hexagonal metals. The glide can include for example $\{\bar{1}100\}$ prismatic planes. The combination of glide planes and slip direction represents the slip system. The slip system is designated by the indices of the equivalent glide planes family and the equivalent slip directions family. It is the $\{0002\}$ $< 11\bar{2}0 >$ slip system in the case of Mg [60]. The *c/a* ratio described in the subsection 3.1.2 is one of the most important factors affecting a priority of activation of particular slip systems in hexagonal metals.

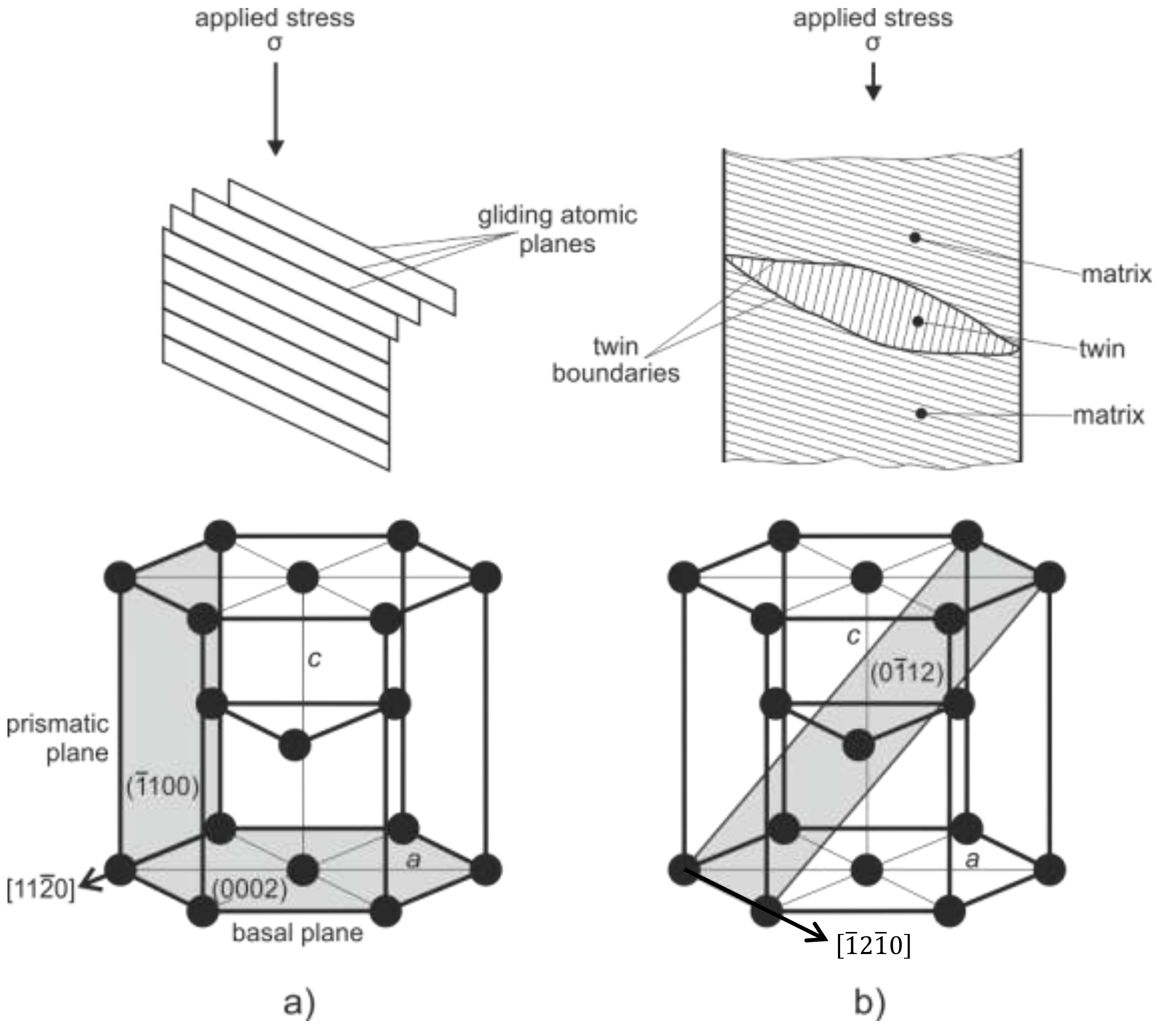

Fig. 10. Example of deformation modes in Mg. a) The image shows schematically dislocation slip that results in gliding of the atomic $\{0002\}$ or $\{\bar{1}100\}$ planes in the $\langle 11\bar{2}0\rangle$ directions as a response to an applied stress; b) the image shows schematically twinning mechanism that results in a rearrangement of atoms in a stressed part of a crystal by mirroring the crystal structure across the $\{0\bar{1}12\}$ twinning planes in the $\langle 11\bar{2}0\rangle$ directions [36].

If the conditions for activationt of the slip mechanism are not complied, Mg can still deform by twinning. The twinning is shown in Fig. 10b. The stressed part of a crystal structure is deformed by rearrangement of atoms across the mirror plane to form the twin. The twin has the same crystal structure as the surrounding matrix, however, the orientation of the twin crystal lattice is mirrored by the twinning plane [60]. An example of the most common twinning in Mg is shown in Fig. 10b. The twinning plane is the $(0\bar{1}12)$ plane and the twinning occurs in the $[\bar{1}2\bar{1}0]$ direction. When the crystal lattice of Mg twins in the $(0\bar{1}12)[\bar{1}2\bar{1}0]$ twinning system, the basal planes of twin and matrix are inclined toward each other by ~ 86 °

that is schematically shown in Fig. 10b. The basal planes are indicated by the lines. This kind of twin is designated as the $(0\bar{1}12)[11\bar{2}0]$ twin. The *c/a* ratio (see the subsection 3.1.2) is also important factor affecting a probability of activation of a particular twinning mechanism in hexagonal metals.

5 Specimen Preparation

Specimen preparation is a critical task for TEM technique. Namely, the thickness of a metallic specimen has to be < 200 nm to enable transparency for electrons and to get reliable experimental information. For some techniques, e.g., high-resolution imaging, the maximal useful thickness is about 20 nm [55]. The specimen after preparation has to represent the same microstructure as the initial bulk material. This fact needs to be kept in mind when setting parameters for the preparation procedure. Inadequate preparation parameters can result in preparation artefacts or in a change of specimen microstructure. Specimen surface has to be clean and without oxidation layer to ensure good visibility and minimize erroneous data. In summary, following conditions need to be complied for the specimen to be suitable for TEM experiments [66, 67]:

- thickness from 1 to 200 nm (according to the TEM technique to be used)
- unchanged microstructure during preparation
- no preparation artefacts
- clean surface

5.1 Preparation Methods Overview

Various methods are used for TEM specimen preparation. In this thesis, only the preparation techniques of TEM specimen from bulk materials are described. Each preparation method has its advantages and disadvantages. The choice depends mainly on the physical and chemical properties of specimen material. Nowadays, the the most widely used methods for bulk specimen preparation are:

- Ion milling
- Electrolytic polishing
- Wedge polishing
- Focussed ion beam

5.1.1 Ion Milling

Ion milling uses the energy of accelerated Ar^+ ions that bombards the centre of the specimen to remove its material until perforation. Cross-sectional view of Ar^+ milling is in Fig. 11. Edges of the perforation are suitable for TEM experiments. Specimens for ion milling are usually pre-processed by grinding down to about 50 μm and punching of discs with diameter of 3 mm. The disc is rotated in the milling machine chamber to ensure uniform and smooth perforation. Materials with poor thermal conductivity are cooled using liquid nitrogen to prevent their overheating. Modern milling devices include light microscope to inspect the specimen during milling and systems for control of the perforation. Milling time ranges from 1 up to 15 hours, with dependence on material, milling parameters and initial specimen thickness. However, the process is fully automated. Ion milling provides smooth and clean surface with relatively large field of view. Despite Ar^+ inertness, possible artefact is Ar^+ implantation into the microstructure [66, 67].

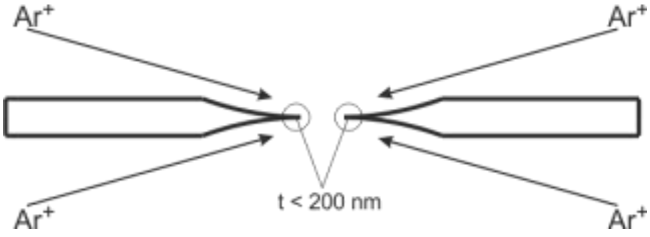

Fig. 11. Ion milling. The disc specimen with diameter of 3 mm and thickness about 50 μm is rotating inside the milling machine. Beam of Ar ions bombards specimen centre until perforation. Edges of the perforation are suitable for TEM experiments [66].

5.1.2 Electrolytic Polishing

This method is also called twin-jet polishing. Its principle is removing of the specimen material by electrochemical reaction. Specimen itself is the anode. Twin jets of an electrolyte are focussed to the specimen centre from both sides, providing connection to the cathode (Fig. 12). Specimen material is dissolved in the electrolyte and passes to the cathode. Before electrolytic polishing, the specimen is grinded down to about 150 μm. Discs with diameter of 3 mm are then punched and placed into the electrolytic polishing specimen holder. Devices for the electrolytic polishing are also equipped with systems for automated detection of the perforation and control of the perforation size. Advantages of this method are very fast thinning rate and the largest field of view. Specimen preparation takes only a few minutes. In contrast to Ar^+ milling, disadvantage of electro polishing is much more demanding selection of variable conditions for the procedure. The most important parameters to be controlled at once to achieve a proper result are suitable chemical composition of the electrolyte, preparation temperature, voltage, flow rate and perforation size. The electrolytic polishing is not applicable for all materials. Attention has to be paid to electrochemical potentials of specimen and cathode to conduct the electrochemical reaction properly. Possible artefacts are products from the electrochemical reaction such as oxidation or passivation layers [66, 67].

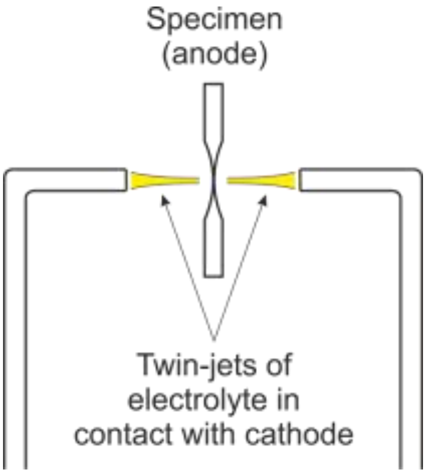

Fig. 12. Electrolytic polishing. The specimen is connected to the anode potential. Twin jets mediate connection between the cathode and the electrolyte focussed to the specimen centre. Specimen material is removed by the electrochemical reaction until perforation [66].

5.1.3 Wedge Polishing

In this case, a wedge with an angle of about 1–2 ° is created using a tripod polisher (Fig. 13). The specimen is wax-mounted to the base of the tripod polisher and the angle is controlled by adjusting of three micrometers. The specimen is mechanically polished on a diamond lapping film down to a thickness of electron transparency. Finally, the surface damage caused by mechanical grinding and polishing can be removed by ion milling for a very short time. This method is often used for preparation of specimens from multilayered materials. On the other hand, it is not well suited for soft materials (for example Mg alloys). Wedge polishing provides high-quality specimens; however, it needs very good skill in mechanical grinding and patience during the slow polishing [66, 67].

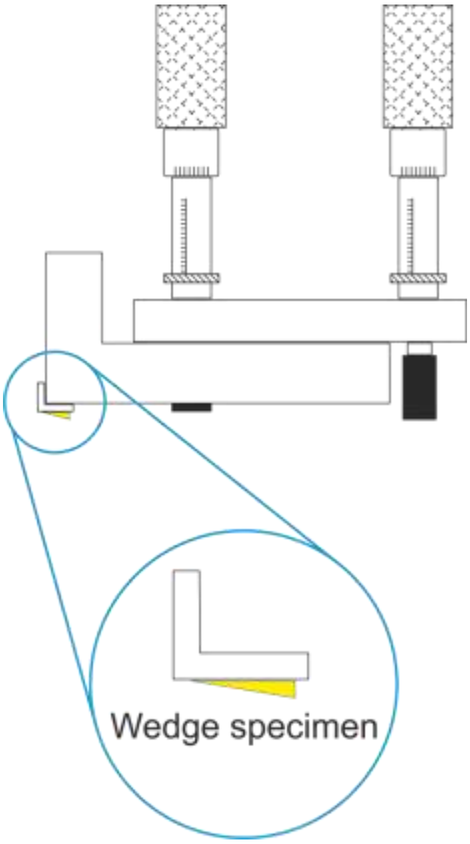

Fig. 13. Wedge polishing. The specimen is mechanically ground and polished using tripod polisher. Electron transparent wedge with angle of about 1-2 ° is formed. The angle is adjusted by three micrometers [66].

5.1.4 Focussed Ion Beam

Focussed ion beam (FIB) method has similar principle as the ion milling described in the subsection 5.1.1. Specimen material is removed by a beam of Ga^+ ions (other elements are seldom used). Nowadays, FIB is usually attached to SEM resulting in two-beam microscope. Specimens are first directly cut from a bulk material by FIB, with the aid of navigation by SEM. After that, the thinning process is conducted by FIB supported by SEM observation for fine tuning of milling parameters. The procedure is schematically shown in Fig. 14. The main advantage is possibility to cut the specimen from a region of interest in the bulk material, for example an interface of two phases or grains. Cross-sectional specimens of layered material can also be prepared using FIB. Disadvantage is possible chemical reaction of Ga^+ from the beam and other elements (C, Pt) from organometallic precursor used for protection of the material during shaping and manipulation. Artefacts may arise from reactions of specimen material with the aforementioned elements. If too high energy of FIB is used, the specimen can also undergo overheating followed by phase transformation. The FIB method has high demands on the operator´s skills [66–68].

Fig. 14. Focussed ion beam. The specimen is first cut out from the bulk material by FIB (on the left). The beam is then used also for the thinning process (on the right) [66].

6 Interaction of Electron Beam with Solid Crystal

An interaction of an accelerated electron beam with a solid matter is the most important aspect in TEM to obtain, understand and interpret the data. A vast amount of signals are generated when accelerated electrons hit a specimen, see Fig. 15. Each type of signal carries a different type of information about the specimen. Selection of signals can be controlled by setup of electron optics, apertures and image recording system of the microscope. Each of the generated signals can be in principle detected in a TEM; however, some of them are more convenient to be detected in a more dedicated instrument.

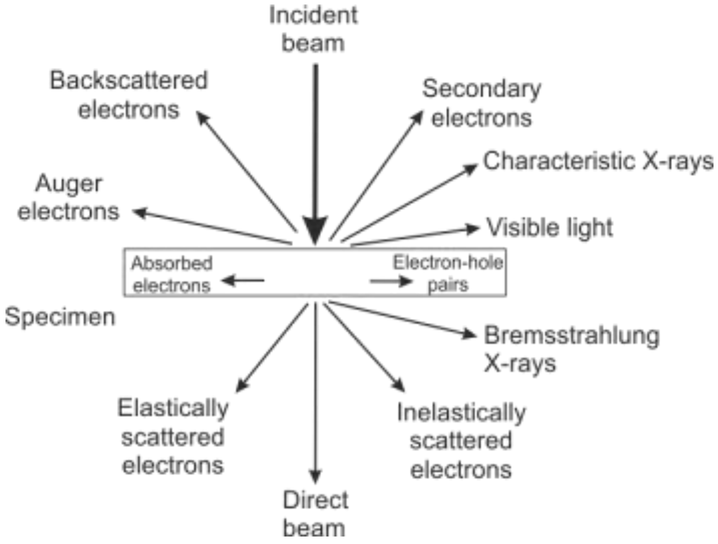

Fig. 15. Interaction of electron beam with solid crystal. The image shows schematically signals generated when an incident beam of accelerated electrons hits a specimen (redrawn from [55]). Each of the generated signals carries different information about the specimen and can be detected.

6.1 Origin of Signals

6.1.1 Backscattered Electrons

Backscattered electrons (BSE) arise from scattering of the primary electrons to angles higher than 90 degrees with respect to the incident direction. Electrons scattered to such a high angle leave the specimen surface at the same side they entered it (the upper side). BSE provide an atomic number contrast. They are usually detected in a scanning electron microscope (SEM) than in TEM.

6.1.2 Secondary Electrons

Secondary electrons (SE) are low energy electrons ejected from the specimen and carry information about the specimen surface topography. They are usually detected by SEM.

6.1.3 Characteristic X-rays and Auger Electrons

Characteristic X-rays and Auger electrons are radiations that are emitted during relaxation of electronic states excited by the primary electron beam. Auger electrons carry information about specimen surface chemistry and are best detected by dedicated Auger spectrometer. Characteristic X-rays carry information about chemistry from the specimen interior. Most TEMs are equipped with an energy-dispersive spectrometer (EDS) that detects characteristic X-rays.

6.1.4 Inelastic Scattering

Inelastically scattered electrons are produced by an interaction of primary beam electrons with an electronic structure of specimen atoms. An incident beam electron loses an amount of energy that depends on specimen material and the kind of interaction. These electron loses are detected by an electron energy-loss spectrometer (EELS) attached to TEM and carry information about specimen chemistry and electronic structure.

6.1.5 Elastic Scattering

Elastically scattered electrons come especially from a diffraction of primary beam electrons on the crystal structure of the specimen. Atomic planes that are in the Bragg condition (described in the subsection 6.2.1) with respect to the incident beam diffracts the incident beam electrons to different angles. It is dependent on interplanar spacing and spatial orientation of the atomic planes. When the direct beam (see 6.1.7) and diffracted beams are recorded simultaneously, interplanar spacing of appropriate atomic planes and their spatial orientation can be determined. Diffraction in TEM is therefore the fundamental tool for crystal structure identification.

6.1.6 Direct Beam

Direct beam represents electrons that were not elastically scattered (diffracted) by the crystal structure of a specimen. Their momentum was not changed and they propagate on the optic axis through the projector system to TEM detectors. Direct beam is a common feature in a TEM and is ued in the majority of TEHm techniques.

6.1.7 Absorbed Electrons, Electron-Hole Pairs and Bremsstrahlung X-rays

Absorbed electrons or electron-hole recombination are in general of no interest in electron microscopy, as well as so called Bremsstrahlung X-rays. Bremsstrahlung X-rays is a radiation with continuous spectrum generated by slowing down of the primary beam electrons by atomic nuclei of the specimen.

6.2 Image Formation

6.2.1 Diffraction Pattern

Diffraction is a general term for an elastic scattering of a radiation on a crystal structure of a solid matter. While the thesis deals with electron diffraction only, the physics described in this section is similar for electron, neutron or X-ray radiation.

A beam of radiation (Incident beam) in the form of a plane wave falls onto a system of atomic planes in the crystal structure of a specimen at an angle of incidence θ (Fig. 16). When a path difference between a beam diffracted at a reference plane and a beam diffracted at a first-order diffracting plane is equal to a wavelength of the radiation, the diffraction condition for constructive interference is satisfied and the diffracted beam remains coherent. The angle of incidence of the beam that ensures a satisfaction of the diffraction condition is called the Bragg angle and is dependent on chemical composition of material and its crystallography.

In case the diffraction condition is satisfied for the system of crystallographic planes with respect to the incident beam, the plane system act as a semipermeable mirror and diffracts the beam. Constructive interference of diffracted wave then produces a diffraction pattern. The diffraction condition for the case depicted in Fig. 16 is [55, 60]:

$$CB + BD = \lambda. \tag{6.1}$$

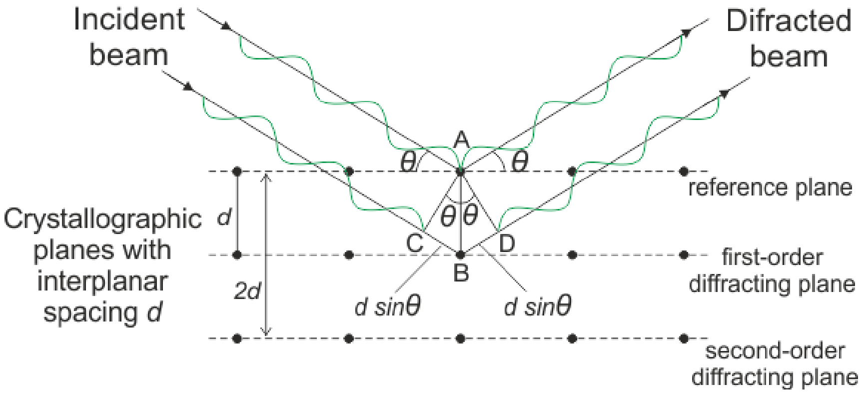

Fig. 16. Illustrative outline showing geometry of Bragg diffraction: d – interplanar spacing, θ – angle of incidence [59].

The diffraction conditions is that the path difference $CB + BD$ between waves diffracted on adjoining crystallographic planes with the interplanar spacing d has to be equal to the wavelength λ of the incident radiation. Rewritten in more practically oriented form, the diffraction condition passes to the Bragg law:

$$2d \cdot sin\theta = \lambda, \tag{6.2}$$

where θ represents the Bragg angle of the system of crystallographic planes. In the above form the law is valid only for a system of two planes, one reference plane and first-order diffracting plane. If we add the third collinear plane in the same interplanar spacing to the system, the path difference between waves diffracted from the reference plane and second-order diffracting plane would be equal to 2λ.

It is equivalent to considering the second-order diffracting plane as the first-order diffracting plane with interplanar spacing *2d*. Number of planes in a system can be in general unlimited. Dimensions of TEM specimens involve typically tens to thousands of atomic planes. Complete form of the Bragg law is therefore necessary:

$$2d \cdot sin\theta = n\lambda, \tag{6.3}$$

where *n* now represents the order of the diffraction.

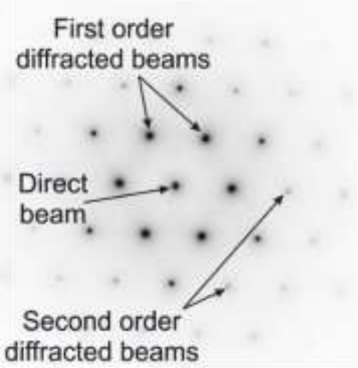

Fig. 17. Electron diffraction pattern. The electron diffraction pattern shows spatial arrangement of a direct beam and diffracted beams acquired from a magnesium crystal in the [0002] zone axis orientation. The pattern reflects symmetry of a crystal and lattice parameters of a unit cell. Note: the intensity of the pattern image was inversed [experimental data of this work].

When the crystalline specimen is tilted so that more systems of crystallographic planes form the Bragg angle with respect to the incident beam, diffraction condition is satisfied for all these systems simultaneously. Diffraction pattern is then a two-dimensional dataset with the intensity of the direct beam in the centre and the diffracted intensities from appropriate plane systems around (Fig. 17) [55, 61].

6.2.2 Amplitude Contrast

Amplitude contrast describes the origin of conventional TEM images at lower magnifications. Electron beam treated as a plane wave illuminates a specimen. If the specimen is crystalline, it diffracts some of the incident wave intensity to different angles, because of a presence of crystallographic planes. Objective lens of the microscope acts to sum the diffracted beams and the direct (non-diffracted) beam back together in the image plane of the objective lens. In Fig. 18a, only two beam case (direct and diffracted beams) is shown for simplicity. Both direct and diffracted beams contribute to the image intensity that is therefore dependent mainly on the thickness and the mass of the illuminated specimen area. The contrast in the image is usually poor in this case.

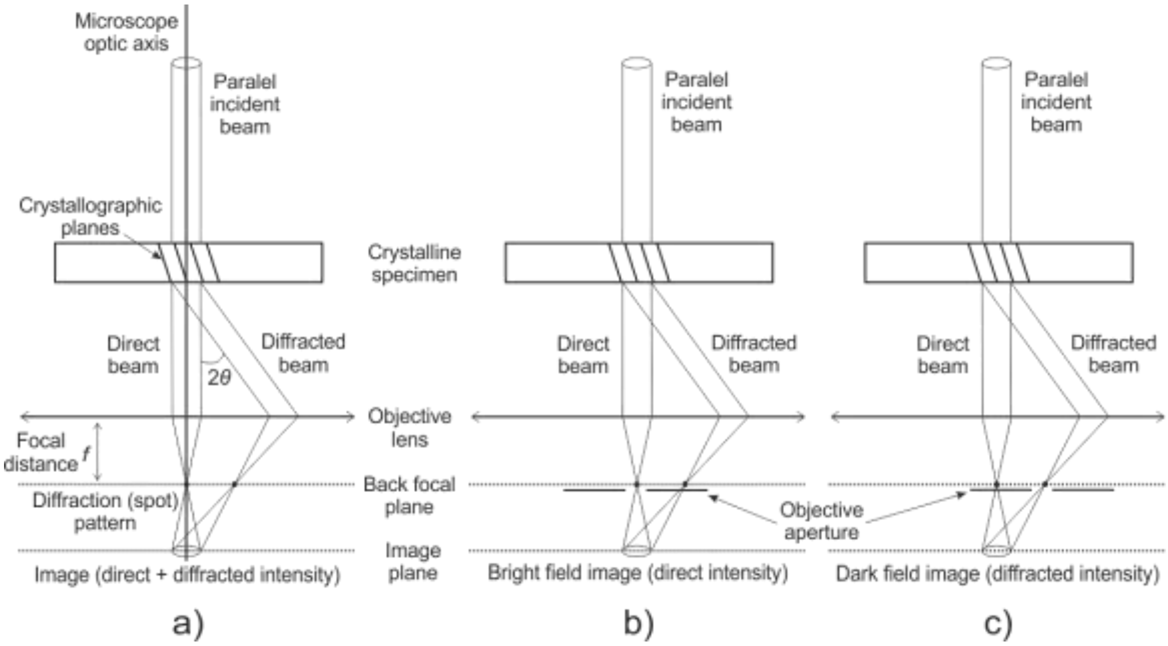

Fig. 18. Amplitude contrast (drawn on the basis of [61]). a) The image shows schematically a formation of an amplitude contrast image of a specimen by composition of a direct and a diffracted beam in an image plane of an objective lens; b) The image shows schematically a formation of a bright field image using the objective aperture to select only the direct beam to contribute to the image of the specimen; c) The image shows schematically a formation of a dark field image using the objective aperture to select the diffracted beam to contribute to the image of the specimen.

TEM has a capability of a spatial filtering of these spatially spread beams using the objective aperture. Only the direct beam or only the diffracted beam can be chosen to contribute to the image. When only the direct beam intensity contributes to the image, the image is called the *bright field* image, see Fig. 18b. When only the diffracted beam intensity contributes to the image, the image is called the *dark field* image, see Fig. 18c. The image contrast is enhanced using the objective aperture to highlight features of the specimen that cause the beam to be diffracted. In all described cases the image intensity comes from the interference of the amplitudes of the electron waves in the image plane of the objective lens [55, 61, 69].

An example of a bright field and dark field image of the same grain boundaries is shown in Fig. 19. Bright field image (Fig 19a.) was formed by selection of only the direct beam using the objective aperture. Dark field image (Fig. 19b) was formed by selection of only the diffracted beam using the objective aperture. Objects that are close to diffraction condition appear darker in the bright field image and brighter in the dark field image. Defects in grain boundaries satisfying diffraction condition are rather notable in the dark field image (Fig. 19b). Related diffraction pattern (Fig. 19c) shows direct beam and diffracted beam selected for the image formation [61].

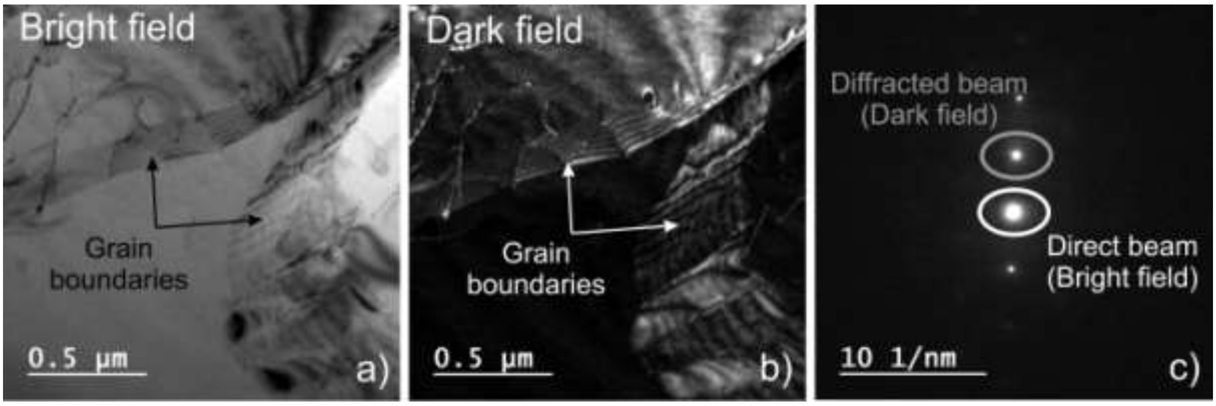

Fig. 19. Amplitude contrast example. a) the bright field image was formed by selection of only the direct beam. b) the dark field image was formed by selection of only the diffracted beam. c) related diffraction pattern. Ti specimen [by courtesy of V. Gärtnerová].

6.2.3 Phase Contrast

Phase contrast describes origin of a high-resolution image from crystalline material at high magnifications. High-resolution image has its origin in the mutual interference of diffracted beams and the direct beam inside a specimen. It emerges from the specimen in the form of exit wave. The exit wave is than formed to the high-resolution image by the objective lens. The image is composed of minima and maxima of the exit wave. The minima and maxima depend particularly on a crystal structure, orientation and thickness of the specimen and on a defocus of the objective lens [55, 69].

Interpretation of phase contrast high-resolution images is not straightforward. With a dependence on crystal structure, thickness and orientation and objective lens defocus conditions, either minima or maxima of the exit wave can correspond to atoms or atomic columns in the crystal structure of the specimen. In special cases, the exit wave even shows additional minima or maxima that do not correspond to atoms or atomic columns. The problems with the interpretation can be solved with the aid of image simulation or various exit wave reconstruction algorithms. The formation of the exit wave and the phase contrast high-resolution image is schematically depicted in Fig. 20a. The intensity of the image is periodically variable and depends mainly on the specimen thickness and the objective lens defocus [55, 69]. An example of high-resolution image is shown in Fig. 20b.

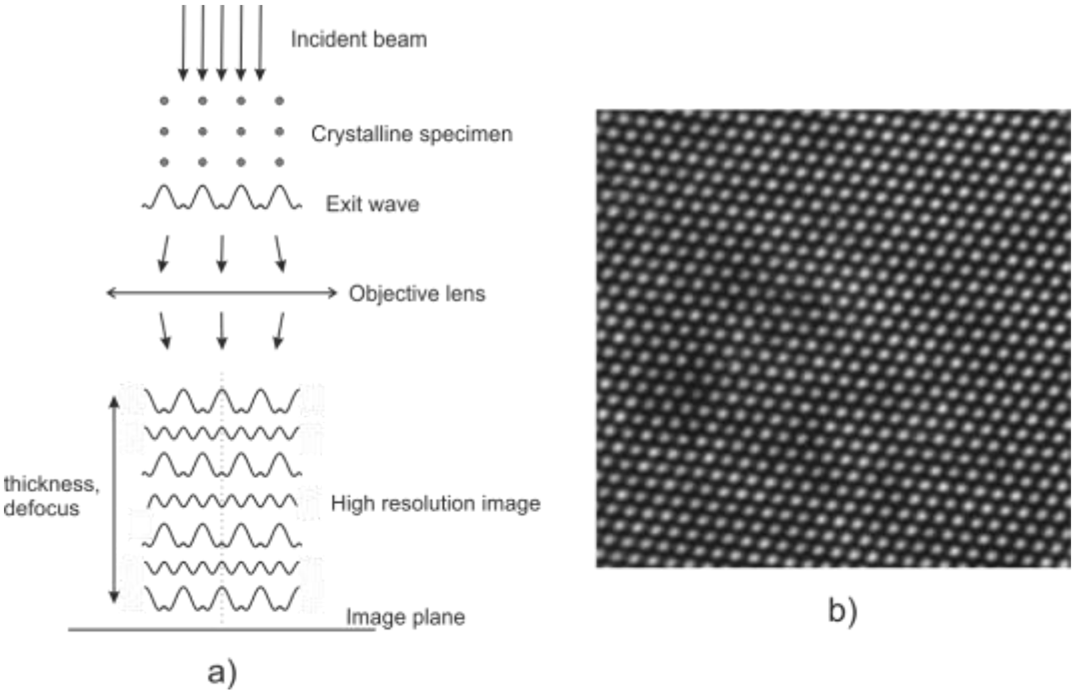

Fig 20. Phase contrast image. a) The image schematically shows an origin of an exit wave and subsequent formation of a high resolution phase contrast image by an objective lens [redrawn from 69] b) High-resolution TEM image shows phase contrast image from an Mg12Zn specimen tilted to the [0002] zone axis orientation [experimental data of this work].

6.3 Electron Spectroscopy

Electron spectroscopy is the most important analytical technique in both industry and materials science. In TEM, there are two the most commonly used electron spectroscopy techniques: Energy-dispersive spectroscopy (EDS) and Electron energy-loss spectroscopy (EELS). Both of them rely on the interaction of incident beam electrons with electronic structure of specimen atoms (Fig. 21).

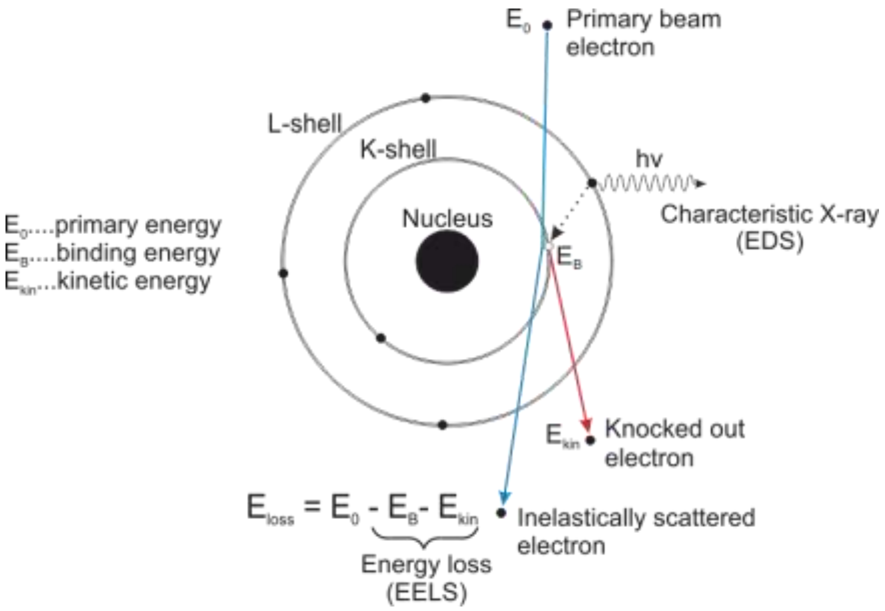

Fig. 21. Electron spectroscopy. The image shows the origin of a spectroscopic signal used in TEM.

Primary electron beam propagates through the specimen with a path close to an atomic nucleus. Kinetic energy of the primary beam electron is based on accelerating voltage of the microscope that is typically in the range of 80–300 kV. This energy is high enough for the primary beam electron to knock-out tightly bounded K-shell electron from the atomic nucleus of the specimen. However, the K-shell electron is bonded to its nucleus by characteristic binding energy. The primary beam electron has to transfer at least the amount of its kinetic energy to the K-shell electron that is equal to the K-shell electron characteristic binding energy. There are two basic consequences of this interaction.

The first one, the specimen atom with knocked-out electron from its K-shell is at an unstable excited state and tends to relax to a more stable state. It is energetically favourable for an L-shell electron to jump to the hole in the K-shell. High excitation energy of the atom is then lowered. This energy cannot simply vanish. It is radiated from the atom in the form of photon with a wavelength in an X-ray spectrum. This radiation is detected using EDS detector in TEM as characteristic X-rays that carry the information about the chemical composition of the specimen [55].

The second one, the kinetic energy of the primary beam electron is lowered. The primary beam electron suffers an energy loss that is equal to the binding energy E_B of the knocked-out electron from the atom electronic structure. Electrons that lose an amount of energy can be detected using electron energy-loss spectrometer. These electrons also carry information about specimen chemistry and the technique that deals with them is called electron energy-loss spectroscopy (EELS) [55, 70].

7 Results and Discussion

7.1 Material and Methods

7.1.1 Casting

Magnesium with 99.9% purity and an appropriate amount of high-grade zinc were melted in a graphite crucible under an Ar atmosphere to prepare two binary magnesium alloys with a nominal composition of Mg6Zn and Mg12Zn.

7.1.2 Heat Treatment

Subsequent thermal treatment consisted of annealing at 320 °C for 20 h to homogenize the microstructure and quenching in warm water – homogenization heat treatment. This state is hereafter referred as the initial state.

7.1.3 Severe Plastic Deformation

The material was then processed by ECAP-BP (Fig. 22). The following processing parameters were used: a die inter-channel angle of 90° and a corner angle of 0°, 4 passes via a Bc route, and an applied back pressure of ~400 MPa to prevent cracking during processing. The processing temperature for Mg6Zn was 220 °C, 220 °C, 220 °C and 160 °C for the 1st, 2nd, 3rd and 4th ECAP-BP pass, respectively. The processing temperature for Mg12Zn was gradually decreased from 200 °C to 185 °C, 170 °C and 155 °C for the 1st, 2nd, 3rd and 4th ECAP-BP pass, respectively. In both cases, ECAP geometry leads to an imposed strain of ~1.15 per pass.

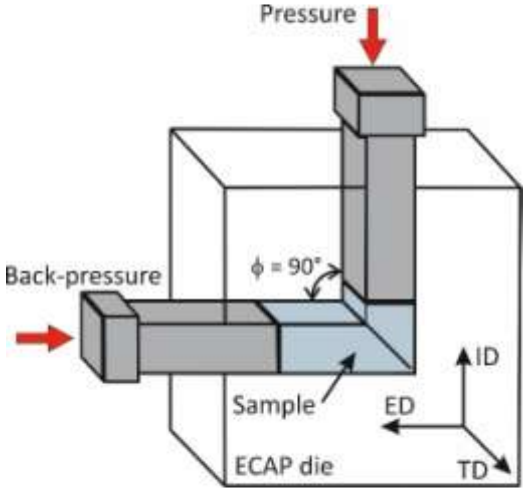

Fig. 22. Schematic drawing of ECAP die with back pressure (BP). Orientation between the compression axis and the coordinates of the specimen after the ECAP-BP processing is marked by ID, ED and TD arrows. (ID – insert direction, ED – extrusion direction, TD – transverse direction, ϕ – die inter-channel angle).

7.1.4 Microstructure Observation

Specimens for metallographic observation were prepared by conventional cutting (ID-ED plane for specimens after ECAP-BP (see Fig. 22 for notation), grinding and polishing followed by etching in a 5% picric acid solution. The microstructure was examined using light microscopy (LM) with a Zeiss Axio Observer D1m and scanning electron microscopy (SEM) with an FEI Phenom.

Thin foils for the transmission electron microscopy (TEM) observation were prepared by grinding of 3 mm disks down to a thickness of approximately 50 μm and subsequent Ar ion polishing using a Gatan PIPS.

The following TEM techniques were employed for micro- and nano-structural analysis: bright-field (BF) imaging, selected area electron diffraction (SAED), convergent beam electron diffraction (CBED), high-resolution transmission electron microscopy (HRTEM), high-angle annular dark field-scanning transmission electron microscopy imaging (HAADF-STEM) and electron energy-loss spectroscopy (EELS). Each of these TEM techniques was performed using an FEI 52 TF20 X-twin operated at 200 kV and equipped with a GIF Quantum SE. The EELS data were processed using Gatan Digital Micrograph.

In-situ high-resolution transmission electron microscopy (In-situ HRTEM) was performed for nanoparticle growth observation using a DENSsolutions Double Tilt (DH30) heating system. Thin foils for the in-situ HRTEM were prepared using the FIB technique performed with an FEI Quanta 3D FEG. The diffraction pattern images and HRTEM images were processed using the CrysTBox software [72].

Precession-assisted Electron diffraction tomography (PA-EDT) was performed on Philips CM 120, which operated at 120 kV and equipped with a NanoMEGAS precession unit DigiStar. For the structure determination, a precession angle of 1° was used, whereas the data for the orientation relationship examination were recorded without precession. The EDT data were processed using the PETS software [73]. The structure solution was performed by charge flipping using the Superflip software [74], and the structure was kinematically refined in the software Jana 2006 [75].

7.1.5 Mechanical Testing

Mechanical properties were characterized using uniaxial compression tests at constant initial strain rate. Specimens for the compression tests from the Mg6Zn and Mg12Zn after ECAP-BP were cut along three (ID, ED and TD) directions by electrical-discharge machining. The nomenclature used for the description of the orientation between the compression axes and the coordinates of the ECAP-BP billet are shown in Fig. 22. Compression specimens with dimensions of 4x4x8 (width x thickness x length) mm^3 were deformed at a strain rate of 1.1×10^{-3} s^{-1} using an Instron 5882 machine at room temperature. At least two measurements were performed for each orientation to verify reproducibility. All compression tests were performed to specimen rupture.

7.1.6 Corrosion Testing

Corrosion properties were investigated by the measurement of a corrosion rate using a hydrogen evolution method [76]. Specimens for corrosion rate measurement were prepared by conventional cutting (ID-ED plane for specimens after ECAP-BP, see Fig. 22) and grinding. They were subsequently immersed in static 9 g/l NaCl solution at a temperature of 37 °C (simulation of human body temperature). To prevent dissolution of the hydrogen released from the specimens in the NaCl solution, the solution was saturated with hydrogen prior to exposure of the specimens. Each specimen was exposed in the NaCl solution for 26 hours. The amount of hydrogen released from the specimens was recorded for the first and the last two hours of the exposure time at ~15 min intervals. Prior to each measurement, the pressure of the released hydrogen was adjusted to the atmospheric pressure. The adjustment of the hydrogen pressure was performed using a compensatory vessel with mercury connected to the burette. The indicatory manometer was filled by a dodecane ($C_{12}H_{26}$) hydrocarbon to prevent the dissolution of the hydrogen released from the specimen as well.

7.2 Mg12Zn Initial Microstructure

Typical microstructure of an Mg12Zn specimen after annealing at 320 °C / 20h with subsequent quenching is shown in Fig. 23. The microstructure consists of grains created by the α-Mg matrix (supersaturated solid solution of Zn in Mg) and many Mg-Zn particles with different morphologies distributed uniformly within the α-Mg matrix (Fig. 23a). The SEM micrograph (Fig. 23b) reveals two types of Mg-Zn particles: larger lengthy ones (white arrows) and smaller globular ones (black arrows). These particles, which are greater than 1 μm, are marked as A-microparticles hereafter. A detail of the microstructure in the TEM bright-field (TEM BF) image demonstrates the presence of other nano-scaled particles in the α-Mg matrix with dimensions of either approximately 100 nm, which are marked as B-nanoparticles (Fig. 23c), or approximately 5 nm, which are marked as C-nanoparticles (magnified inset in Fig. 23c). The crystal structure and orientation relationship of all particles found in the microstructure were analysed and described in separated sections.

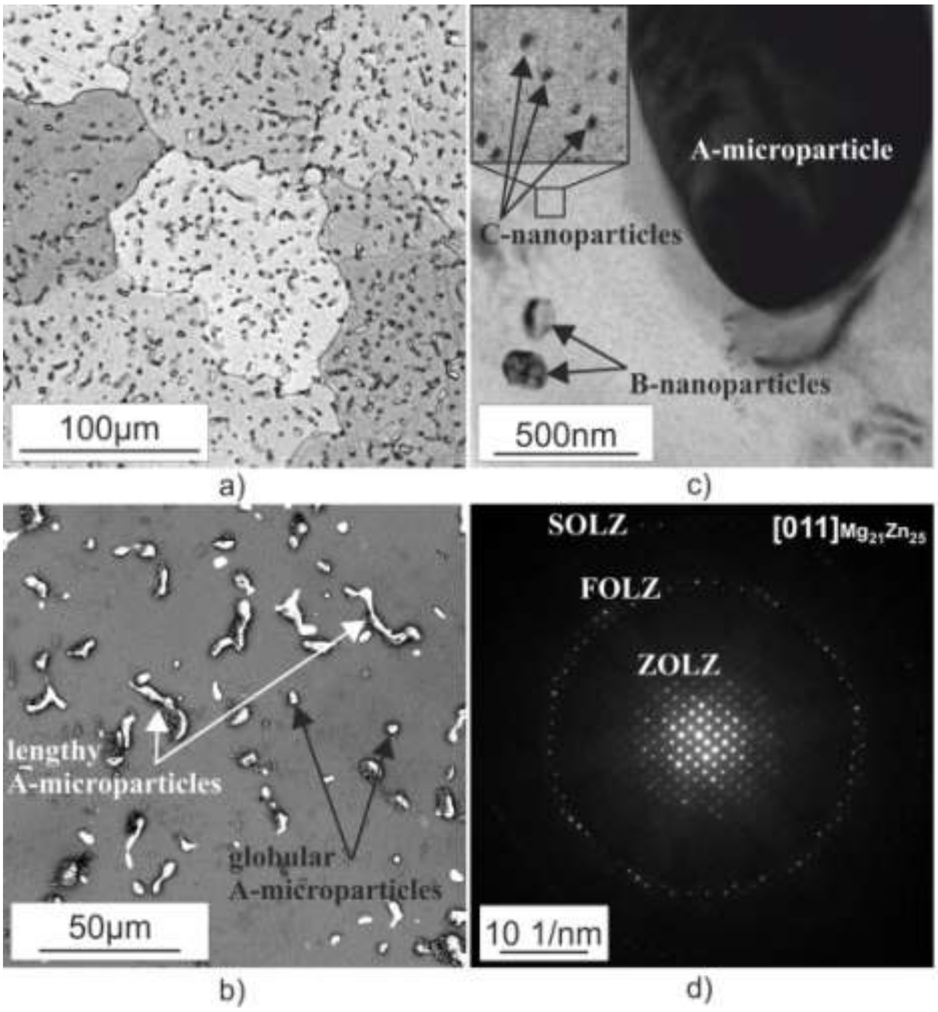

Fig. 23: General overview of microstructure of the Mg12Zn alloy in the initial state. a) LM image showing grains of α-Mg matrix and A-microparticles distribution, b) SEM image showing two different shapes of A-microparticles – lengthy and globular, c) TEM BF image demonstrating B-nanoparticles with dimensions of approximately 100 nm, C-nanoparticles with dimensions of approximately 5 nm (magnified in the inset) and a typical view of the A-microparticle in a zone axis orientation, d) SAED pattern from the A-microparticle in c) identified as a pattern from the crystal structure of the $Mg_{21}Zn_{25}$ phase in the $[011]$ zone axis orientation.

7.3 Particles in Mg12Zn Initial Microstructure

7.3.1 A-microparticles

Two different electron diffraction techniques (SAED and PA-EDT) were used to identify a crystal structure of the A-microparticles. The zone-axis SAED patterns from various morphologies of A-microparticles were acquired and evaluated using the CrysTBox software. Fig. 23d shows one of the examined SAED patterns, which were taken from an A-microparticle. The pattern well fits the crystal structure of an $Mg_{21}Zn_{25}$ phase described by Černý and Renaudin [24] oriented to the [011] zone axis. All inspected A-microparticles, which were lengthy and globular, were well fitted to this structure. There is likely no experimental work that unambiguously associates the morphology of $Mg_{21}Zn_{25}$ particles with their direct identification in a microstructure of any Mg-Zn-based material. Hence, it was essential to verify the SAED analysis using a more reliable method, like PA-EDT.

7.3.1.1 Precession-assisted Electron Diffraction Tomography

The PA-EDT is an experimental technique that allows direct measurement of 3D diffraction information from nanocrystals. The diffraction data are acquired by sequential tilting of a crystal in a TEM, and acquiring diffraction pattern at every tilt step [77]. The acquired data can be treated in a way analogous to standard procedures used in single-crystal X-ray diffraction [78], especially if combined with precession electron diffraction [79]. The technique thus allows also the space group determination and *ab initio* structure determination.

Experimental data from several A-microparticles of both lengthy and globular types were acquired. The crystal structure was solved as trigonal with the $R\bar{3}c$ space group and lattice parameters a ~ 2.6 nm and c ~ 0.89 nm (Fig. 24). The structure model (Fig. 24b) is notably consistent with the previously reported structure of $Mg_{21}Zn_{25}$ and thus confirms the results in [24]. Several A-microparticles were examined to find their orientation relationship toward the α-Mg matrix; however, no fixed orientation was observed.

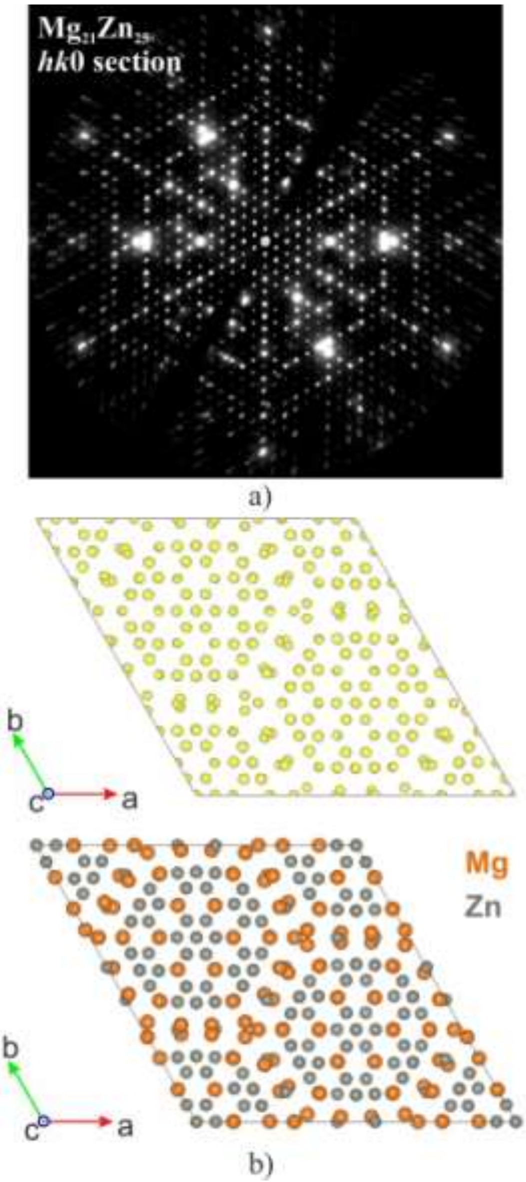

Fig. 24: Structure determination of A-microparticle of Mg12Zn alloy in initial state from PA-EDT data. a) *hk*0 section through the experimental 3D reciprocal map; b) results of the structure solution viewed along the [0001] direction (top - map of electrostatic potential; bottom - structural model).

TEM bright-field imaging revealed three additional features in the $Mg_{21}Zn_{25}$ A-microparticles: i) grain boundaries were observed in a number of $Mg_{21}Zn_{25}$ A-microparticles, which indicates the formation of an intermetallic polycrystalline phase during solidification, see Fig. 25a-1; ii) shadow-like regions, which surround the A-microparticles (Fig. 25a-2) and iii) the presence of nanoparticles, which are marked as D-nanoparticles and were embedded in the interiors of A-microparticles (Fig 25b, c). According to the HAADF-STEM imaging, which is actually dark-field imaging that is contrast sensitive to the Z atomic number of elements in a material, the D-nanoparticles (Fig. 25c, black arrows) consist of a greater amount of an element with lower atomic Z number than the surrounding $Mg_{21}Zn_{25}$ particle. The only intermetallic phase in the Mg-Zn binary phase diagram [27] that satisfies this condition is $Mg_{51}Zn_{20}$. It is supposed that the D-nanoparticles in $Mg_{21}Zn_{25}$ formed a eutectic compound of $Mg_{21}Zn_{25}$ + $Mg_{51}Zn_{20}$ during the solidification. The Z-contrast image again shows the shadow in the α-Mg matrix around the A-microparticle (Fig. 25c), which indicates an increased Zn concentration near the α-Mg matrix/A-microparticle interface.

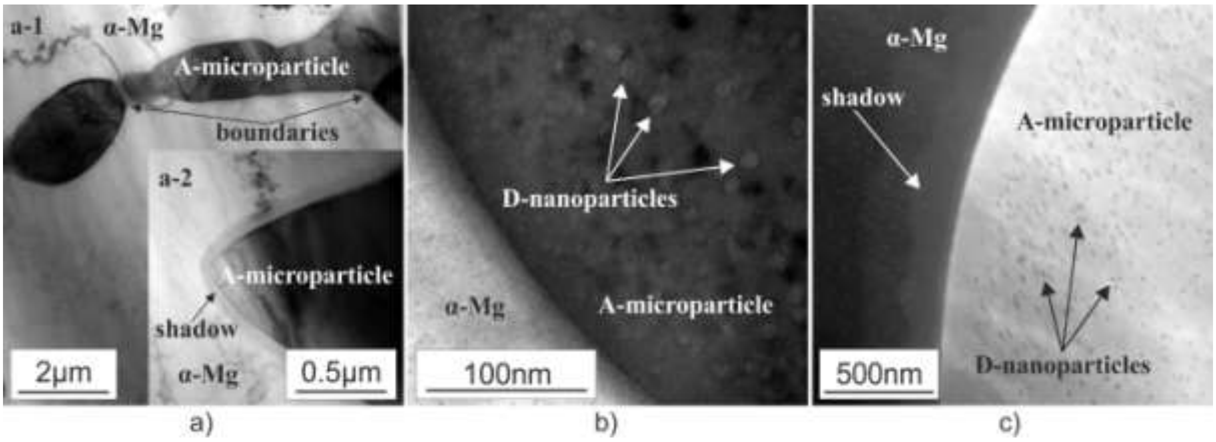

Fig. 25: Images of fine features connected with A-microparticles. a-1) TEM BF: boundaries within A-microparticle (marked by arrows); a-2) TEM BF: shadow in the vicinity of α-Mg matrix/A-microparticle interface; b) TEM BF: α-Mg matrix/A-microparticle interface and presence of D-nanoparticles (some of them marked by arrows) within A-microparticle; c) HAADF-STEM: α-Mg matrix/A-microparticle interface with increased Zn concentration (shadow) and D-nanoparticles within A-microparticle.

7.3.2 B-nanoparticles

As shown in Fig. 23c, B-nanoparticles with dimensions of approximately 100 nm were preferentially found near the $Mg_{21}Zn_{25}$ A-microparticles. Fig. 26 shows the morphology of B-nanoparticles at higher magnification. The crystal structure analysis using SAED and CBED fitted these particles to the orthorhombic crystal structure of $Mg_{51}Zn_{20}$ with the *Immm* space group and lattice parameters a = 1.408 nm, b = 1.449 nm, c = 1.403 nm, which were proposed by Higashi et al. [28]. The $Mg_{51}Zn_{20}$ B-nanoparticles in the α-Mg matrix are supposed to be the remainders of a solidification process after casting.

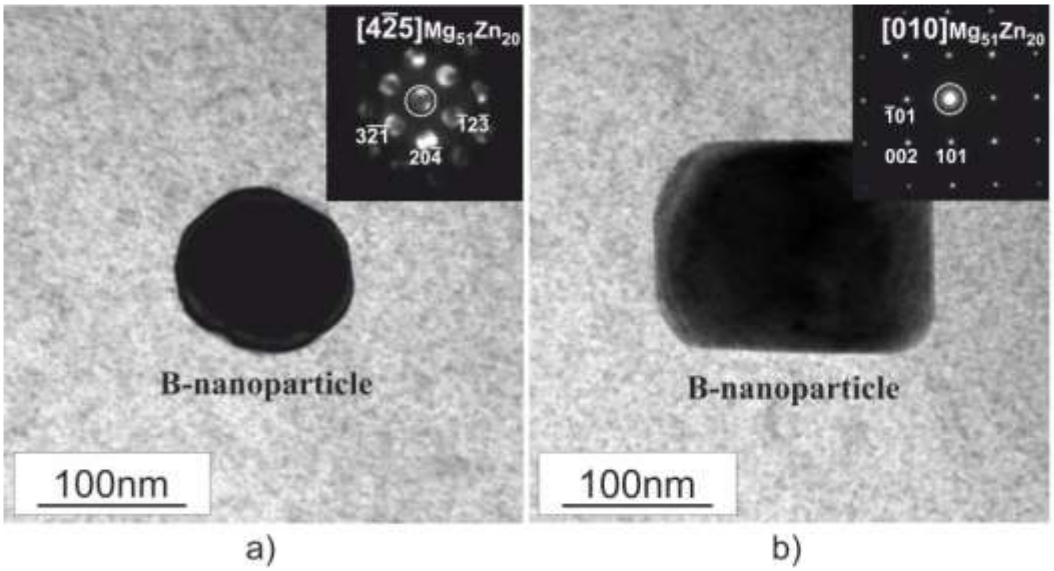

Fig. 26: TEM images of B-nanoparticles in the α-Mg matrix. a) BF image of a particle in a zone axis orientation and its corresponding CBED pattern indexed according to the $Mg_{51}Zn_{20}$ crystal structure in the [4$\bar{2}$5] zone axis; b) BF image of another particle and its corresponding SAED pattern indexed according to the $Mg_{51}Zn_{20}$ crystal structure in the [010] zone axis.

7.3.3 C-nanoparticles

The C-nanoparticles in Fig. 23c, which are approximately 5 nm in size, are densely and uniformly distributed in the entire α-Mg matrix with a clear shape similarity and preferential orientation relationship toward the α-Mg matrix. The particles were analysed using TEM BF, HRTEM with an in-situ heating experiment, precession-assisted EDT and SAED techniques.

7.3.3.1 In-situ Heating of Mg12Zn in Initial State

During the in-situ heating experiment in the temperature range of 150-250 °C, it was observed that the C-nanoparticles preserved their typical shapes and orientation while growing. The microstructure changes after 10 min at 150°C are shown in Fig. 27a. The FFT (Fast-Fourier transform) analysis of the HRTEM image (Fig. 27b) indicates that the C-nanoparticles possess the hexagonal crystal structure of the $MgZn_2$ phase with the $P6_3/mmc$ space group and lattice parameters a = 0.522 nm, c = 0.857 nm. This phase was proposed by Komura et al. [30].

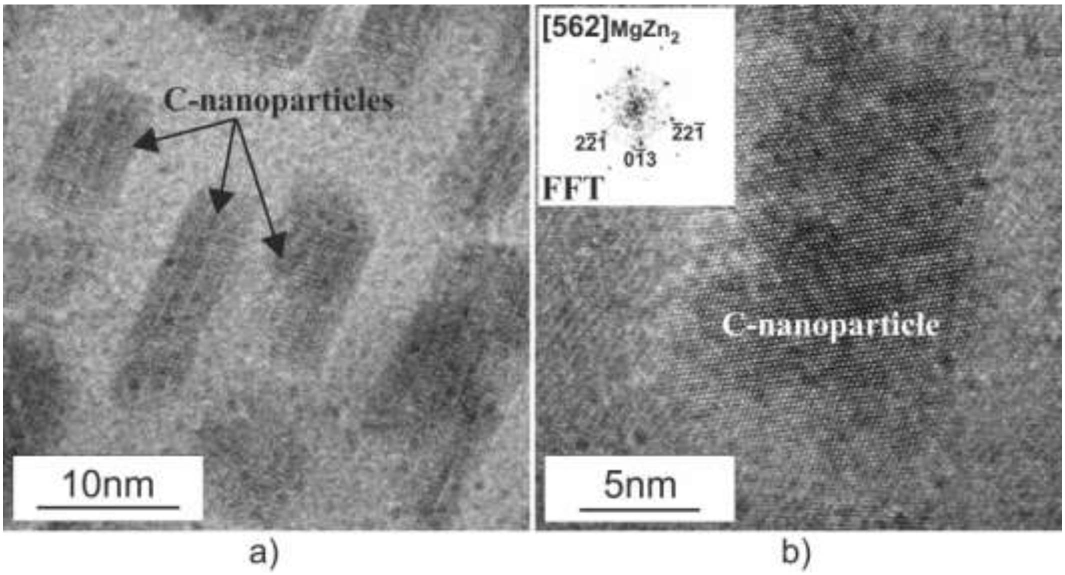

Fig. 27: HRTEM images of C-nanoparticles in the initial state Mg12Zn from the in-situ heating experiment. a) C-nanoparticles after 10 min at 150 °C; b) Detail of a C-nanoparticle with its corresponding FFT indexed according to the $MgZn_2$ crystal structure in the [562] zone axis.

7.3.3.2 PA-EDT Analysis

Because HRTEM is not the most appropriate technique for crystallographic analysis, a material that contained C-nanoparticles with dimensions suitable for PA-EDT experiments (see Fig. 28a) was prepared. The initial state of the Mg12Zn alloy was heat treated at 300 °C / 2 h to allow growth of C-nanoparticles and subsequently quenched into water. The crystal structure of the C-nanoparticles, which were determined using the PA-EDT (Fig. 28b), indeed corresponds to the $MgZn_2$ phase (space group $P6_3/mmc$ with lattice parameters $a \sim 0.53$ nm and $c \sim 0.87$ nm). It is worth noting that $MgZn_2$ particles had never been analysed using the PA-EDT technique and the resulting structure is notably consistent with the X-ray diffraction data [30]. Two different orientation relationships (ORs) of overgrown $MgZn_2$ C-nanoparticles toward the α-Mg matrix were found using the PA-EDT. The first OR is shown in Fig. 28c*:*

$$\text{OR1: } [0001]_{MgZn_2} \parallel [0001]_{\alpha};\ (11\bar{2}0)_{MgZn_2} \parallel (10\bar{1}0)_{\alpha}\ .$$

OR1 is consistent with an orientation relationship of a plate-like form of $MgZn_2$ precipitate termed β_2' in the literature [4, 15]. It is also considered a primary OR of β_2' precipitates toward the α-Mg matrix in Mg-Zn alloys [4, 15].

The second OR is shown in Fig. 28d:

$$\text{OR2: } [0001]_{\mathrm{MgZn_2}} \parallel [11\bar{2}0]_{\alpha};\ (11\bar{2}0)_{\mathrm{MgZn_2}} \parallel (0001)_{\alpha}\ .$$

OR2 is known for a lath-like form of the β_2' precipitate and considered a secondary OR of β_2' precipitates toward the α-Mg matrix in Mg-Zn alloys [4, 15].

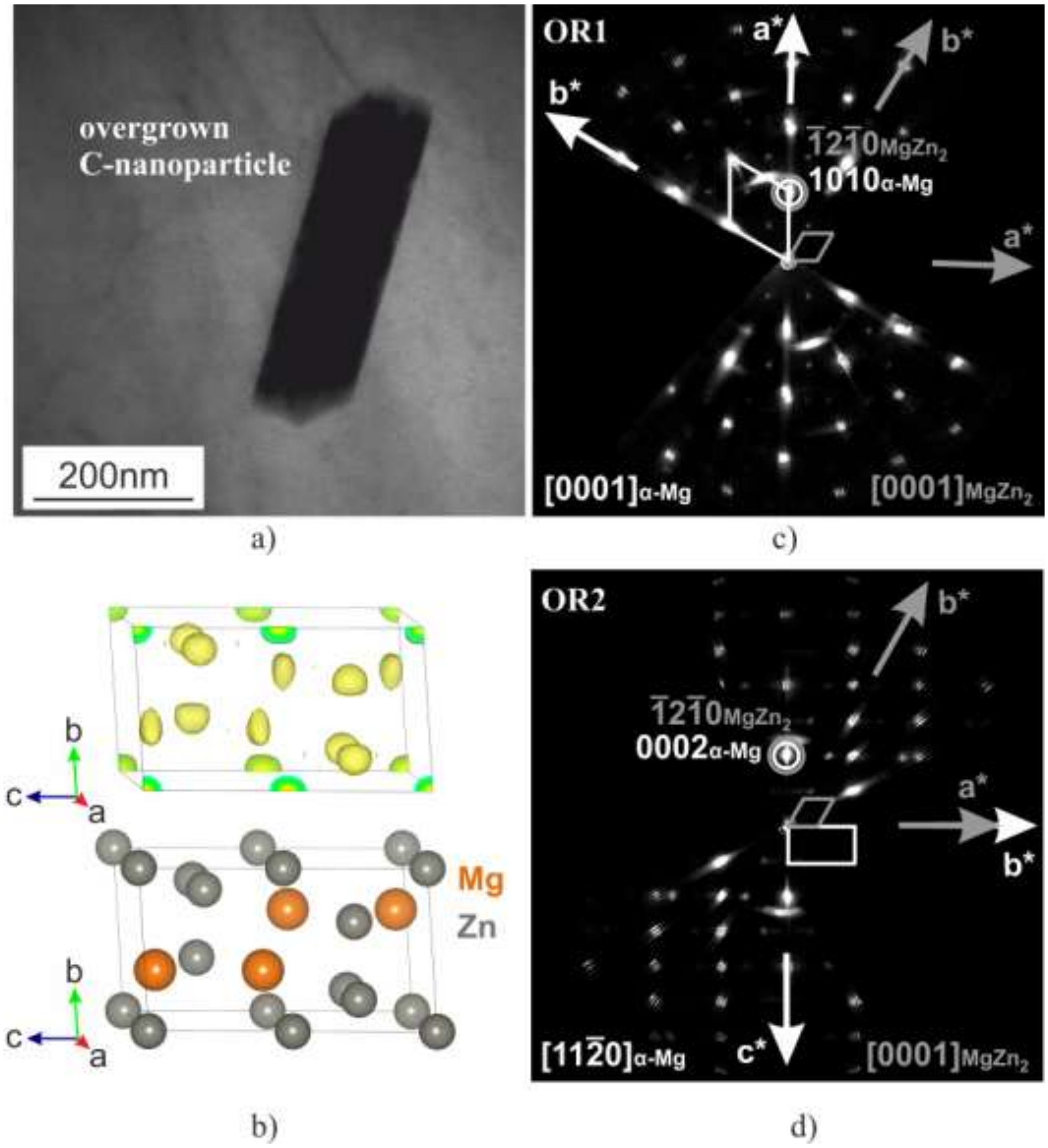

Fig. 28: Structure determination of C-nanoparticles and their orientation relationship toward α-Mg matrix obtained from EDT data in Mg12Zn alloy specially heat treated for this experiment: a) TEM BF image shows overgrown C-nanoparticles in the α-Mg matrix; b) results of structure solution (top - map of electrostatic potential, bottom - structural model); c) section through the experimental 3D reciprocal map, which shows the orientation relationship OR1; d) section through the experimental 3D reciprocal map, which shows the orientation relationship OR2.

7.3.3.3 TEM BF, HRTEM and SAED Analysis of Shapes and ORs

Possible shapes of β_2' $MgZn_2$ precipitates that form during aging are often discussed in connection to the ORs [4, 15, 18]. Therefore, it is important to discover the link between the shapes and the ORs of the $MgZn_2$ C-nanoparticles (approximately 5 nm in size) in the initial state of the material and to confirm the consistence with the results obtained by other authors for β_2' $MgZn_2$ precipitates (approximately 200 nm in size) in aged materials [4, 15, 18]. The shape and OR analyses were performed using TEM BF imaging with SAED (Fig. 29) and HRTEM imaging (Fig. 30).

TEM BF images (Figs. 29a-c) that were taken with the α-Mg matrix oriented to the $[0001]$, $[10\bar{1}0]$ and $[11\bar{2}0]$ zone axes reveal a uniform 3D shape of most C-nanoparticles. The shape is hexagonal-like (referred to as plate-like in the literature [4, 15]) in the $[0001]_\alpha$ projection (Fig. 29a) and rectangular-like in the $[10\bar{1}0]_\alpha$ (Fig. 29b) and $[11\bar{2}0]_\alpha$ (Fig. 29c) projections.

The corresponding SAED patterns (Fig. 29d-f) show that in addition to the α-Mg matrix reflections, there are other reflections from the C-nanoparticles with a clear preferential orientation relationship. There are streaks of different intensities in all SAED patterns in Fig. 29. The intense streaks (marked by grey ellipses) come from most C-nanoparticles, whereas the weaker ones (marked by grey rectangles) originate from the remaining C-nanoparticles. We consider only the reflections from the $\{0001\}_{MgZn_2}$, $\{10\bar{1}0\}_{MgZn_2}$ and $\{11\bar{2}0\}_{MgZn_2}$ plane systems in the discussion about the ORs because it is not possible to unambiguously identify $MgZn_2$ reflections with more complex indices from our experimental SAED patterns. The $[0001]_\alpha$ zone-axis SAED pattern (Fig. 29d) reveals six intense reflections from the $\{30\bar{3}0\}_{MgZn_2}$ planes (grey ellipse) that were rotated by 60°, which are parallel to the $< 11\bar{2}0 >_\alpha$ directions. Because the hexagonal symmetry gives six reflections of the $\{30\bar{3}0\}$ planes rotated by 60° only in the $[0001]$ zone-axis, the $[0001]_\alpha \parallel [0001]_{MgZn_2}$ orientation relationship holds in Fig. 29d. Hence, the OR1 found using the PA-EDT and reported for the β_2' precipitate [4, 15], $[0001]_{MgZn_2} \parallel [0001]_\alpha$; $(11\bar{2}0)_{MgZn_2} \parallel (10\bar{1}0)_\alpha$ is valid for the C-nanoparticles that create those intense reflections in Fig. 29d. Note: $(11\bar{2}0)_{MgZn_2} \parallel (10\bar{1}0)_\alpha$ is equivalent to $(10\bar{1}0)_{MgZn_2} \parallel (11\bar{2}0)_\alpha$ when both $MgZn_2$ and α-Mg matrix are in the [0001] zone axis.

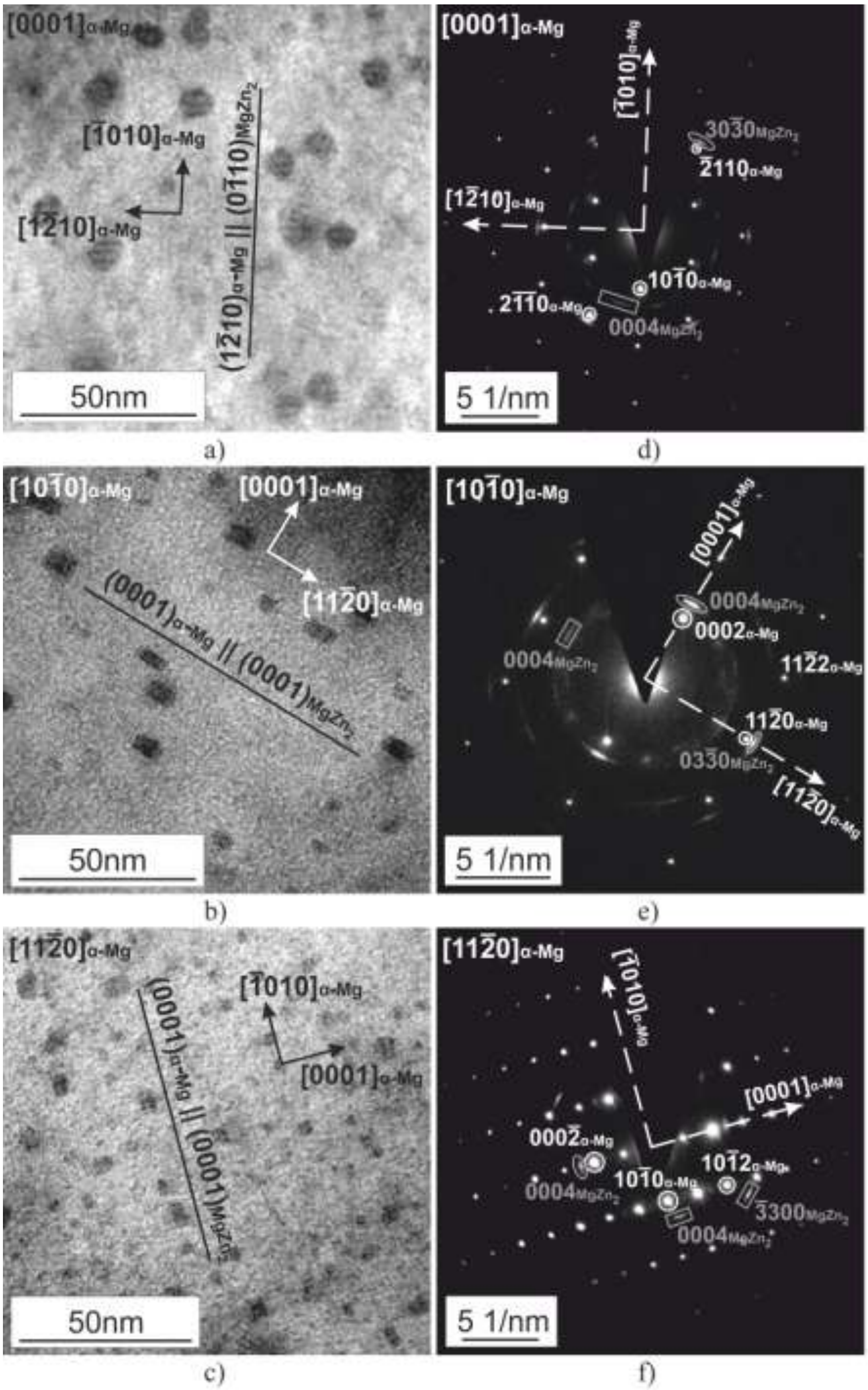

Fig. 29: OR and shape analysis of C-nanoparticles in Mg12Zn alloy in the initial state. C-nanoparticles are viewed in the BF TEM images a), b) and c) along the α-Mg matrix [0001], $[10\bar{1}0]$ and $[11\bar{2}0]$ directions, respectively, with their corresponding SAED patterns d), e) and f). The BF TEM images demonstrate the 3D shape of most C-nanoparticles, and the SAED patterns reveal the orientations of the C-nanoparticles in the α-Mg matrix.

The identical OR is also apparent from the $[10\bar{1}0]_{\alpha}$ zone-axis SAED pattern (Fig. 29e). The 0002_{α} reflections are parallel to the intense 0004_{MgZn_2} reflections (Fig. 29e, grey ellipse), and the $[11\bar{2}0]_\alpha$ direction is parallel to the $03\bar{3}0_{MgZn_2}$ reflections (Fig. 29e, grey ellipse), which are also intense. These two types of $MgZn_2$ reflections also belong to the OR1. The intense C-nanoparticle reflections in the $[11\bar{2}0]_\alpha$ zone-axis SAED pattern originated from the $(0004)_{MgZn_2}$ planes (Fig. 29f , grey ellipse), which are parallel to the reflections from the $(000\bar{2})_\alpha$ planes; thus, they support previous results. However, there is no visible reflection from the $\{11\bar{2}0\}_{MgZn_2}$ planes in Fig. 29f to resolve the complete OR1 from this pattern. All of these orientation relationships are listed in the Table 1.

Table 1

Main orientation relationships of the hexagonal $MgZn_2$ C-nanoparticles toward the α-Mg matrix, which result from the SAED patterns acquired in different α-Mg matrix zone axes.

α-Mg matrix direction	intense MgZn2 reflections	weaker MgZn2 reflections
[0001]α-Mg	[0001]MgZn2 ‖ [0001]α-Mg $(11\bar{2}0)$MgZn2 ‖ $(10\bar{1}0)$α-Mg	(0001)MgZn2 ‖ $(3\bar{4}10)$α-Mg *
$[10\bar{1}0]$α-Mg	[0001]MgZn2 ‖ [0001]α-Mg $(11\bar{2}0)$MgZn2 ‖ $(10\bar{1}0)$α-Mg	$(11\bar{2}0)$MgZn2 ‖ (0001)α-Mg
$[11\bar{2}0]$α-Mg	[0001]MgZn2 ‖ [0001]α-Mg	(0001)MgZn2 ‖ $(10\bar{1}0)$α-Mg * $(1\bar{1}00)$MgZn2 ‖ (1012)α-Mg *

*ORs with significant deviation

The analysis of the SAED patterns (Figs. 29d and 29f) confirms that most C-nanoparticles have OR1. The TEM BF images (Figs. 29a-c) show that they exhibit a rectangular (rod- or lath-like) shape in the $[10\bar{1}0]_\alpha$ and $[11\bar{2}0]_\alpha$ projections and a hexagonal (plate-like) shape in the $[0001]_\alpha$ projection, which is clearly seen in higher magnification in HRTEM image (Fig. 30a). The HRTEM images of the most common C-nanoparticles with OR1 demonstrate in fine detail the hexagonal (plate-like) shape projection in $[0001]_\alpha$ (Fig. 30a) and rectangular shape projection in $[10\bar{1}0]_\alpha$ (Fig. 30b). The analysis confirms the similarity in shape and primary OR of $MgZn_2$ C-nanoparticles with $MgZn_2$ $\beta_2^{'}$ precipitates [15].

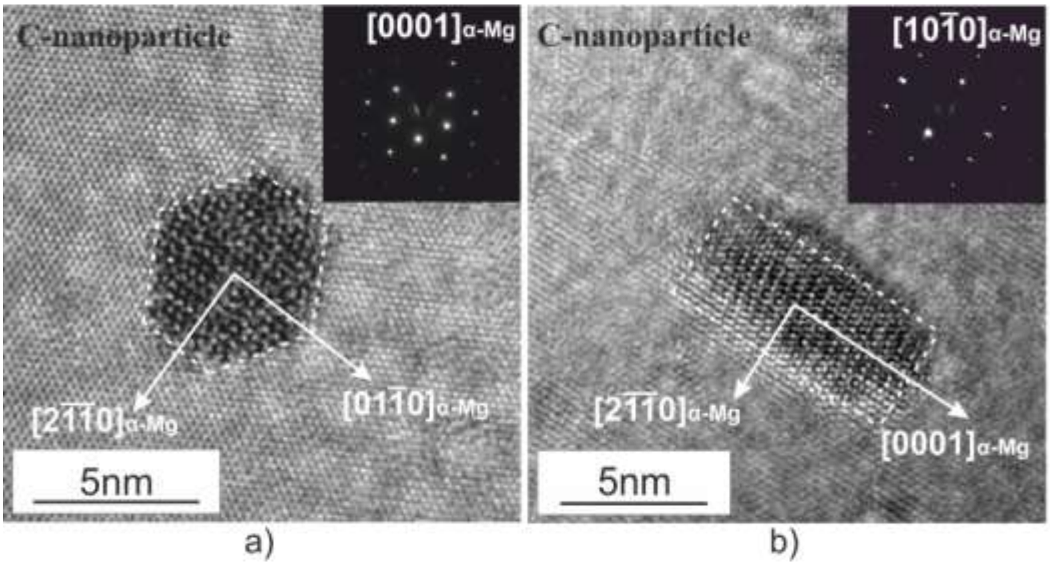

Fig. 30: HRTEM images demonstrate the shape projections of most C-nanoparticles onto the α-Mg matrix directions in the initial state Mg12Zn alloy: a) C-nanoparticle viewed along the $[0001]_{\alpha}$ zone axis with an evident hexagonal (plate-like) shape projection (SAED pattern in the inset); b) C-nanoparticle viewed along the $[10\bar{1}0]_{\alpha}$ zone axis with evident rectangular (rod- or lath-like) shape projection (SAED pattern in the inset).

There are also weaker $MgZn_2$ reflections in the presented SAED patterns (Figs. 29d-f), which do not belong to the OR1. In the $[0001]_{\alpha}$ zone-axis SAED pattern (Fig. 29d), there are 0004_{MgZn_2} reflections, which make a ring with twelve intensity maxima (one of which is marked by a grey rectangle) and twelve intensity minima. Because those minima are in the $< 11\bar{2}0 >_{\alpha}$ and $< 10\bar{1}0 >_{\alpha}$ directions, the C-nanoparticles that create 0004_{MgZn_2} reflections are oriented with their $\{0001\}_{MgZn_2}$ planes between $< 11\bar{2}0 >_{\alpha}$ and $< 10\bar{1}0 >_{\alpha}$, which gives $(0001)_{MgZn_2} \parallel (3\bar{4}10)_{\alpha}$ in average. However, the intensity deviation from the average is considerably large (up to ~10°). In the $[10\bar{1}0]_{\alpha}$ zone-axis SAED pattern (Fig. 29e), there are also weaker 0004_{MgZn_2} reflections (grey rectangle) parallel to the $[\bar{1}\bar{1}20]_{\alpha}$. They indicate a part of the OR2, $[0001]_{MgZn_2} \parallel [11\bar{2}0]_{\alpha}$; $(11\bar{2}0)_{MgZn_2} \parallel (0001)_{\alpha}$, which was also found by the PA-EDT discussed in the subsection 7.3.3.2 and reported for the β_2' precipitate in the literature [4, 15]. Nevertheless, there is no visible reflection from the $\{11\bar{2}0\}_{MgZn_2}$ planes in this pattern to confirm the complete OR2. In the $[11\bar{2}0]_{\alpha}$ zone-axis SAED pattern (Fig. 29f), one can see weaker $MgZn_2$ reflections from the $(0004)_{MgZn2}$ and $(\bar{3}300)_{MgZn_2}$ planes (grey rectangles). They are nearly parallel to the $10\bar{1}0_{\alpha}$ and $10\bar{1}2_{\alpha}$ reflections, respectively, with a biased intensity deviation of approximately 3°. These partial orientation relationships are also listed in Table 1. The shape analysis of C-nanoparticles with secondary ORs is not technically feasible.

7.3.4 D-nanoparticles

The presence of D-nanoparticles within A-microparticles and the formation of a eutectic compound $Mg_{21}Zn_{25}$ with $Mg_{51}Zn_{20}$ based on the Mg-Zn binary phase diagram [27] were discussed in the subsection 7.3.1.1. The HRTEM analysis was performed to support the HAADF-STEM data. The HRTEM image (Fig. 31a) shows a D-nanoparticle within an A-microparticle. Two reciprocal lattices fit well the FFT of the HRTEM image (Fig. 31a), which was processed using the CrysTBox software (Figs. 31b and 31c), green and blue crosses in Fig. 31b. There is an $Mg_{21}Zn_{25}$ reciprocal lattice [24] in the [101] orientation (blue crosses) and an $Mg_{51}Zn_{20}$ reciprocal lattice [28] in the $[\bar{1}1\bar{1}]$ orientation (green crosses). The FFT image shown in Fig. 31b was indexed according to the CrysTBox processing result (Fig. 31c) and confirms the formation of the eutectic compound $Mg_{21}Zn_{25}$ + $Mg_{51}Zn_{20}$. It is observed that the $[\bar{1}1\bar{1}]_{Mg_{51}Zn_{20}}$ zone axis is parallel to the $[101]_{Mg_{21}Zn_{25}}$ zone axis, and the $011_{Mg_{51}Zn_{20}}$ reflection is approximately 5° declined from the $1\overline{11}_{Mg_{21}Zn_{25}}$ reflection, but no ORs between $Mg_{21}Zn_{25}$ and $Mg_{51}Zn_{20}$ were deeply investigated in this work.

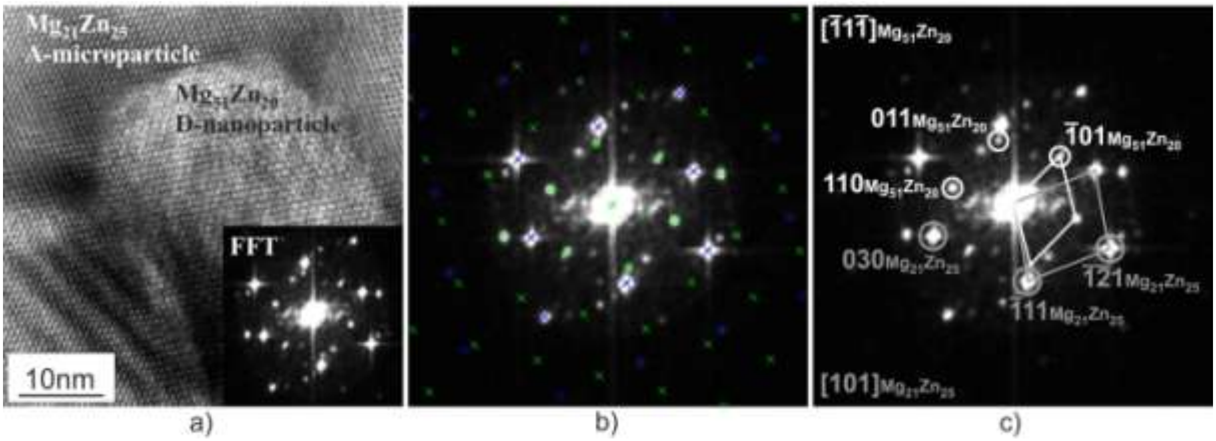

Fig. 31: Analysis of the $Mg_{21}Zn_{25}$ + $Mg_{51}Zn_{20}$ eutectic compound in the initial state Mg12Zn alloy: a) HRTEM image of a D-nanoparticle within an A-microparticle with an FFT of the overall image in the inset; b) FFT of the previous HRTEM image, which was processed using the CrysTBox software, reveals the presence of two distinct reciprocal lattices: $Mg_{21}Zn_{25}$ (blue crosses) and $Mg_{51}Zn_{20}$ (green crosses); c) indexed FFT of the HRTEM image shows an $Mg_{21}Zn_{25}$ A-microparticle in the [101] orientation and an $Mg_{51}Zn_{20}$ D-nanoparticle in the $[\bar{1}1\bar{1}]$ orientation.

7.4 Microstructure of Mg12Zn after ECAP-BP

Microstructure of Mg12Zn alloy in the initial state with all microstructure features was thoroughly discussed in subsection 7.3. The Mg12Zn alloy in initial state was subjected to ECAP-BP as described in the subsection 7.1. Resulting billet after ECAP-BP with dimensions of 10x10x50 mm was compact and crack-free on both - surface and cross sections in ID, ED and TD directions.

The typical microstructure overview of Mg12Zn after ECAP-BP from the micro-scale down to the nano-scale is shown in Fig. 32. An α-Mg matrix consists of two different types of areas. The first type represents a highly deformed structure that can be seen as the light areas in the LM micrograph (Fig. 32a) marked by yellow ellipses. The highly deformed structure means that no grains and grain boundaries were visualised by etching. The second type represents a partially recrystallized structure that can be seen as the dark areas in the LM micrograph (Fig. 32a) marked by red ellipses. The partially recrystallized structure means that recrystallized grains are already present in some parts of material; however, the recrystallization has not been finished. There are many particles (Fig. 32a, red arrows) that were labeled as A-microparticles and identified as the $Mg_{21}Zn_{25}$ intermetallic phase in the initial state, see the subsection 7.3.1. A-microparticles are distributed uniformly inside the α-Mg matrix, regardless of the α-Mg matrix area type (highly deformed or partially recrystallized structure).

It is obvious from the SEM micrograph (Fig. 32b) that some of the A-microparticles were broken up during ECAP-BP process. The TEM BF image (Fig. 32c) shows a boundary between the two different α-Mg matrix areas described as highly deformed and partially recrystalized (highlighted by a dotted line). The area on the left corresponds to the highly deformed structure, and the area on the right corresponds to the partially recrystallized structure. An average grain size in the partially recrystallized structure was estimated to be approximately 250 nm. The presence of small nanoparticles in both types of the α-Mg matrix areas is also apparent from Fig. 32c. These nanoparticles were previously marked as C-nanoparticles and determined to adopt the $MgZn_2$ crystal structure, see the subsection 7.3.3 [30].

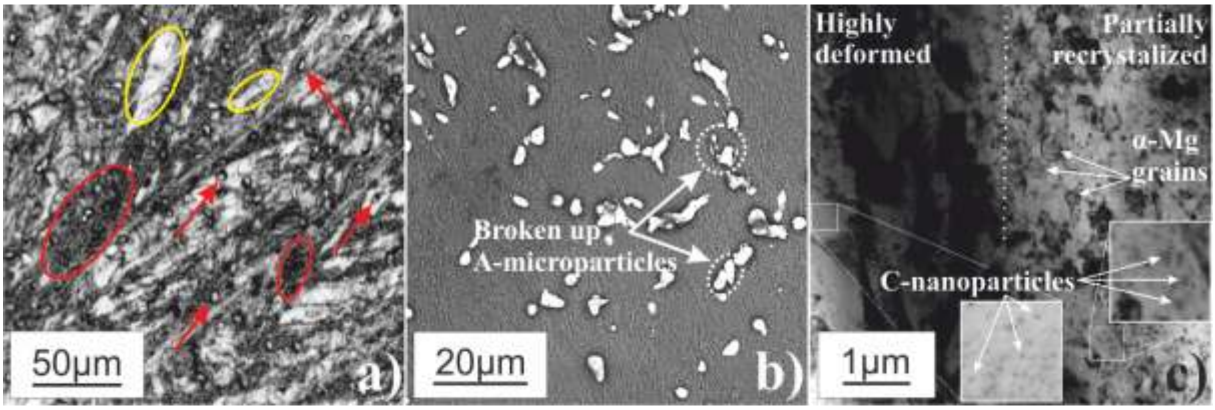

Fig. 32. General microstructure overview of the Mg12Zn alloy after ECAP-BP. a) an LM image shows A-microparticles (red arrows) uniformly distributed in both types of an α-Mg matrix: highly deformed (light areas, yellow ellipses) and partially recrystallized (dark areas, red ellipses); b) an SEM image shows the broken up A-microparticles; and c) a TEM BF image shows the boundary between a highly deformed (on the left) and a partially recrystallized (on the right) α-Mg matrix with a distribution of C-nanoparticles in both areas.

7.5 Particles in Mg12Zn after ECAP-BP

The ECAP-BP process influenced also each type of intermetallic particle, which were found and investigated in the initial state of the Mg12Zn alloy (see the subsection 7.3). Changes are analyzed and described in separated sections with references to the initial state. The microstructure of the as-processed material was analyzed in three perpendicular planes of the billet, ID-ED, ID-TD and ED-TD planes (see Fig. 22). No differences in the particles were observed in these three planes, therefore there is no reference to particular plane in the text below.

7.5.1 Influence of ECAP-BP on A-microparticles

A-microparticles were thoroughly examined in the initial state (see the subsection 7.3.1) and their crystal structure unambiguously identified as $Mg_{21}Zn_{25}$ [24]. After ECAP-BP, three basic forms (or combinations thereof) of the A-microparticles occur in the microstructure (Fig. 33). These basic forms were characterized as: i) single-crystalline, ii) nano-crystalline and iii) broken up. These individual forms and their combinations are described in separated subsections. A connection between the A-microparticle form after ECAP-BP and the corresponding type of surrounding α-Mg matrix (highly deformed or partially recrystallized) is also discussed.

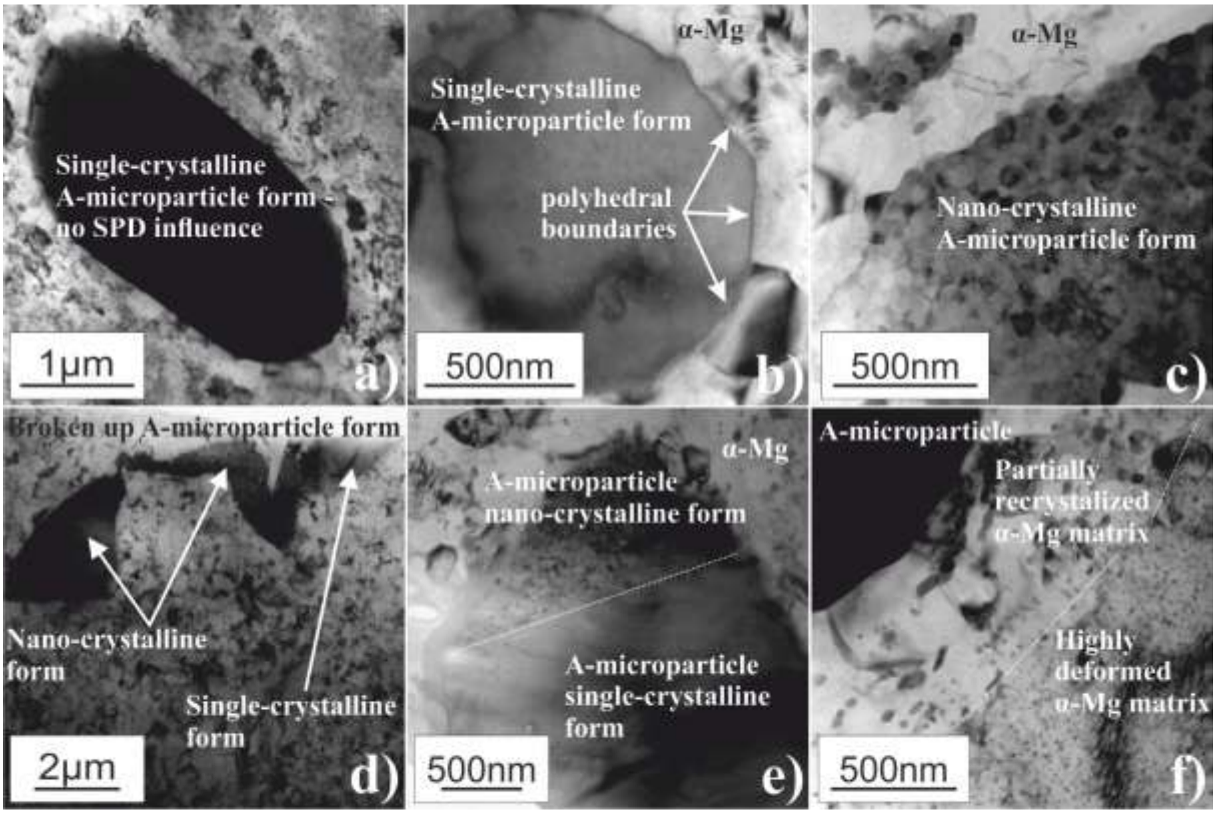

Fig. 33. A-microparticles in Mg12Zn after ECAP-BP. TEM BF images show: a) a single-crystalline A-microparticle form with a negligible influence of ECAP-BP; b) a single-crystalline A-microparticle form sharing polyhedral boundaries with the α-Mg matrix; c) a detail of a nano-crystalline A-microparticle form; d) a broken up A-microparticle form that is to a major extent combined with a nano-crystalline form and to a minor extent with a single-crystalline form; e) an A-microparticle with a boundary between a nano-crystalline form and a single-crystalline form; and f) that A-microparticles in a highly deformed α-Mg matrix are preferential sites for α-Mg matrix recrystallization.

7.5.1.1 Single-crystalline

A-microparticles that exhibit negligible (Fig. 33a) or minor (Fig. 33b) changes during ECAP-BP were characterized as a single-crystalline form. Fig. 33b shows a typical image of an A-microparticle with a polyhedral boundary instead of a rounded one. It looks like a spatial adaptation of the particle boundaries in relation to the partially recrystallized α-Mg matrix polyhedral grains. The A-microparticles with polyhedral boundaries were observed more frequently in the microstructure than the A-microparticles with a negligible impact of SPD. It is worth reminding that some of the A-microparticles in the initial state possessed internal boundaries. The term single-crystalline form is also used for particular regions of the A-microparticles separated by internal boundaries that exhibited minor changes during ECAP-BP (these features are described below in the subsection 7.5.1.4.

7.5.1.2 Nano-crystalline

Plastic deformation inside the A-microparticles during ECAP-BP gave origin to nano-crystalline regions with an average grain size well below 100 nm, as seen in the TEM BF image (Fig. 33c). An inspection of several samples showed that the nano-crystalline form was more frequent in the microstructure than the single-crystalline one.

7.5.1.3 Broken up

The SPD process forced some of the A-microparticles to become broken up. The A-microparticles of this form were already shown in an SEM micrograph (Fig. 32b). A detail of a broken up A-microparticle is shown in a TEM BF image (Fig. 33d). It is clearly seen that the surroundings of broken up particles are completely filled with the α-Mg matrix, and no cracks were observed after ECAP-BP. It is also apparent that the particle in Fig. 33d consists of a combination of the two basic forms characterized above (single-crystalline and nano-crystalline). This feature is described below.

7.5.1.4 Combinations of Basic Forms

Combinations of the three described basic forms of A-microparticles were also observed. An example of a particle combining a single-crystalline form and a nano-crystalline form is shown in a TEM BF image (Fig. 33e, the boundary between the two forms is highlighted by a dotted line). Fig. 33d shows a particle combining all of the described forms. It is a broken up particle with a large area of the nano-crystalline form and a small area of the single-crystalline form. These two areas were probably separated by an internal boundary in the A-microparticle in the initial state.

The origin of such an unequal plastic deformation of the A-microparticles may stem from their polycrystalline nature in the initial state. Some crystallites with various orientations might be favorably aligned to a shear stress during ECAP-BP that results in a mixed form of the A-microparticle. It is important to note that a broken up form cannot exist individually and is always combined with a nano-crystalline or a single-crystalline form.

7.5.1.5 Connection between A-microparticle Form and α-Mg Matrix Type after ECAP-BP

It was found that each A-microparticle form and each combination occur in both α-Mg matrix types (highly deformed and partially recrystallized structures), hence, the A-microparticles were deformed independent of the α-Mg matrix. However, a detailed investigation discovered that A-microparticles located in the highly deformed α-Mg matrix areas exhibited an additional feature at the α-Mg/A-microparticle interface. The α-Mg matrix is partially recrystallized in close vicinity to the A-microparticles (Fig. 33f), which indicates that the A-microparticles are preferential sites for an α-Mg grain nucleation.

7.5.2 Influence of ECAP-BP on B-nanoparticles

B-nanoparticles with size of approximately 100 nm in the initial state of an Mg12Zn alloy occurred preferentially in the close vicinity to the A-microparticles and were identified as the $Mg_{51}Zn_{20}$ phase [28]. A careful search for a B-nanoparticle in the microstructure after ECAP-BP was performed, however, no evidence of their existence was found. According to the Mg-Zn binary phase diagram proposed by Okamoto [27], they could transform into α-Mg or $Mg_{21}Zn_{25}$ during SPD.

7.5.3 Influence of ECAP-BP on C-nanoparticles

C-nanoparticles were densely and uniformly distributed within the α-Mg matrix of the Mg12Zn alloy in the initial state and determined to be the $MgZn_2$ phase (see the subsection 7.3.3). It was shown in Fig. 32c that they are still present in the microstructure after ECAP-BP within both types of the α-Mg matrix (highly deformed and partially recrystallized structures). Because these particles exhibited distinct behavior in both α-Mg matrix types, they are described in separate subsections.

7.5.3.1 C-nanoparticles in Highly Deformed α-Mg Matrix

An overview of the C-nanoparticles in a highly deformed α-Mg matrix in Mg12Zn alloy after ECAP-BP is seen in a TEM BF image (Fig. 34a). There are large (up to 100 nm) and small (approximately 10 nm) C-nanoparticles in the highly deformed microstructure.

The large C-nanoparticles were examined using SAED to confirm the crystal structure after ECAP-BP. An example of the large C-nanoparticle is shown in a TEM BF image (Fig. 34b) with its zone axis SAED pattern in the inset, which is magnified in Fig. 34c. The diffraction pattern was well fitted and indexed according to the MgZn$_2$ crystal structure [30] in the $[1\bar{2}10]$ zone axis orientation. Fig. 34c also shows the presence of the α-Mg matrix reflections with no zone axis orientation, which indicates that the large C-nanoparticles do not possess an orientation relationship toward the highly deformed α-Mg matrix. The same finding was confirmed for several large C-nanoparticles.

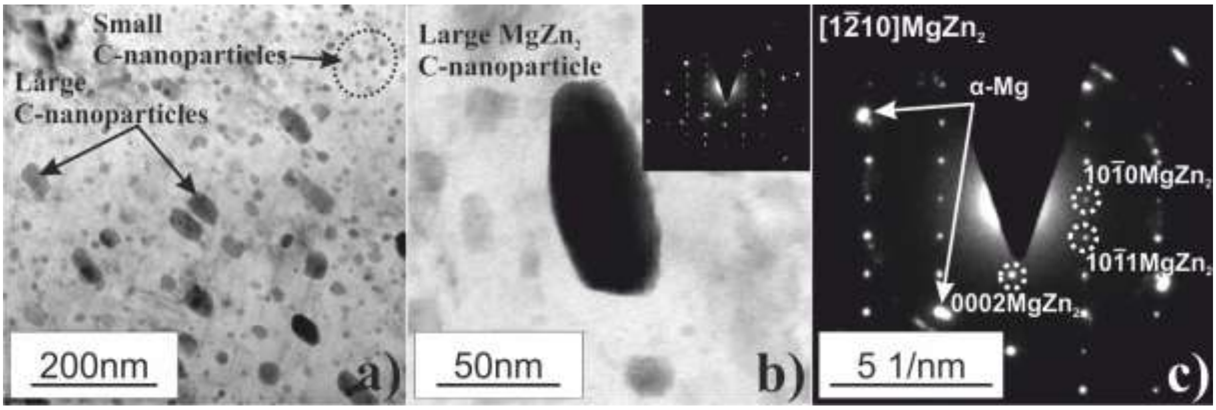

Fig. 34. MgZn$_2$ C-nanoparticles in a highly deformed α-Mg matrix of Mg12Zn alloy after ECAP-BP. a) a TEM BF image reveals C-nanoparticles in a highly deformed α-Mg matrix after ECAP-BP – some of them grew to 100 nm (large), whereas the others were approximately 10 nm (small); b) a TEM BF image shows a large C-nanoparticle in a zone axis orientation with its SAED pattern in the inset; and c) a magnified SAED pattern from the particle in b) indexed according to MgZn$_2$ in the $[1\bar{2}10]$ zone axis.

Small C-nanoparticles within the highly deformed α-Mg matrix were examined using bright-field imaging and SAED with the α-Mg matrix oriented to a low-index zone axis. A typical view of the C-nanoparticles in the α-Mg matrix oriented to the $[1\bar{1}00]$ zone axis is shown in a TEM BF image (Fig. 35a) with the corresponding SAED pattern in Fig. 35b. Reflections coming from the α-Mg matrix are diffuse because of a texture in the highly deformed regions caused by SPD. In addition to the α-Mg matrix reflections, there are intense reflections from the C-nanoparticles matching the $MgZn_2$ structure. Appropriate pairs of the $MgZn_2$ and the α-Mg reflections in the pattern are arranged to form an OR, which is marked as OR1 in the initial state:

$$[0001]MgZn_2 \,||\, [0001]\alpha - Mg;\ (01\bar{1}0)MgZn_2 \,||\, (11\bar{2}0)\alpha - Mg$$

and is also satisfied after ECAP-BP. In general, OR1 is considered to be the most common OR for $MgZn_2$ nanoparticles in Mg-Zn alloys [4].

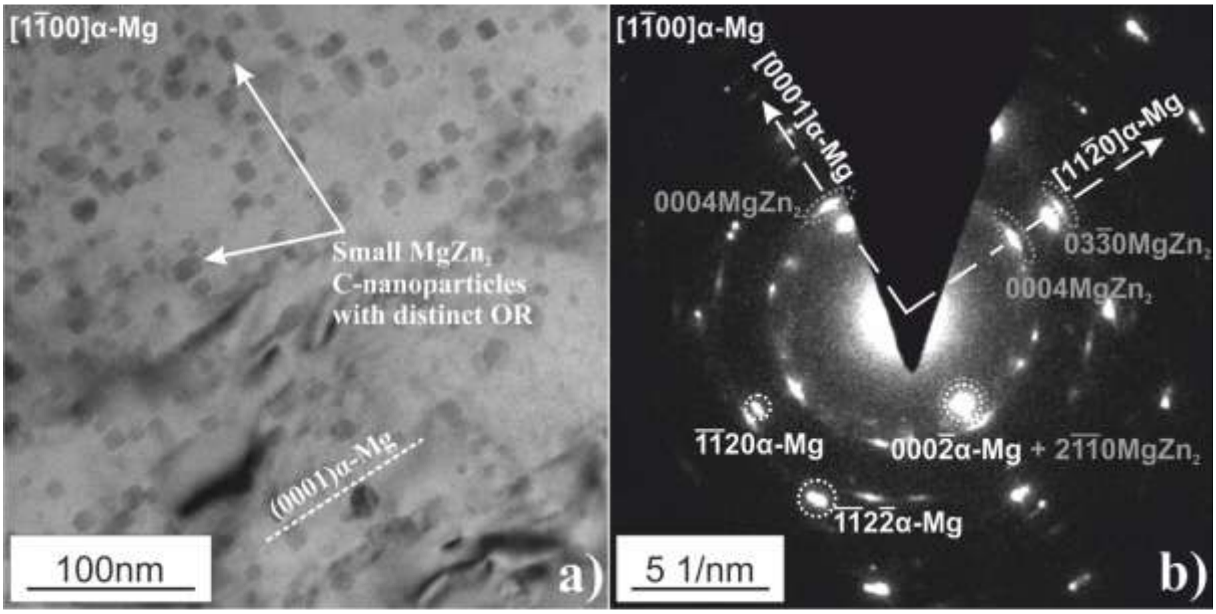

Fig. 35. Small $MgZn_2$ C-nanoparticles in a highly deformed α-Mg matrix of Mg12Zn alloy after ECAP-BP. a) a TEM BF image of small $MgZn_2$ C-nanoparticles in a highly deformed α-Mg matrix oriented to the $[1\bar{1}00]$ zone axis shows that the C-nanoparticles adapt two different preferential orientations; b) a SAED pattern corresponding to a) confirms that small $MgZn_2$ C-nanoparticles possess OR1 and OR2.

It was revealed that some of the small C-nanoparticles are oriented perpendicular to the others (see Fig. 35a, marked by arrows). This phenomenon is reflected in the SAED pattern (Fig. 35b), where $0004MgZn_2$ reflections are also intense in the $[11\bar{2}0]\alpha - Mg$ direction. This is a part of OR2:

$$[0001]MgZn_2 \,||\, [11\bar{2}0]\alpha - Mg;\ (11\bar{2}0)MgZn_2 \,||\, (0001)\alpha - Mg,$$

and it is described as a minor one in the initial state in the subsection 7.3.3.3. The $0004 MgZn_2$ reflections in the $[11\bar{2}0]\alpha-Mg$ direction in the initial state were weak and became intense after ECAP-BP (compare with Fig. 35b and Fig. 29e). The combination of the BF image (Fig. 35a) and the SAED pattern (Fig. 35b) indicate that OR2 is more frequent after ECAP-BP then in the initial state. The $2\bar{1}\bar{1}0 MgZn_2$ reflections that belong to the second part of OR2 are overlapping in the diffraction pattern with the appropriate $000\bar{2}\alpha-Mg$ reflections because of a negligible difference in the corresponding d-spacing of both phases. OR2 is also known as a common OR for $MgZn_2$ nanoparticles in Mg-Zn alloys [4].

The two most common orientation relationships of $MgZn_2$ nanoparticles toward the α-Mg matrix in Mg-Zn alloys are depicted in Fig. 36 using two model lattices with a hexagonal symmetry.

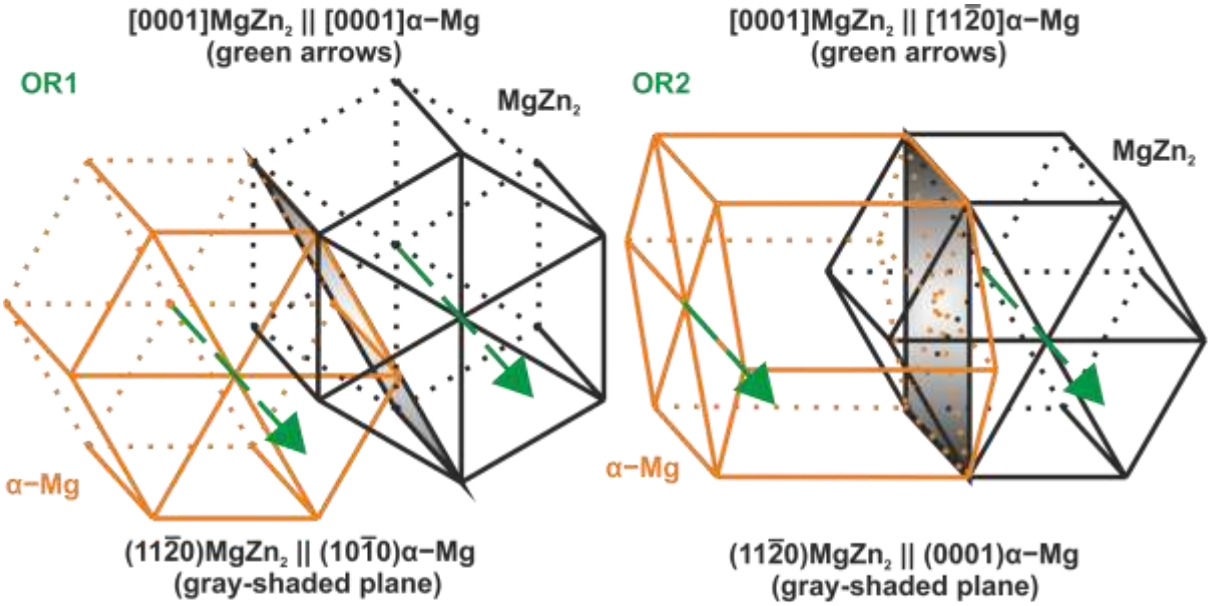

Fig. 36. Visualization of the two most common orientation relationships of $MgZn_2$ nanoparticles (C-nanoparticles in this work) with the α-Mg matrix in Mg-Zn alloys. Both α-Mg matrix and $MgZn_2$ particles possess a hexagonal symmetry. The hexagonal lattices are oriented with respect to each other to satisfy OR1 (on the left) and OR2 (on the right). Note: the parameters of the model lattices are not to scale.

Differences in the morphology and size of C-nanoparticles in a highly deformed α-Mg matrix likely stem from their origin in the initial state. Some of them could have grown and possibly lost coherency with the α-Mg matrix during SPD carried out at an elevated temperature, while the others were newly formed from a supersaturated solid solution of Zn in the α-Mg matrix.

7.5.3.2 C-nanoparticles in Partially Recrystallized α-Mg Matrix

Fig. 37a shows a typical view of the C-nanoparticles present in areas with the partially recrystallized structure of the α-Mg matrix in Mg12Zn alloy after ECAP-BP with an average grain size of approximately 250 nm. The C-nanoparticles possess different sizes (from ~10 nm up to ~100 nm) and occur homogeneously both in the grain interior and at the grain boundary with no preference to either one. An example of a C-nanoparticle in the partially recrystallized area of the α-Mg matrix is shown in a TEM BF image (Fig. 37b) with its corresponding SAED pattern (inset in Fig. 37b, magnified in Fig. 37c). Reflections in the SAED pattern were well fitted and indexed according to the $MgZn_2$ crystal structure [30] in the $[1\bar{2}10]$ zone axis orientation (Fig. 37c). Moreover, Fig. 37c shows that the α-Mg grain is not in a zone axis orientation, which indicates that the particle possesses no OR toward the partially recrystallized α-Mg grain. To conclude these, several particles were analyzed and the corresponding results obtained.

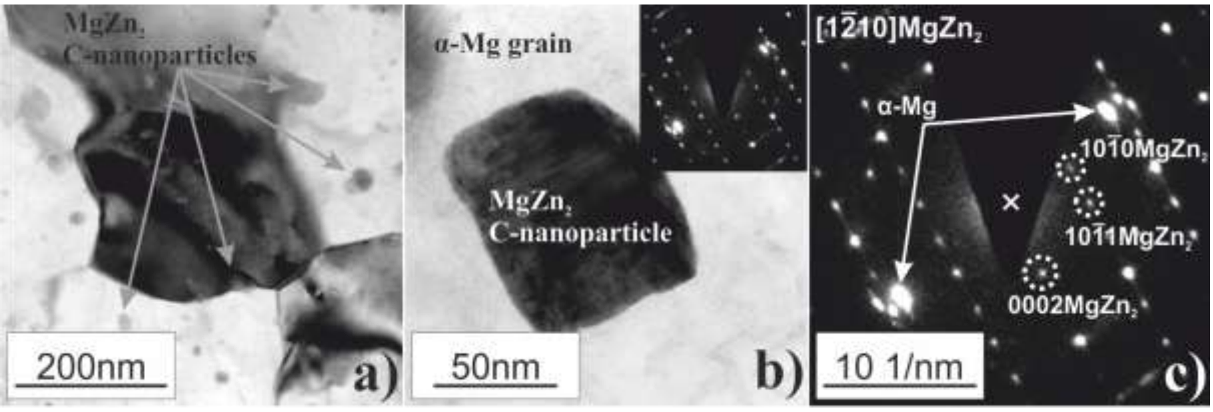

Fig. 37. $MgZn_2$ C-nanoparticles in a partially recrystallized α-Mg matrix of Mg12Zn alloy after ECAP-BP. a) a TEM BF image presents the distribution and size of C-nanoparticles in a partially recrystallized α-Mg matrix; b) a TEM BF image shows a C-nanoparticle in a zone axis orientation with its SAED pattern in the inset; and c) Corresponding SAED pattern from the particle in b) indexed according to $MgZn_2$ in the $[1\bar{2}10]$ orientation.

It can be concluded that C-nanoparticles during ECAP-BP adopted different changes in a highly deformed and partially recrystallized α-Mg matrix. In the highly deformed α-Mg matrix, C-nanoparticles remained either very small (< 10 nm) or grew to be large (up to ~100 nm). However, the areas with the large C-nanoparticles (Fig. 34a) were rather rare. Fig. 35a is characteristic view of the C-nanoparticles in the highly deformed α-Mg matrix. These small

(10 nm) C-nanoparticles possess OR1 and OR2 toward the α-Mg matrix. C-nanoparticles in a partially recrystallized α-Mg matrix (Fig. 37a) were also found with sizes from ~10 nm up to ~100 nm. Contrary to the C-nanoparticles in a highly deformed α-Mg matrix, the average size of C-nanoparticles in the partially recrystallized α-Mg matrix is much higher (> 50 nm on average). No OR for the C-nanoparticles that reached sizes of ~100 nm in either the highly deformed or the partially recrystallized α-Mg matrix was revealed using the SAED technique.

7.5.4 Influence of ECAP-BP on D-nanoparticles

In the initial state of the Mg12Zn alloy were D-nanoparticles with a size of 10-50 nm located inside $Mg_{21}Zn_{25}$ A-microparticles and identified as the $Mg_{51}Zn_{20}$ phase forming a eutectic compound, $Mg_{21}Zn_{25}$ + $Mg_{51}Zn_{20}$ (see the subsection 7.3.4). As was shown in the subsection 7.5.1, there are three basic forms of A-microparticles after ECAP-BP. A broken up form cannot exist individually and is always combined with a nano-crystalline or a single-crystalline form. The behavior of the D-nanoparticles was therefore investigated in single-crystalline and nano-crystalline forms (refer to the Fig. 33) and described in two separate subsections.

7.5.4.1 D-nanoparticles in Single-crystalline A-microparticle Form

D-nanoparticles inside a single-crystalline A-microparticle form are shown in a TEM BF image (Fig. 38a). There is a clear dispersion in the D-nanoparticle size (ranging from 10 nm to 50 nm). A conservation of the $Mg_{51}Zn_{20}$ crystal structure of the D-nanoparticles in the single-crystalline form of the A-microparticles was confirmed using HRTEM imaging (Fig. 38b) and its Fourier transform analysis (Fig. 38c). There are two overlapping reciprocal lattices in the Fourier transformed image (Fig. 38c). One of them was identified as a trigonal $Mg_{21}Zn_{25}$ reciprocal lattice in the $[0\bar{1}3]$ orientation, and the second one was an orthorhombic $Mg_{51}Zn_{20}$ in the $[0\bar{1}1]$ orientation. The $\bar{3}00 Mg_{21}Zn_{25}$ reflections are parallel to the $200 Mg_{51}Zn_{20}$ reflections, which allow one to figure out a possible OR as follows:

$$[0\bar{1}3]Mg_{21}Zn_{25} \; || \; [0\bar{1}1]Mg_{51}Zn_{20};\ (100)Mg_{21}Zn_{25} \; || \; (100)Mg_{51}Zn_{20}.$$

However, further investigation and employment of more reliable electron diffraction techniques for the OR determination would be needed to prove this finding.

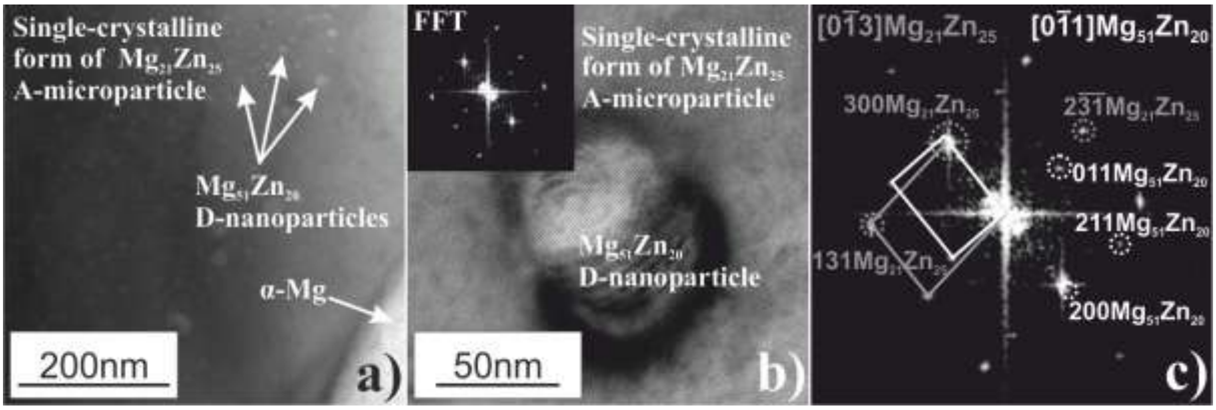

Fig. 38. $Mg_{51}Zn_{20}$ D-nanoparticles inside a single-crystalline A-microparticle form in Mg12Zn alloy after ECAP-BP. a) a TEM BF image shows D-nanoparticles with different sizes inside a single-crystalline A-microparticle; b) an HRTEM image shows the detail of a D-nanoparticle in a single-crystalline A-microparticle, and its FFT is in the inset; and c) the magnified FFT from b) shows two reciprocal lattices indexed according to $Mg_{51}Zn_{20}$ in the $[0\bar{1}1]$ orientation and $Mg_{21}Zn_{25}$ in the $[0\bar{1}3]$ orientation.

7.5.4.1 D-nanoparticles in Nano-crystalline A-microparticle Form

A representative image of an A-microparticle in Mg12Zn alloy after ECAP-BP with a boundary (white line) between the nano-crystalline and single-crystalline forms is shown in a TEM BF image (Fig. 39a). There are some brighter features in the nano-crystalline region. However, it is not straightforward to assign them as D-nanoparticles because of diffraction contrast phenomena. The brightness could originate just from the different crystal orientations of the nano-sized grains formed in the nano-crystalline area of the A-microparticle (a grain oriented in a strong Bragg condition appears dark, and one far from the Bragg condition appears light). Z-contrast HAADF-STEM imaging (Fig. 39b) is much more indicative. An HAADF detector is very sensitive to differences in the atomic Z-number of elements present within a specimen, and it is not so sensitive to the diffraction contrast. Thus, features containing a higher amount of a lighter element appear dark, and features containing a higher amount of a heavier element appear bright in an HAADF image, regardless of their orientation.

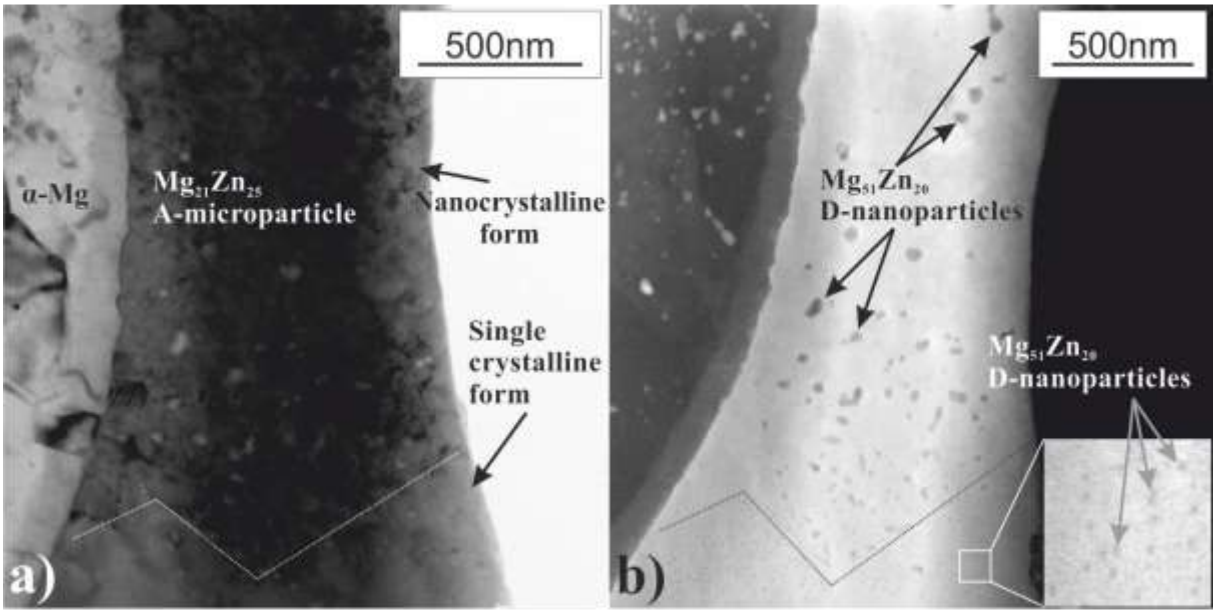

Fig. 39. $Mg_{51}Zn_{20}$ D-nanoparticles in a nano-crystalline A-microparticle form in Mg12Zn alloy after ECAP-BP. a) a TEM BF image shows a boundary (dotted line) between single-crystalline and nano-crystalline forms of an A-microparticle with large bright features; b) a HAADF-STEM image of the same region confirms the presence of large $Mg_{51}Zn_{20}$ D-nanoparticles in the nano-crystalline A-microparticle form that correspond to the bright features from a).

It is clearly seen that the bright features inside the A-microparticle nano-crystalline form in the TEM BF image (Fig. 39a) match well with the dark features in the corresponding areas of the HAADF-STEM image (Fig. 39b). Because the features are darker than the parent A-microparticle in the HAADF image, they have to contain a higher amount of a lighter element. In the case of the parent $Mg_{21}Zn_{25}$ A-microparticle, the only Mg-Zn intermetallic compound satisfying this condition according to the Mg-Zn binary phase diagram [27] is the $Mg_{51}Zn_{20}$ phase. Hence, the HAADF-STEM technique confirmed the presence of the D-nanoparticles in the nano-crystalline A-microparticle regions and the preservation of their phase structure. It is also seen from Fig. 39b that the average size of D-nanoparticles is gradually increasing from 10 nm in the single-crystalline form up to 100 nm in the nano-crystalline form of the A-microparticle.

7.6 Zn Distribution in α-Mg Matrix of Mg12Zn

The α-Mg matrix of the Mg12Zn alloy after ECAP-BP consists of two different types of microstructural areas: highly deformed and partially recrystallized. It was shown that $MgZn_2$ nanoparticles get larger in the partially recrystallized areas of the α-Mg matrix after ECAP-BP. During this process, a majority of the zinc from the supersaturated solid solution of α-Mg matrix is consumed mainly by the $MgZn_2$ nanoparticles and results in the inhomogeneous distribution of Zn in the α-Mg matrix. Consequently, either Zn depleted or Zn saturated zones can occur after ECAP-BP. Zn saturated zones are therefore located close to the $MgZn_2$ nanoparticles after ECAP-BP. This phenomenon can also be seen in the work by Basha et al. [50] (Fig. 10b in the reference article), yet the authors did not pay any closer attention to this phenomenon.

Gradual changes of Zn concentration in the microscale can have significant impact on material properties, particularly corrosion resistance. Therefore, in this section, Mg12Zn alloy in initial state and Mg12Zn alloy after ECAP-BP were investigated using HAADF-STEM combined with EELS to obtain an overview of Zn inhomogeneity in the α-Mg matrix.

7.6.1 HAADF-STEM Imaging

HAADF-STEM image contrast strongly depends on atomic number, Z, (the higher the Z-number the higher the brightness) thus giving a qualitative information about chemical gradients. HAADF-STEM images of Mg12Zn alloy in Fig. 40a-c show a general overview of the $MgZn_2$ nanoparticles in the initial state of α-Mg matrix. Details of the microstructure (Fig. 40d-f) acquired at higher magnification show chemical composition differences represented by a grayscale contrast of the α-Mg matrix. The Zn concentration in at.% inscribed in the images were measured using an EELS technique and will be described in the next subsection. While there is no obvious contrast in the α-Mg matrix of Mg12Zn alloy in the initial state (Fig. 40a and 40d), the highly deformed and partially recrystallized α-Mg matrix after ECAP-BP (Fig. 40e and 40f) exhibits perceptible contrast resulting in darker and brighter areas. The brighter areas in the partially recrystallized α-Mg matrix are visible especially around the $MgZn_2$ nanoparticles (Fig. 40f).

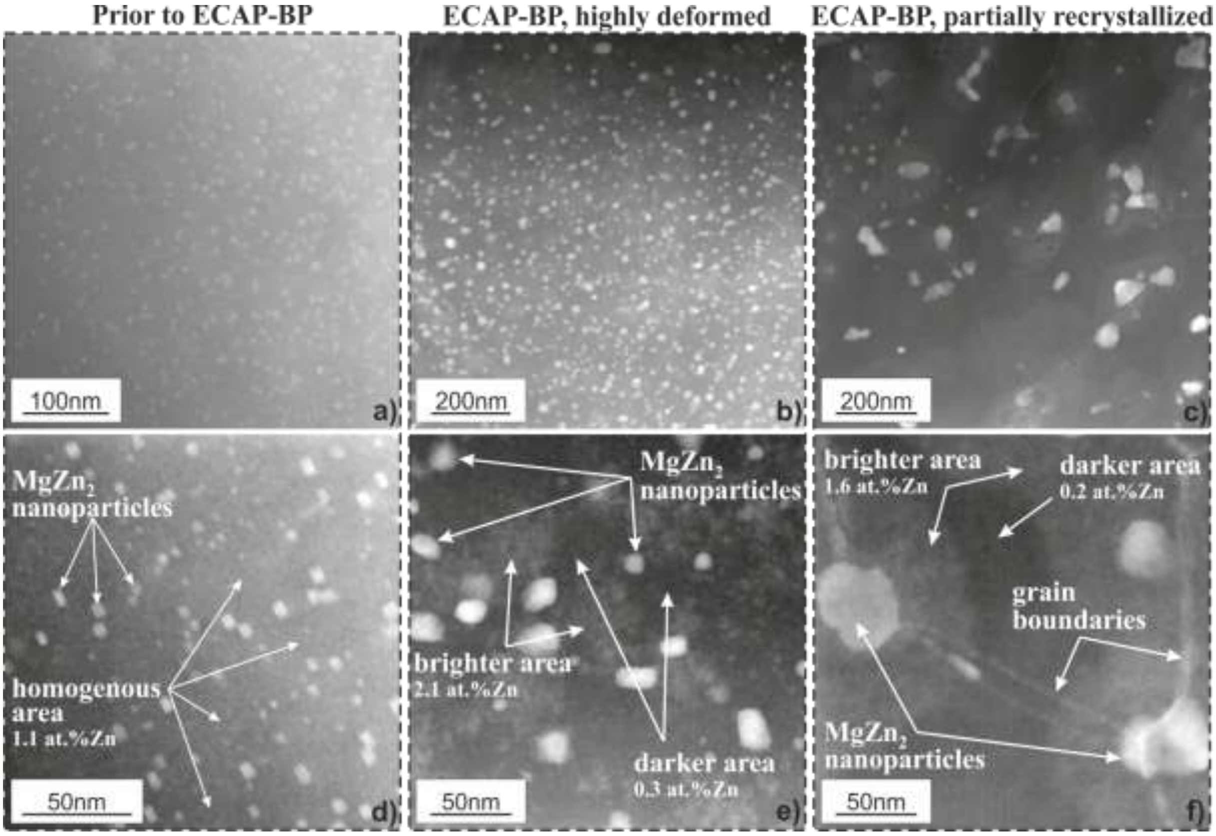

Fig. 40. HAADF-STEM images show Z-contrast of the microstructure of Mg12Zn alloy: a-c) general overview of the initial state α-Mg matrix, highly deformed and partially recrystallized regions of α-Mg matrix after ECAP-BP, respectively; d-f) details of α-Mg matrix with homogeneous contrast in the initial state (d) and brighter and darker areas in (e, f) caused by variation in Zn concentration as determined using EELS.

7.6.2 EELS Analysis

The EELS technique was performed as the next step after HAADF-STEM imaging to acquire approximate quantitative information about the inhomogeneous distribution of Zn in the α-Mg matrix of the Mg12Zn alloy. As presented in Fig. 40, five different types of Zn distributions in the α-Mg matrix were examined using HAADF-STEM:

i) homogenous area in an initial state of α-Mg matrix;
ii) darker area in a highly deformed α-Mg matrix after ECAP-BP;
iii) brighter area in a highly deformed α-Mg matrix after ECAP-BP;
iv) darker area in a partially recrystallized α-Mg matrix after ECAP-BP; and
v) brighter area in a partially recrystallized α-Mg matrix after ECAP-BP.

A hundred spectra were acquired from each type of Zn distribution (ten spectra from ten different instances for each type of Zn distribution). To minimize the effect of plural scattering during data acquisition, only areas near the specimen edges with low thickness (t) to mean free path (λ) ratio ($t/\lambda < 0.4$) were selected. The signal from the Zn-L and Mg-K edges after background subtraction was quantified using an elemental ratio method [70], [81] to obtain relative Zn content in at.%. Fig. 41 shows typical raw EEL spectra from sites with Zn concentrations close to the resulting averages.

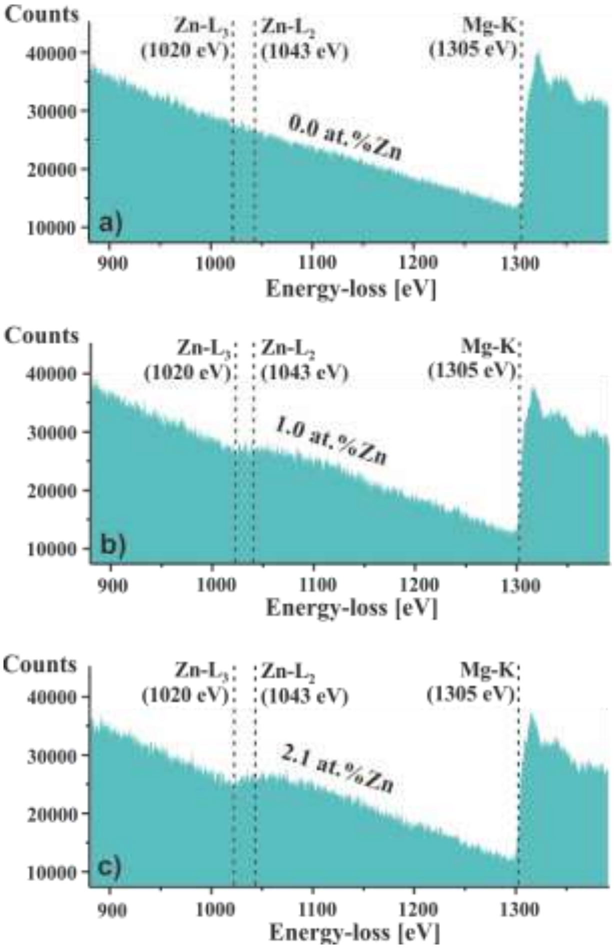

Fig. 41. Typical raw EEL spectra in Mg12Zn taken from different sites of the α-Mg matrix after ECAP-BP with Zn concentration close to resulting average values. a) Zn was not detected, b) approximately 1 at. % of Zn, c) approximately 2 at. % of Zn.

The relative Zn contents from each type of area were subsequently averaged over corresponding sets of the hundred spectra. Quantification errors of individual spectra were disregarded (they are in general in order of 10% [70], [81]). Parameters setting for data acquisition are listed in Table 2 and the obtained results are shown in Table 3. Although the standard deviations of the results may seem to be quite high, the results prove well the gradients of the Zn distribution. Moreover, the results are in accordance with the HAADF-

STEM imaging. Averaged relative atomic concentrations belonging to appropriate types of areas are also inscribed in Fig. 40d-f. The results in Table 3 clearly indicate how significant the differences in Zn concentration are in the α-Mg matrix, most notably after ECAP-BP where Zn concentrations vary by approximately 2 at.%. The EELS results therefore confirmed the presence of Zn concentration inhomogeneity in Mg12Zn after ECAP-BP and revealed depleted zones (Fig. 40f) with negligible Zn concentration in-between grown $MgZn_2$ nanoparticles after ECAP-BP.

Table 2

EELS acquisition and quantification parameters.

Convergence semi-angle α (mRad)	Collection semi-angle Β (mRad)	t / λ	Zn-L background (eV)	Zn-L integration (eV)	Mg-K Background (eV)	Mg-K Integration (eV)
11,3	29,4	0,2 – 0,4	900 - 1010	1020 - 1095	1225-1300	1305-1380

Table 3

Averaged relative atomic concentrations of Zn in different areas of the α-Mg matrix of the Mg12Zn in the initial state and after ECAP-BP as obtained using EELS and quantified using elemental ratio method.

Initial state homogenous area		ECAP highly def. darker area		ECAP highly def. brighter area	
Average (at. % Zn)	Std. dev. (at. % Zn)	Average (at. % Zn)	Std. dev. (at. % Zn)	Average (at. % Zn)	Std. dev. (at. % Zn)
1,0[a]	0,5	0,3[a]	0,3	2,1[a]	1,0

ECAP part. recryst. darker area		ECAP part. recryst. brighter area	
Average (at. % Zn)	Std. dev. (at. % Zn)	Average (at. % Zn)	Std. dev. (at. % Zn)
0,2[a]	0,2	1,6[a]	0,6

[a] see subsection 7.6.2 for the explanation of the average value meaning

A higher average concentration of Zn was expected in the α-Mg matrix of Mg12Zn in the initial state, because the solubility limit of Zn in Mg at 320 °C is slightly above 2 at.% [27]. A Zn concentration of 12 wt.% (that corresponds to approximately 5 at.%) highly exceeds this value. The EELS analysis shows in average only 1 at.% of Zn concentration in the initial state of α-Mg matrix. After a solution treatment at 320 °C for 20 h and subsequent quenching in warm water, the α-Mg should remain supersaturated by approximately 2 at.% of Zn. Since the specimens were stored at the RT, the EELS analysis revealed a precipitation process in the initial state Mg12Zn alloy at the RT resulting in the creation of $MgZn_2$ nanoparticles shown in the subsections 7.3.3 and 7.5.3.

7.7 Comparison of Mg6Zn and Mg12Zn Microstructures

In depth microstructure characterization of the Mg12Zn alloy in the initial state was described in the subsection 7.2. The microstructure of Mg12Zn alloy in the initial state consists of α-Mg grains with a size of approximately 150 μm and a large number of second phase particles with sizes from 1 to 10 μm that were identified as $Mg_{21}Zn_{25}$ phase (A-microparticles, see Fig. 23a, b). Nanoparticles were also detected, notably $MgZn_2$ (C-nanoparticles, Fig. 23c) with sizes ranging from 5 to 10 nm that adopted a specific orientation relationship (OR) toward the α-Mg matrix. The microstructure of the Mg6Zn alloy in the initial state (heat treatment conditions: 320 °C for 20 h with subsequent water quenching) is shown in Fig. 42a. The microstructure consists of large α-Mg grains (supersaturated solid solution of Zn in Mg) and a low number of large $Mg_{21}Zn_{25}$ microparticles with different morphology distributed predominantly at the grain boundaries. In comparison with the Mg12Zn alloy in initial state (Fig. 42c), the average grain size of Mg6Zn is slightly larger and the number of intermetallic particles is considerably lower.

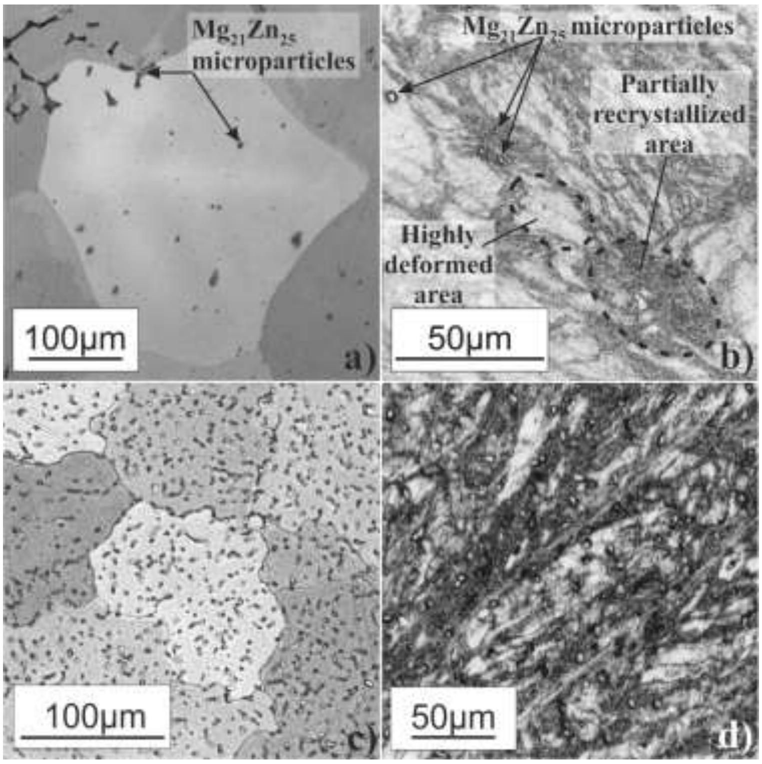

Fig 42. Microstructure of Mg6Zn and Mg12Zn alloys in the initial state and after ECAP-BP (LM images). a) a Typical microstrucutre of Mg6Zn alloy in the initial state and a distribution of $Mg_{21}Zn_{25}$ microparticles. b) a Typical microstructure of the Mg6Zn alloy after ECAP-BP consisting of highly deformed and partially recrystallized areas. c) a typical microstructure of Mg12Zn alloy in initial state with $Mg_{21}Zn_{25}$ microparticles distribution, and d) a typical microstructure of the Mg12Zn alloy after ECAP-BP consisting of highly deformed and partially recrystallized areas.

The microstructure of Mg12Zn after ECAP-BP was analyzed in the subsection 7.4. It consists of highly deformed and partially recrystallized regions with $MgZn_2$ and $Mg_{21}Zn_{25}$ particles variously affected by ECAP-BP processing. The microstructure of Mg6Zn after ECAP-BP processing (4 passes via Bc route) observed using LM was very similar to the microstructure of Mg12Zn after ECAP-BP (compare Fig. 42b and Fig. 42d). It can be seen that partially recrystallized areas of the α-Mg matrix (dark areas) alternate with highly deformed areas (light areas) of the α-Mg matrix. However, the lower amount of $Mg_{21}Zn_{25}$ microparticles in the Mg6Zn specimen is obvious.

Mg-Zn alloys after SPD with a composition similar to the Mg6Zn have also been analyzed by other authors [38], [50]. They found and described extensive twinning, areas with various amount of recrystallization, nano-sized precipitates and similar microstructural features that are present in the microstructure of Mg6Zn analyzed in this work.

7.8 Influence of ECAP-BP on Mg-Zn Microstructure - Summary

There are several factors influencing final microstructure after severe plastic deformation. One of them is mutual misorientation of the α-Mg matrix grains and secondary phases prior to ECAP-BP combined with ECAP geometry, which can cause local variations in accumulated deformation. Besides microstructure fragmentation during ECAP-BP, the elevated temperature used during SPD processing has significant influence on growth of the $MgZn_2$ nanoparticles due to inhomogeneity of Zn concentration in the α-Mg matrix (supersaturated solud solution of Zn in Mg). The growth of $MgZn_2$ nanoparticles directly from α-Mg matrix during in-situ heating experiment was shown in the subsection 7.3.3.1. Moreover, the growth of the $MgZn_2$ nanoparticles during ECAP-BP was dependent also on a type of the α-Mg matrix area, as was shown in the subsection 7.5.3. In general, increased chemical inhomogeneity in the solid solution of the α-Mg matrix was shown in Fig. 25 and Fig. 39. This chemical inhomogeneity of the Zn distribution in solid solution of the α-Mg matrix was of the Mg12Zn alloy after ECAP-BP was investigated by HAADF-STEM imaging and EELS in the subsection 7.6.

7.9 Mechanical Properties of Mg6Zn and Mg12Zn

Fig. 43a shows the characteristic true stress–true strain compression curves of the Mg6Zn and Mg12Zn after ECAP-BP measured along ID, ED and TD directions (see Fig. 22 for denotation). Curves of Mg6Zn and Mg12Zn alloys in the initial state are also shown for comparison in Fig. 43b. In the case of Mg6Zn after ECAP-BP, only the ED direction was measured due to a limited material quantity. The measured values of the yield stress σ_{02}, maximum stress σ_{max} and compressive strain to failure ε are listed in Table 4.

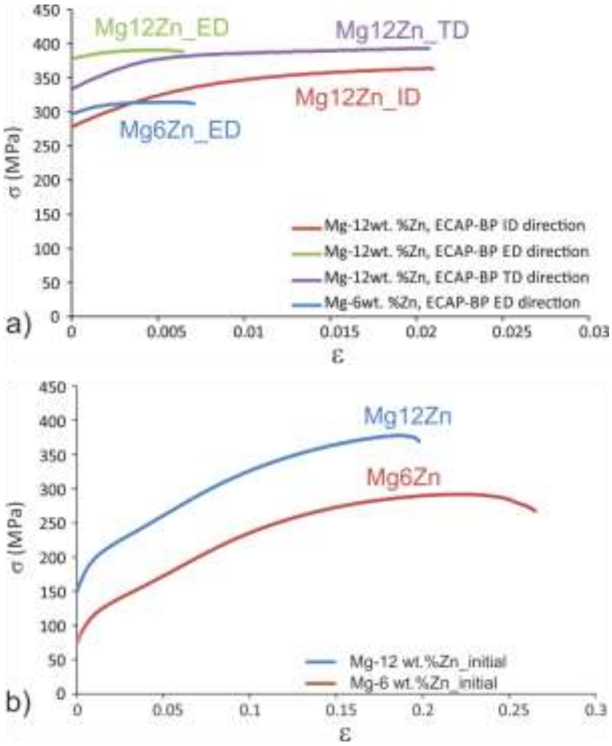

Fig. 43. Compression tests results. True stress – true strain curves measured for Mg6Zn and Mg12Zn alloys at RT at the initial strain rate of 1.1 x 10^{-3} s^{-1}: a) after ECAP-BP (ID, ED and TD directions for Mg12Zn and ED direction for Mg6Zn); b) initial state alloys.

Table 4

The measured compression values of the yield stress σ_{02}, maximum stress σ_{max} and compressive strain to failure A at RT for Mg6Zn and Mg12Zn alloys in different conditions and pure Mg after ECAP for comparison (data for pure Mg taken from [82]). Each number is an average of at least two measurements.

	σ_{02} (MPa)	σ_{max} (MPa)	A (%)
Mg6Zn, initial state	75	290	26
Mg12Zn, initial state	150	362	19
Mg6Zn, ECAP-BP – ED	302	314	0.7
Mg12Zn, ECAP-BP – ED	385	391	0.6
Mg12Zn, ECAP-BP – ID	269	355	2.1
Mg12Zn, ECAP-BP – TD	340	393	2.1
pure Mg, ECAP at ~ 200 °C [82]	58 – 82	152 - 210	8 - 10

Fig. 43 and Table 4 show that initial state Mg-Zn alloys have noticeable strain to failure and significant strain hardening, but the yielding occurs at relatively low stresses. In contrast, Mg-Zn after ECAP-BP demonstrates a two- to threefold increase in the yield strength, a tendency to equilibrium between hardening and softening processes, and a reduced compressive strain to failure. The material processed by ECAP-BP also exhibits directional dependence of compression properties. This mechanical anisotropy has already been observed in hexagonal close packed Titanium subjected to ECAP-BP [83] and the results show that specimen orientation also has a noticeable impact on mechanical properties of Mg12Zn alloy. A similar tendency can be expected for Mg6Zn alloy as well. The yield stress and maximum stress for initial state Mg12Zn are 2 to 3 times higher than pure Mg subjected to different ECAP conditions (see Table 4) [82], which highlights the strengthening effect of Zn. In the case of the Mg12Zn alloy after ECAP-BP the yield stress and maximum stress is about 3 to 6 times higher than that for pure Mg after ECAP. However, in contrast to pure Mg after ECAP, Mg12Zn alloy after ECAP-BP is very brittle in all compression directions. Systematically higher values of both characteristic stresses for Mg12Zn in comparison with Mg6Zn (both initial state and after ECAP-BP) are mainly caused by the higher concentration of $Mg_{21}Zn_{25}$ microparticles and smaller grain size in the initial state, which are also responsible for lowering of compressive strain to failure of Mg12Zn alloy in both states.

7.10 Corrosion Properties of Mg6Zn and Mg12Zn

Specimens of Mg6Zn and Mg12Zn alloys in the initial state as well as specimens after ECAP-BP processing were exposed to an NaCl solution at 37° C (human body temperature) for 26 hours to determine the influence of ECAP-BP on the corrosion rate. The results of corrosion rate using a hydrogen evolution method are shown in Fig. 44. It is clearly seen that the corrosion rates of the initial state alloys are lower than that of the materials after ECAP-BP, and the corrosion rate of Mg6Zn alloy for the initial state and after ECAP-BP specimens is markedly lower than those of Mg12Zn alloy in both states. The corrosion rate for Mg6Zn alloy in the initial state (empty squares), was negligible at the end of the exposure, except for two instances (the two non-zero values in the lower-right part of the graph). These two non-zero values were caused by the loosening of whole fragments of material from the specimen during exposure. The loosening of whole fragments also accounted for higher fluctuations of data for the other alloys.

Macro images of the specimens after corrosion rate measurement are shown in Fig. 45 a-d. Visual inspection revealed that the less eroded surface is in the case of Mg6Zn alloy in the initial state and the most eroded surface is associated with the case of Mg12Zn alloy after ECAP-BP. The results are in accordance with measured corrosion rates (Fig. 44). Cross-sections of the specimens after corrosion tests were examined by LM (Fig. 45e and 45g). It can be seen that there are no preferences for the initial state in both alloys in terms of transcrystalline or intercrystalline corrosion. Additionally, no pronounced dependence of corrosion progress on α-Mg matrix area type after ECAP-BP (i.e., partially recrystallized or highly deformed) was found (Fig. 45f and 45h).

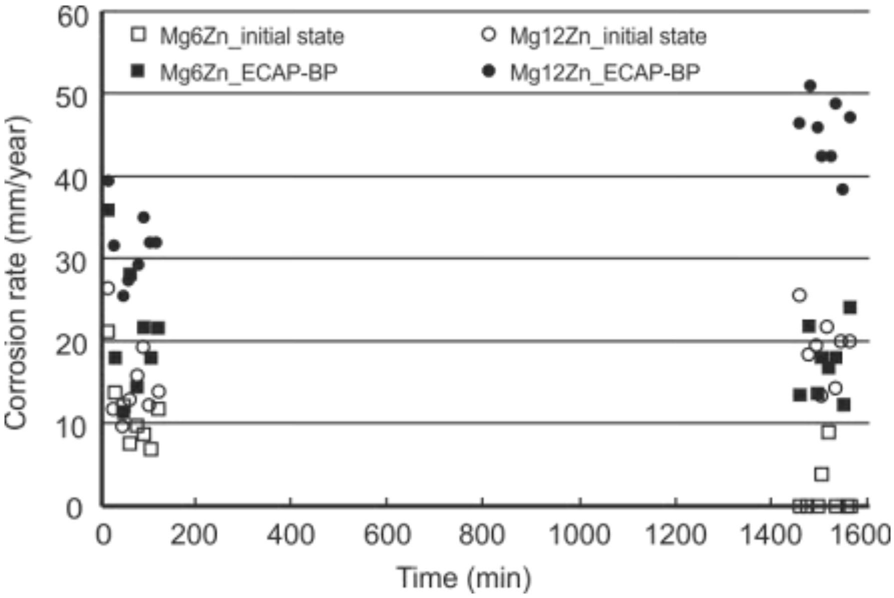

Fig. 44. Results of the corrosion rate measurement using a hydrogen evolution method. Obtained values for corrosion rates are represented by empty squares, filled squares, empty circles and filled circles for Mg6Zn alloy in the initial state, Mg6Zn alloy after ECAP-BP, Mg12Znalloy in initial state and Mg12Zn after ECAP-BP, respectively.

The results indicate that the alloy with lower Zn content has higher corrosion resistance than alloy with higher Zn content. Alloying over the solid solubility limit is beneficial for the improvement of mechanical properties through hardening effects but considerably deteriorate corrosion properties. A similar conclusion has been drawn by Zhang although for a different corrosion rate measurement technique [46]. Our results show that the corrosion rate in an NaCl solution is significantly increased in the case of ultrafine-grained Mg-Zn alloy processed by ECAP-BP compared to the coarse-grained alloy in the initial state. It has been reported that various Mg-alloys processed by extrusion exhibit slower corrosion rate than the as-cast states [47]. However, this is not the case of Mg6Zn and Mg12Zn aloys processed by multiple ECAP-BP passes, where the grain refinement has the opposite effect.

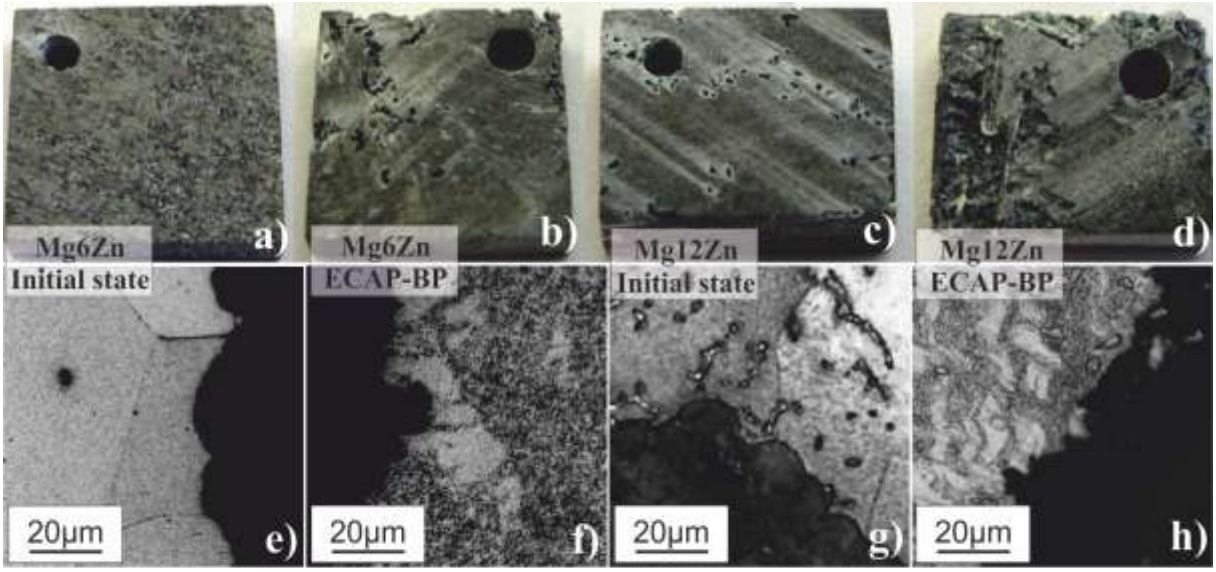

Fig. 45. Specimens after 26 hours of exposure in an NaCl solution. Images of specimens are shown in a) – d). Each specimen has a drilled hole with a diameter of about 1.5 mm for a plastic fiber to fix it in the NaCl solution. Corresponding LM images from the cross-sections are shown in e) – h).

8 Conclusions

Thorough analysis of Mg-Zn binary alloys in initial state and after severe plastic deformation was conducted. The results provide fundamental understanding about microstructure of investigated alloys down to the nano-scale. Essential gap in knowledge about the $Mg_{21}Zn_{25}$ phase was overcome. Influence of severe plastic deformation and alloying element Zn on microstructure, and mechanical and corrosion properties of the Mg-Zn alloys was described in depth. Obtained results provide invaluable knowledge for design of advanced Mg-Zn alloys with desirable properties for construction applications and biomedical implants. Following conclusions can be extracted from the thesis.

8.1 Mg-Zn Alloys Initial State

- The Mg-12 wt.%Zn alloy after casting and annealing at 320 °C / 20 h consists of coarse grained microstructure (grains size ~ 150 μm and a large number of intermetallic particles.
- It was proven by various electron diffraction techniques that the A-microparticles of size about 1 – 10 μm adopts the $Mg_{21}Zn_{25}$ crystal structure with trigonal symmetry.
- Presence and identification of the A-microparticles unambiguously confirm that the $Mg_{21}Zn_{25}$ phase should replace the MgZn phase in the generally accepted Mg-Zn binary phase diagram.
- The C-nanoparticles with the hexagonal $MgZn_2$ crystal structure of size about 5 – 10 nm are evenly distributed within the α-Mg matrix. Majority of them possess orientation relationship:

$$[0001]MgZn_2 \,||\, [0001]\alpha - Mg;\ (01\bar{1}0)MgZn_2 \,||\, (11\bar{2}0)\alpha - Mg.$$

- The Mg-12 wt.%Zn alloy can precipitate at room temperature.
- Compared to the Mg-12 wt.%Zn alloy, the microstructure of the Mg-6 wt.%Zn alloy after casting and annealing at 320 °C / 20 h consists of lower amount of intermetallic particles. The grain size is slightly larger.

8.2 Mg-Zn Alloys After ECAP-BP

- The α-Mg matrix of Mg-6 wt.%Zn and Mg-12%Zn alloys after ECAP-BP consists of highly deformed or partially recrystallized areas. Average grain size in the partially recrystallized areas attains about 250 nm.
- Volume fractions of highly deformed and partially recrystallized structures are similar.
- The A-microparticles are preferential sites for recrystallization of the α-Mg matrix during ECAP-BP processing.
- The A-microparticles showed three diiferent forms: single-crystalline, nano-crystalline and broken up or their combinations.
- The C-nanoparticles have grown during ECAP-BP up to ~100 nm. The orientation relationship OR1 was preserved. The second common orientation relationship OR2 was found to be important after ECAP-BP:

$$[0001]MgZn_2 \mid\mid [11\bar{2}0]\alpha - Mg; (11\bar{2}0)MgZn_2 \mid\mid (0001)\alpha - Mg.$$

- Zn concentration within the α-Mg matrix varies in average from 0,3 at.% to 2,1 at.%.
- ECAP-BP processing increased the corrosion rate of analyzed Mg-Zn alloys.The yield stress was increased by a factor of 2–3 at the expense of ductility.

References

[1] M.M. Avedesian, H. Baker, Magnesium and Magnesium Alloys, ASM International (1999), Materials Park.

[2] C. Bettles, M. Barnett, Advances in wrought magnesium alloys, Woodhead Publishing Limited, Cambridge, 2012.

[3] J.B. Clark, Transmission electron microscopy study of age hardening in a Mg-5wt.%Zn

[4] J.M. Rosalie, H. Somekawa, A. Singh, T. Mukai, Structural relationships among monoclinic and hexagonal phases and transition structures in Mg-Zn-Y alloys, Philosophical Magazine 90 (2012) 3355–3374.

[5] S. Deledda, B.C. Hauback, H. Fjellvåg, H-sorption behaviour of mechanically activated Mg–Zn powders, J. All. Comp. 446–447 (2007) 173–177.
alloy, Acta Metall. 13 (1965) 1281–1289.

[6] P. Blanco-Rodríguez, J. Rodríguez-Aseguinolaza, E. Risueño, M. Tello, Thermophysical characterization of Mg-51%Zn eutectic metal alloy: A phase change material for thermal energy storage in direct steam generation applications, Energy 72 (2014) 414–420.

[7] Institute of Physics, ASCR, A. Jäger, Czech Republic, Preparation of $Mg(OCH_3)_2$ by reaction of Mg and CH_3OH with catalytic help of Zn, National patent no. 304987 (2015).

[8] R. Agarwal, H.L. Lukas, G. Petzow, F. Sommer, T. G. Chart, G. Effenberg, Assesment of the Mg-Zn System Zeits, Metallk. 83 (1992) 216–223.

[9] P. Liang, H.J. Seifert, H.L. Lukas, G. Ghosh, G. Effenberg, F. Aldinger, Thermodynamic Modelling of the Cu-Mg-Zn Ternary System, CALPHAD 22 (1998) 527–544.

[10] S. Wasiur-Rahman, M. Medraj, Critical assessment and thermodynamic modeling of the binary Mg–Zn, Ca–Zn and ternary Mg–Ca–Zn systems, Intermetallics 17 (2009) 847–864.

[11] P. Ghosh, M. Mezbahul-Islam, M. Medraj, Critical assessment and thermodynamic modeling of Mg–Zn, Mg–Sn, Sn–Zn and Mg–Sn–Zn systems, CALPHAD 36 (2012) 28–43.

[12] S.K. Das, Y.-M. Kim, T.K. Ha, I.-H.Jung, Investigation of anisotropic diffusion behavior of Zn in hcp Mg and interdiffusion coefficients of intermediate phases in the Mg–Zn system, CALPHAD 42 (2013) 51–58.

[13] P. Liang, T. Tarfa, J. A. Robinson, S. Wagner, P. Ochin, M. G. Harmelin, H. J. Seifert, H.L. Lukas, F. Aldinger, Experimental investigation and thermodynamic calculation.

[14] X. Gao, J.F. Nie, Structure and thermal stability of primary intermetallic particles in an Mg–Zn casting alloy, Scripta Materialia 57 (2007) 655–658.

[15] X. Gao, J.F. Nie, Characterization of strengthening precipitate phases in a Mg–Zn alloy, Scripta Materialia 56 (2007) 645–648.

[16] A. Berche, C. Drescher, J. Rogez, M.-C. Record, S. Brühne,W. Assmus, Thermodynamic measurements in the Mg–Zn system, J. All. Comp. 503 (2010) 44–49.

[17] J.B. Clark, F.N. Rhines, Central region of the Mg- Zn phase diagram, Journal of Metals 9 (1957) 425–430.

[18] L.Y. Wei, G.L. Dunlop, H. Westengen, Precipitation Hardening of Mg-Zn and Mg-Zn-RE Alloys, Metall. Mater. Trans. 26A (1995) 1705–1716.

[19] T.B. Massalski, Binary Alloy Phase Diagrams, ASM (1990) 2571–2572.

[20] H. Okamoto, Comment on Mg-Zn (Magnesium-Zinc), J. Phase Eq. 15 (1994) 129–130.

[21] W. Hume-Rothery, E.O. Rounsefell, The system magnesium–zinc, J. Inst. Met. 41 (1929) 119–138.

[22] L. Tarschnisch, Röntgenographische Untersuchung der Verbin-dungen MgZn und $MgZn_5$ X-ray studies on the compound MgZn, Zeits. Kristallogr. 86 (1933) 423–438.

[23] Y. Khan, Dynamic temperature crystallization behavior of amorphous and liquid $Mg_{70}Zn_{30}$ alloy, J. Mater. Sci. 24 (1989) 963–973.

[24] R. Černý, G. Renaudin, The intermetallic compound $Mg_{21}Zn_{25}$, Acta Crystallographica C (2002) 154–155.

[25] R.C. Ropp, Encyclopedia of the Alkaline Earth Compounds, Elsevier (2013) 1115–1122.

[26] Inorganic material database 26, Materials Information Station, National Institute for Materials Science, Tsukuba, Japan.
Available online (2018/08/03): http://crystdb.nims.go.jp

[27] H. Okamoto, Supplemental literature review of binary phase diagrams: Cs-In, Cs-K, Cs-Rb, Eu-In, Ho-Mn, K-Rb, Li-Mg, Mg-Nd, Mg-Zn, Mn-Sm, O-Sb, and Si-Sr, J. Phase Equilib. Diffus. 34 (2013) 251–263.

[28] I. Higashi, N. Shiotani, M. Uda, T. Mizoguchi, H. Katoh, The Crystal Structure of $Mg_{51}Zn_{20}$, J. Solid State Chemistry 36 (1981) 225–233.

[29] Y.P. Yarmolyuk, P.I. Kripyakevich, E.V. Mel'nik, Crystal structure of the compound Mg_4Zn_7, Sov. Phys. Crystallogr. 20 (1975) 329–331.

[30] Y. Komura, K. Tokunaga, Structural Studies of Stacking Variants in Mg-Base Friauf-Laves Phases, Acta Crystallographica B 36 (1980) 1548–1554.

[31] H. Euchner, M. Mihalkovič, F. Gähler, M.R. Johnson, H. Schober, S. Rols, E. Suard, A. Bosak, S. Ohhashi, A.P. Tsai, S. Lidin, C.P. Gomez, J. Custers, S. Paschen, M. de Boissieu, Anomalous vibrational dynamics in the Mg_2Zn_{11} phase, Physical Review B 83 (2011) 144202-1–144202-17.

[32] Y. Yuan, F. Pan, D. Li, A. Watson, The re-assessment of the Mg–Zn and Fe–Si systems and their incorporation in thermodynamic descriptions of the Al–Mg–Zn and Fe–Si–Zn systems, CALPHAD 44 (2014) 54–61.

[33] M. Krystian, M.J. Zehetbauer, H. Kropik, B. Mingler, G. Krexner, Hydrogen storage properties of bulk nanostructured ZK60 Mg alloy processed by Equal Channel Angular Pressing, J. Alloys Compd. 509S (2011) S449–S455.

[34] J. Jain, P. Cizek, W.J. Poole, M.R. Barnett, Precipitate characteristics and their effect on the prismatic–slip–dominated deformation behaviour of an Mg–6 Zn alloy, Acta Materialia 61 (2013) 4091–4102.

[35] R.Z. Valiev, T.G. Langdon, Principles of equal–channel angular pressing as a processing tool for grain refinement, Progress in Materials Science 51 (2006) 881–981.

[36] P.G. Partridge, The crystallography and deformation modes of hexagonal close–packed metals, Metallurgical Reviews 12 (1967) 169–194.

[37] B. Li, P.F. Yan, M.L. Sui, E. Ma, Transmission electron microscopy study of stacking faults and their interaction with pyramidal dislocations in deformed Mg, Acta Materialia 58 (2010) 173–179.

[38] A. Singh, H. Somekawa, T. Mukai, Formation of nano–twin domains by nucleation and multiplication of twins during fracture of a magnesium alloy, Philos. Mag. 94 (2014) 898–913.

[39] J. Nagels, M. Stokdijk, P. M. Rozing, Stress shielding and bone resorption in shoulder arthroplasty, J. Shoulder Elbow Surg. 12 (2003) 35–39.

[40] F. Witte, The history of biodegradable magnesium implants: A review, Acta Biomaterialia 6 (2010) 1680–1692.

[41] B. Chen, Ch. Lu, D. Lin, X. Zeng, Microstructural Evolution and Mechanical Properties of Mg95.5Y3Zn1.5 Alloy Processed by Extrusion and ECAP, Met. Mater. Int. 20 (2014) 285–290.

[42] M.P. Staiger, A.M. Pietak, J. Huadmai, G. Dias, Magnesium and its alloys as orthopedic biomaterials: A review, Biomaterials 27 (2006) 1728–1734.

[43] F. Witte, N. Hort, C. Vogt, S. Cohen, K.U. Kainer, R. Willumeit, F. Feyerabend, Degradable biomaterials based on magnesium corrosion, Current Opinion in Solid State and Materials Science 12 (2008) 63–72.

[44] D. Vojtěch, J. Kubásek, J. Šerák, P. Novák, Mechanical and corrosion properties of newly developed biodegradable Zn-based alloys for bone fixation, Acta Biomater. 7 (2011) 3515–3522.

[45] G. Song, Control of biodegradation of biocompatable magnesium alloys, Corrosion Science 49 (2007) 1696–1701.

[46] S. Zhang, X. Zhang, Ch. Zhao, J. Li, Y. Song, Ch. Xie,H. Tao, Y. Zhang, Y. He, Y. Jiang, Y. Bian, Research on an Mg–Zn alloy as a degradable biomaterial, Acta Biomaterialia 6 (2010) 626–640.

[47] Y. Chen, Z. Xu, Ch. Smith, J. Sankar, Recent advances on the development of magnesium alloys for biodegradable implants, Acta Biomaterialia 10 (2014) 4561–4573.

[48] Y. Cui, Y. Li, Z. Wang, X. Ding, Y. Koizumi, H. Bian, L. Lin, A. Chiba, Impact of solute elements on detwinning in magnesium and its alloys, Inter. J. Plast. 91 (2017) 134–139.

[49] Cui, Y., et al., Regulating twin boundary mobility by annealing in magnesium and its alloys, International Journal of Plasticity (2017).
http://dx.doi.org/10.1016/j.ijplas.2017.08.002

[50] D.A. Basha, J.M. Rosalie, H. Somekawa, T. Miyawaki, A. Singh, K. Tsuchiya, Microstructure study of a severely plastically deformed Mg-Zn-Y alloy by application of low angle annular dark field diffraction contrast imaging, Sci. Technol. Adv. Mater. 17 (2016) 115–127.

[51] V. Gärtnerová, A. Singh, A. Jäger, T. Mukai, Deformation behavior of ultra-fine-grained Mg-0.3 at% Al alloy in compression, Journal of Alloys and Compounds 726 (2017) 651–657.
of the Al-Mg-Zn system, Thermochim. Acta 314 (1998) 87–110.

[52] Thermo Fisher Scientific, Electron Microsopy Solutions
Available online (2018/10/02): https://www.fei.com/materials-science/

[53] L.M. Brown, P.E. Batson, N. Dellby, O.L. Krivanek, Brief history of the Cambridge STEM aberration correction project and its progeny, Ultramicroscopy 157 (2015), 88–90.

[54] R.F. Egerton, Vibrational-loss EELS and the avoidance of radiation damage, Ultramicroscopy 159 (2015) 95–100.

[55] D.B. Williams, C.B. Carter, Transmission Electron Microscopy, second edition, Springer (2009), New York.

[56] X. Zou, S. Hovmöller, P. Oleynikov, Electron Crystallography, Oxford University Press (2011), Oxford.

[57] G. Burns, A.M. Glazer, Space Groups for Solid State Scientists, third ed., Academic Press (2013), Waltham.

[58] M. De Graef, M.E. McHenry, Structure of Materials: An Introduction to Crystallography, Diffraction and Symmetry, second edition, University Press (2012), Cambridge.

[59] J.W. Eddington, Electron Diffraction in the Electron Microscope, Macmillan EducationUK (1975), Cambridge.

[60] R.E. Reed-Hill, Physical Metallurgy Principles, second ed., Litton Educational Publishing (1973), Monterey.

[61] J.P. Morniroli, Large-Angle Convergent Beam Electron Diffraction (LACBED), Société Française des Microscopies (2002), Paris.

[62] P. Haasen, Physical Metallurgy, University Press (1996), Cambridge.

[63] L. Ptáček, Nauka o materiálu I., second ed., CERM (2003), Brno.

[64] R.Z. Valiev, R.K. Islamgaliev, I.V. Alexandrov, Bulk nanostructured materials from severe plastic deformation, Progress in Materials Science 45 (2000) 103–189.

[65] F.J. Humpreys, M. Hatherly, Recrystallization and Related Annealing Phenomena, Elsevier (2004), Kidlington.

[66] J. Ayache, L. Beaunier, J. Boumendil, G. Ehret, D. Laub, Sample Preparation Handbook for Transmission Electron Microscopy: Methodology, Springer, New York (2010).

[67] J. Ayache, L. Beaunier, J. Boumendil, G. Ehret, D. Laub, Sample Preparation Handbook for Transmission Electron Microscopy: Techniques, Springer, New York (2014).

[68] L.A. Gianluzzi, F.A. Stevie, Introduction to Focused Ion Beams: Instrumentation, Theory, Techniques and Practice, Springer, New York (2005).

[69] M. Karlík, Úvod Do Transmisní Elektronové Mikroskopie, Česká technika – nakladatelství ČVUT (2011), Prague.

[70] R.F. Egerton, Electron Energy-Loss Spectroscopy in the Electron Microscope, third ed., Springer (2011), New York.

[71] M. Němec, V. Gärtnerová, A. Jäger, Influence of severe plastic deformation on intermetallic particles in Mg-12 wt.%Zn alloy investigated using transmission electron microscopy, Mater. Charact. 119 (2016) 129–136.

[72] M. Klinger, CrysTBox - Crystallographic Toolbox, Institute of Physics of the AS CR, Prague, Czech Republic (2015).
Available online (2018/10/02): http://www.fzu.cz/crystbox

[73] L. Palatinus, PETS – program for analysis of electron diffraction data, Institute of Physics of the AS CR, Prague, Czech Republic (2011).

[74] L. Palatinus, G. Chapuis, SUPERFLIP - a computer program for the solution of crystal structures by charge flipping in arbitrary dimensions, *J. Appl. Cryst.* 40 (2007) 786–790.

[75] V. Petricek, M. Dusek, L. Palatinus, The crystallographic computing system JANA2006:General features, Zeits. Kristallogr. 229 (2014) 345–352.

[76] G. Song, A. Atrens, D. StJohn, An hydrogen evolution method for estimation of the corrosion rate of magnesium alloys, TMS (The Minerals, Metals & Materials Society) (2001) 255–262.

[77] U. Kolb, T. Gorelik, C. Kubel, M.T. Otten, D. Hubert, Towards automated diffraction tomography: Part I—Data acquisition, Ultramicroscopy 107 (2007) 507–513.

[78] U. Kolb, T. Gorelik, M.T. Otten, Towards automated diffraction tomography. Part II—Cell parameter determination, Ultramicroscopy 108 (2008) 763–772.

[79] E. Mugnaioli, T. Gorelik, U. Kolb, ‘‘Ab initio’’ structure solution from electron diffraction data obtained by a combination of automated diffraction tomography and precession technique, Ultramicroscopy 109 (2009 758–765.

[80] M. Němec, V. Gärtnerová, M. Klementová, A. Jäger, Analysis of intermetallic particles in Mg–12 wt.%Zn binary alloy using transmission electron microscopy, Materials Characterization 106 (2015) 428–436.

[81] C.C. Ahn, Transmission electron energy loss spectrometry in materials science and the eels atlas, second, Willey, Pasadena, 2004.

[82] F.S.J. Poggiali, C.L.P. Silva, P.H.R. Pereira, R.B. Figueiredo, P.R. Cetlin, Determination of mechanical anisotropy of magnesium processed by ECAP, J. Mater. Res. Technol. 3 (2014) 331–337.

[83] A. Jäger, V. Gärtnerová, K. Tesař, Microstructure and anisotropy of the mechanical properties in commercially pure titanium after equal channel angular pressing with back pressure at room temperature, Materials Science and Engineering A 644 (2015) 114–120.

[84] M. Němec, A. Jäger, K. Tesař, V. Gärtnerová, Influence of alloying element Zn on the microstructural, mechanical and corrosion properties of binary Mg-Zn alloys after severe plastic deformation, Materials Characterization 134 (2017) 69–75.

List of Author´s Work Related to the Thesis

Results of the thesis described in the corresponding subsections of the Results and Discussion section were published in the following work (all impacted in WoS).

Subsections 7.2 and 7.3:

[80] M. Němec, V. Gärtnerová, M. Klementová, A. Jäger, Analysis of intermetallic particles in Mg–12 wt.%Zn binary alloy using transmission electron microscopy, Materials Characterization 106 (2015) 428–436.

Cited by:

[C1] Zhang, L. Wang, W. Hu, W. Yang, Z. Ye, H. Nanometer-sized domain structure in complex Mg21Zn25 formed by eutectoid phase transformation in a Mg-Zn alloy Journal of Alloys and Compounds, vol. 745, pp. 319 - 330, 2018.

[C2] Verissimo, N.C., Brito, C., Afonso, C.R., (...), Cheung, N., Garcia, A. Microstructure characterization of a directionally solidified Mg-12wt.%Zn alloy: Equiaxed dendrites, eutectic mixture and type/ morphology of intermetallics, Materials Chemistry and Physics, 2018.

[C3] She, J., Pan, F.S., Guo, W., (...), Yu, Z.W., Rashad, M. Effect of high Mn content on development of ultra-fine grain extruded magnesium alloy, Materials and Design, 2016.

[C4] Verissimo, N.C., Brito, C., Santos, W.L.R., (...), Spinelli, J.E., Garcia, A. Interconnection of Zn content, macrosegregation, dendritic growth, nature of intermetallics and hardness in directionally solidified Mg-Zn alloys, Journal of Alloys and Compounds, 2016.

[AC1] Němec, M., Jäger, A., Tesař, K., Gärtnerová, V. Influence of alloying element Zn on the microstructural, mechanical and corrosion properties of binary Mg-Zn alloys after severe plastic deformation, Materials Characterization, 2017.

[AC2] Němec, M., Gärtnerová, V., Jäger, A. Influence of severe plastic deformation on intermetallic particles in Mg-12 wt.%Zn alloy investigated using transmission electron microscopy, Materials Characterization, 2016.

[AC3] Ciccarelli, D., El Mehtedi, M., Jäger, A., Spigarelli, S. Analysis of flow stress and deformation mechanism under hot working of ZK60 magnesium alloy by a new strain-dependent constitutive equation, Journal of Physics and Chemistry of Solids, 2015.

Subsections 7.4 and 7.5:

[71] M. Němec, V. Gärtnerová, A. Jäger, Influence of severe plastic deformation on intermetallic particles in Mg-12 wt.%Zn alloy investigated using transmission electron microscopy, Mater. Charact. 119 (2016) 129–136.

Cited by:

[C5] X. Hou, R. Hu, Y. Yang et al. Modification based on internal refinement and external decoration: A powerful strategy for superior thermodynamics and hysteresis of Mg-Ni hydrogen energy storage alloys, Journal of Alloys and Compounds, 2018.

[C6] Hu, Y., Zhang, C., Meng, W., Pan, F., Zhou, J, Microstructure, mechanical and corrosion properties of Mg-4Al-2Sn-xY-0.4Mn alloys, Journal of Alloys and Compounds, 2017.

[C7] Hou, X., Hu, R., Yang, Y., Feng, L., Isothermal activation, thermodynamic and hysteresis of MgH2 hydrides catalytically modified by high-energy ball milling with MWCNTs and TiF3, International Journal of Hydrogen Energy, 2017.

[C8] Zeng, F., Cai, Q., Liu, X., (...), Xie, Y., Wang, Y., Fabrication and mechanical properties of mesoporous silica nanoparticles reinforced magnesium matrix composite, Journal of Alloys and Compounds, 2017.

[AC4] Němec, M., Jäger, A., Tesař, K., Gärtnerová, V. Influence of alloying element Zn on the microstructural, mechanical and corrosion properties of binary Mg-Zn alloys after severe plastic deformation , Materials Characterization, 2017.

Subsections 7.6, 7.7, 7.8 and 7.9:

[84] M. Němec, A. Jäger, K. Tesař, V. Gärtnerová, Influence of alloying element Zn on the microstructural, mechanical and corrosion properties of binary Mg-Zn alloys after severe plastic deformation, Materials Characterization 134 (2017) 69–75.

Cited by:

[C9] Zhong, L.; Wang, Y. Gong, M. Zheng, X. Peng, J. Effects of precipitates and its interface on thermal conductivity of Mg-12Gd alloy during aging treatment, Materials Characterization, vol. 138, pp. 284 - 288, 2018.

List of Author´s Work Unrelated to the Thesis

Author´s work unrelated to the thesis was published in (all impacted in WoS):

[85] M. Klinger, M. Němec, L. Polívka, V. Gärtnerová, A. Jäger, Automated CBED processing: Sample thickness estimation based on analysis of zone-axis CBED pattern, Ultramicroscopy 150 (2015) 88–95.

Cited by:

[C10] Karcz, A.P., Damø, A.J., Illerup, J.B., (...), Dam-Johansen, K., Chaiko, D., Electron microscope investigations of activated chalcopyrite particles via the FLSmidth®ROL process, Journal of Materials Science, 2017.

[C11] Pollock, J.A., Weyland, M., Taplin, D.J., Allen, L.J., Findlay, S.D., Accuracy and precision of thickness determination from position-averaged convergent beam electron diffraction patterns using a single-parameter metric, Ultramicroscopy, 2017.

[C12] Lábár, J.L., Das, P.P., Pattern Center and Distortion Determined from Faint, Diffuse Electron Diffraction Rings from Amorphous Materials, Microscopy and Microanalysis, 2017.

[C13] Honglong, S., Minting, L., Wenzhong, W., CBED Tools for semi-automatic measurement of crystal thicknesses, Journal of Applied Crystallography, 2017.

[C14] W. Xu, J.M. LeBeau, A deep convolutional neural network to analyze position averaged convergent beam electron diffraction patterns, Ultramicroscopy, 2018.

[AC5] Gartnerova, V., Pacherova, O., Klinger, M., (...), Jager, A., Tyunina, M., Strain fluctuations in BaTiO3/SrTiO3 heterostructures, Materials Research Bulletin, 2017.

[AC6] Klinger, M., More features, more tools, more CrysTBox, Journal of Applied Crystallography, 2017.

[AC7] Klinger, M., Polívka, L., Jäger, A., Tyunina, M, Quantitative analysis of structural inhomogeneity in nanomaterials using transmission electron microscopy, Journal of Applied Crystallography, 2016.

[AC8] Klinger, M., Jäger, A., Crystallographic Tool Box (CrysTBox): Automated tools for transmission electron microscopists and crystallographers, Journal of Applied Crystallography, 2015.